

2010

Electron Dynamics in High-Intensity Laser Fields

Harvey, Christopher

<http://hdl.handle.net/10026.1/301>

<http://dx.doi.org/10.24382/1563>

University of Plymouth

All content in PEARL is protected by copyright law. Author manuscripts are made available in accordance with publisher policies. Please cite only the published version using the details provided on the item record or document. In the absence of an open licence (e.g. Creative Commons), permissions for further reuse of content should be sought from the publisher or author.

**ELECTRON DYNAMICS IN
HIGH-INTENSITY LASER FIELDS**

by

CHRISTOPHER HARVEY

A thesis submitted to the University of Plymouth
in partial fulfilment for the degree of

DOCTOR OF PHILOSOPHY

School of Computing and Mathematics
Faculty of Science and Technology

August 2010

Electron Dynamics in High-Intensity Laser Fields

Christopher Harvey

Abstract

We consider electron dynamics in strong electromagnetic fields, such as those expected from the next generation of high-intensity laser facilities. Beginning with a review of constant classical fields, we demonstrate that the electron motion (as given by the Lorentz force equation) can be divided into one of four Lorentz invariant cases. Parameterising the field tensor in terms of a null tetrad, we calculate the radiative energy spectrum for an electron in crossed fields. Progressing to an infinite plane wave, we demonstrate how the electron orbit in the average rest frame changes from figure-of-eight to circular as the polarisation changes from linear to circular. To move beyond a plane wave one must resort to numerics. We therefore present a novel numerical formulation for solving the Lorentz equation. Our scheme is manifestly covariant and valid for arbitrary electromagnetic field configurations. Finally, we reconsider the case of an infinite plane wave from a strong field QED perspective. At high intensities we predict a substantial redshift of the usual kinematic Compton edge of the photon emission spectrum, caused by the large, intensity dependent effective mass of the electrons inside the laser beam. In addition, we find that the notion of a centre-of-mass frame for a given harmonic becomes intensity dependent.

Contents

1	Introduction	11
1.1	Background and Motivation	11
1.2	Description of the Laser Field	16
1.3	A Dimensionless Measure of Laser Intensity	19
1.4	A Brief Overview of Experimental Facilities	20
2	Electron Dynamics in Constant Fields	23
2.1	Classical Particle Motion	23
2.2	Particle Radiation	29
3	Electron Dynamics in Classical Plane Waves	36
3.1	Introduction	36
3.2	Particle Motion	39
3.3	Particle Radiation	43
4	Electron Dynamics in Arbitrary Classical Fields	46
4.1	Covariant Matrix Numerics	46
4.2	Numerical Examples	50
5	Nonlinear Compton Scattering of an Electron in a Plane Wave	55
5.1	Introduction	55
5.2	Volkov Electrons and the S-Matrix	56
5.3	Kinematics	61
5.4	Photon Emission Rates	67
5.5	The Classical Limit	86
5.6	Summary	88
6	Conclusion and Outlook	90
6.1	Summary	90
6.2	Further Developments and Outlook	94
A	Notation	97
B	The Radiation Back-Reaction	99
	Bibliography	103

List of Figures

1.1	Chirped pulse amplification	12
1.2	Description of the laser field	18
1.3	Development of the laser	21
2.1	Particle motion in constant fields	29
2.2	Scattering geometry	32
2.3	Radiation spectra for crossed fields	35
3.1	Electron trajectories in plane waves	39
3.2	Electron motion in average rest frame (linear polarisation)	41
3.3	Electron motion in average rest frame (circular polarisation)	42
3.4	Effect of polarisation on electron motion	43
3.5	Classical plane wave, angular distribution of emitted radiation	45
4.1	Numerical calculation of energies	51
4.2	Numerical error analysis	53
4.3	Numerical calculation of u^2	54
5.1	Feynman diagram for nonlinear Compton scattering	57
5.2	Relationship Mandelstam t and scattering angle	63
5.3	Relationship Mandelstam t and scattering frequency	64
5.4	Relationship between frequency and scattering angle	65
5.5	Mandelstam plot for nonlinear Compton scattering	67
5.6	Individual emission rates as a function of x	69
5.7	Total emission rate as a function of x	71
5.8	Individual emission rates as a function of frequency	72
5.9	Total emission spectrum	73
5.10	Sequence of emission spectra showing critical transition	75
5.11	Sequence of individual emission spectra	76
5.12	Centre-of-mass frames	77
5.13	Individual angular harmonics, linear	78
5.14	Individual angular harmonics, logarithmic	79
5.15	Sequence of individual angular harmonics	80
5.16	Total angular rate, logarithmic	81
5.17	Angular rate errors	82
5.18	Sequence of total angular rates	84
5.19	Angular position of emission peak	85

5.20 Quantum v. classical FZD	87
5.21 Quantum v. classical SLAC	88
6.1 Effects of beam focussing	95
B.1 Radiation damping comparison	102

Acknowledgements

I would like to thank my supervisors Tom Heinzl and Kurt Langfeld for their constant support and expert guidance throughout the last three years. Without them, Tom especially, this piece of work would not have been possible. I also express my gratitude to David McMullan and Martin Lavelle from the University of Plymouth, and to Anton Ilderton from the University of Umeå – all of whom have given me support and advice in one form or another. Finally, I would like to acknowledge Nasser Shahtahmasebi from the Ferdowsi University of Mashhad for helping me to publish my Iranian conference proceedings.

Author's Declaration

At no time during the registration for the degree of Doctor of Philosophy has the author been registered for any other University award without prior agreement of the Graduate Committee.

This study was financed with the aid of a studentship from the Engineering and Physical Sciences Research Council.

Relevant scientific seminars and conferences were attended at which work was presented. Several papers were prepared for publication.

Publications:

Scientific Papers

Signatures of High-Intensity Compton Scattering.

C. Harvey, T. Heinzl and A. Ilderton.

Phys. Rev. A **79**, 063407 (2009)

Covariant Worldline Numerics for Charge Motion with Radiation Reaction.

C. Harvey, T. Heinzl, N. Iji and K. Langfeld.

(In preparation.)

Conference Proceedings

Signatures of High-Intensity Compton Scattering.

C. Harvey, T. Heinzl and A. Ilderton.

Guest contribution to: The proceedings of the 16th Iranian Conference on Optics and Photonics, Yazd University, Iran. 26-28 January 2010.

Civilica P-1509, 327 (2010).

Presentations given:

High-Intensity Laser-Electron Interactions.

University of Umeå, Sweden.

5 January 2010.

Signatures of High-Intensity Compton Scattering.

Rutherford Appleton Laboratory, UK.

17 December 2009.

Compton Scattering in High-Intensity Laser Fields.

University of Swansea, UK.

27 November 2009.

Signatures of High-Intensity Compton Scattering.

University of Plymouth, UK.

16 June 2009.

Conferences attended:

Christmas Meeting of the High-Power Laser Science Community.

Rutherford Appleton Laboratory, UK.

16-18 December 2009.

Annual Theory Meeting.
University of Durham, UK.
18-20 December 2008.

Workshop and School on Fundamental Physics with Ultra-High Fields.
Monastery Frauenwörth, Germany.
29 September-2 October 2008.

Workshop on Ultra High-Intensity Laser Nuclear and Particle Physics.
ECT*, Trento, Italy.
23-27 June 2008.

Annual Theory Meeting.
University of Durham, UK.
17-19 December 2007.

Word count of main body of thesis: 14,200

Signed: C. Harvey
Date: 24/09/2010

Chapter 1

Introduction

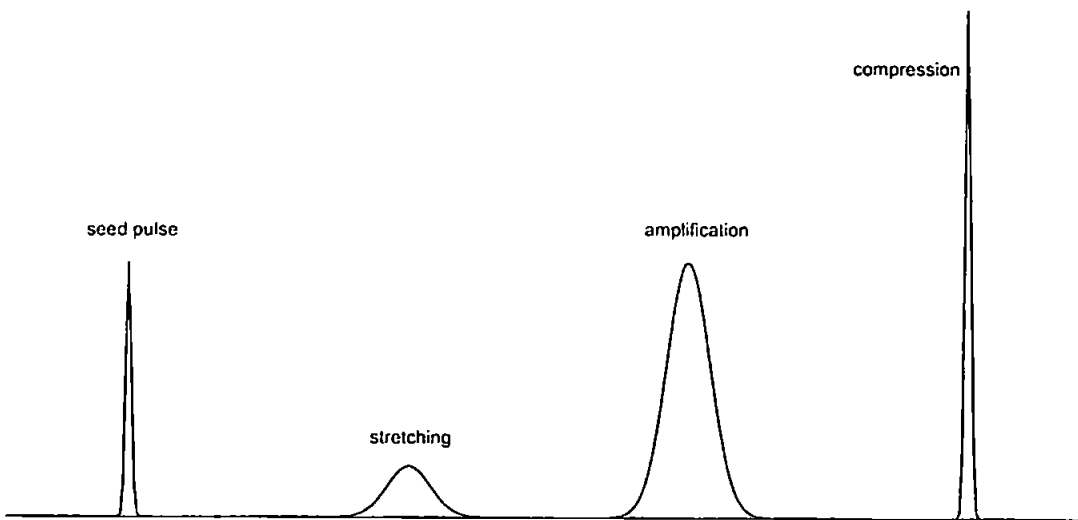
1.1 Background and Motivation

This year (2010) marks the 50th anniversary of the invention of the laser [1]. When such a device first appeared, it was cynically referred to as 'a solution looking for a problem' [1]. Since then laser technology has become essential in a vast range of areas, and there is no longer any doubt regarding its usefulness. In particular, the unique properties of a laser beam – a coherent source of photons, all in phase with each other and all of the same frequency and polarisation – make it a useful tool in many disciplines of physics [2]. It is especially interesting from a theoretical viewpoint, since the high photon density in a laser beam results in an electromagnetic field which in some ways behaves classically, even though it is produced by an inherently quantum process.

Since the first laser in 1960, various technological breakthroughs have ensured a steady increase in powers and intensities. The most important of these is chirped pulse amplification (CPA) [3, 4], which led to an acceleration of this upward trend. CPA overcomes the problem of high energy pulses causing damage as they pass through the laser optics, and therefore rendering the laser useless. It works by passing the pulse through a specially designed dispersive grating, which temporally

stretches it and thus reduces its peak power. The long duration stretched pulse then safely passes through the laser optics where it is amplified by conventional means, before being passed through a second set of gratings which temporally compress it again. This is shown diagrammatically in Figure 1.1. The advent of CPA removed a significant technological barrier, which has allowed the recent development of lasers that have unprecedented powers and intensities; the current record being about 1 PetaWatt (PW) and 10^{22} W/cm² respectively [5]. This trend is expected to continue throughout the next few years, culminating with the European Extreme Light Infrastructure (ELI), which may deliver powers and intensities as high as 1 ExaWatt and 10^{26} W/cm² [6]. Such extremely high intensities will allow the probing of fundamental physics in previously inaccessible regimes.

Figure 1.1: Diagram showing the process of chirped pulse amplification.



The utilisation of high powered laser technology can be divided into four different areas [7]: attosecond science, photonic nuclear science, laser acceleration, and vacuum physics. Attosecond science, as its name suggests, concerns the use of extremely short duration laser pulses. These may be used to track the motion of electrons on atomic scales for example [8]; allowing the behaviour of electrons in complex

biomolecules [12], and in semiconductor nanostructures to be studied. Photonic science involves the probing of atomic nuclei with laser beams. Applications include the probing of radioactive waste to test how well it has decayed [7], as well as (of course) fundamental nuclear physics. Laser acceleration refers to the possibility of using the laser's electromagnetic field to accelerate charged particles. Such technology would be extremely useful, since the current generation of conventional particle accelerators (of which the Large Hadron Collider is a prime example [9]) are large, expensive facilities, and so there is a need for a smaller and cheaper alternative. Laser accelerators could provide a solution since they will be much more compact, raising even the possibility of 'table-top' devices [10]. There may also be applications in medicine [11], one example being the use of the technology to accelerate protons. Protons can be used to destroy deep seated cancerous growths, without causing so much damage to the overlying tissues as conventional radiation therapies [13]. Much research has concerned the possibility of accelerating electrons from a plasma, such as that created when a laser is fired at a target of thin foil (see e.g. [14]). However, there is also a great deal of interest laser vacuum acceleration, where individual electrons (such as those from a conventional accelerator) are inserted into the laser field (e.g. [15]). From an experimental point of view, this would be much 'cleaner' than a laser-plasma interaction, and therefore easier to study. This brings us on to the fourth area: vacuum physics. This is the study of laser fields 'in vacuum', either on their own, or of their interaction with individual charged particles (i.e. without a plasma background). The theory describing the interaction of photons with charged particles – quantum electrodynamics (QED) – is widely accepted as one of the most, if not *the* most, successful scientific theories ever developed [16]. The high electromagnetic field intensities found inside a laser beam provide a unique testing ground for this theory, allowing us to study electromagnetic interactions under otherwise (technologically) unobtainable conditions. Strong field QED is a theory that suc-

cessfully combines relativity and quantum mechanics. The case of a charged particle in a laser field allows us to test both at the same time, since (in a strong field) the particle will be accelerated to relativistic velocities, while interacting on a quantum level with the laser photons.

In terms of vacuum physics, one of the most readily accessible processes is the electron-photon scattering that occurs when an electron is inserted into the laser beam. One way to do this is to bring the laser into collision with a beam of electrons from a conventional linear accelerator, although in many cases it may be more convenient to source the electrons from a laser wake-field induced plasma. At low intensities we have the well known Thomson/Compton scattering processes occurring, as described in any electrodynamics textbook (see e.g. Jackson [19] and Landau and Lifshitz [57]). It should be noted that Thomson scattering is the classical limit of Compton scattering, occurring in the limit where the laser photon energy $\hbar\omega$, as seen by the electron in its rest frame, is much less than the electron rest energy mc^2 . Formally, this amounts to taking $\hbar \rightarrow 0$

$$\begin{array}{ccc} & \hbar \rightarrow 0 & \\ \text{COMPTON} & \longrightarrow & \text{THOMSON} \\ & \hbar\omega \ll mc^2 & \end{array}$$

and will be considered in more detail in Chapter 5. As we move to higher intensities the scattering process can involve more than one laser photon γ_L .

$$e^- + n\gamma_L \rightarrow e^- + \gamma, \quad n \in \mathbb{N}. \quad (1.1)$$

Such a process is known as *nonlinear* Compton scattering, nonlinear because the probability for such a process (with $n > 1$) scales nonlinearly with the photon density

[20]. (We note that a considerable portion of this thesis will be devoted to the study of nonlinear Compton scattering.) At higher intensities still ($\sim 10^{25}$ W/cm²), it may be possible to study vacuum birefringence effects caused by the vacuum laser field being modified by virtual electron-positron pairs. It is predicted [21] that this will result in the laser field having a non trivial refractive index, which will be different for different polarisations of inserted probe photons. Therefore, by examining changes in the polarisation of probe photons [22], such effects could in principle be studied. However, even at ELI intensities such changes are predicted to be exceedingly small, although there is some speculation that a measurement may nevertheless be possible [23]. Looking further to the future, if a laser field could reach a critical field strength of $E_c \equiv m^2 c^3 / e \hbar$, corresponding to a critical intensity of $\sim 4 \times 10^{29}$ W/cm² (beyond even the reach of ELI), then it would contain enough energy to degenerate into electron-positron pairs (Schwinger pair production) [24, 25]. An electron inserted into such a field would acquire an electromagnetic energy equal to its rest energy mc^2 upon traversing a distance of a Compton wavelength $\lambda_c = h/mc$. While Schwinger pair production may not currently be accessible, a variant of the process (Breit-Wheeler pair production [26, 27]) is. Here the energy threshold is overcome by colliding extremely high energy photons with an (optical) laser beam. One source of such photons is of course the nonlinear Compton scattering process we have just discussed. Indeed, this method was successfully tested in the SLAC E-144 experiment [28], where pairs were produced upon colliding 30 GeV photons with an optical laser beam.

In this study we will confine ourselves to an analysis of electron-photon interactions, since it is these processes that will be most readily accessible with the facilities that are due to come online in the near future. We will analyse the electron dynamics in vacuum, rather than in a plasma, since this is a much cleaner environment in which to work. In such a system there are no additional background effects (caused

by a plasma) to take into account, and therefore the physics is more amenable to analytics. We reason that this will give us a deeper insight into the physics involved. We will be considering the situation from both a classical and a quantum perspective, with an ongoing discussion of when each of the view-points are valid.

1.2 Description of the Laser Field

Before we proceed further, let us briefly consider what a suitable description is for a laser field. We begin by enforcing the condition that any four-potential A_μ describing an electromagnetic wave ‘in vacuo’ satisfies the vacuum wave equation [17]

$$\partial_\nu \partial^\nu A_\mu = 0. \quad (1.2)$$

We write the potential in the form

$$A_\mu(x) = \text{Re} \{ a_\mu(x) e^{-i\omega t} \}. \quad (1.3)$$

Substituting (1.3) into (1.2) gives us the Helmholtz equation

$$(\nabla^2 + \omega^2) a(x) = 0. \quad (1.4)$$

If we now assume that the variation of the wave amplitude $a(\mathbf{x})$ is slow within the distance of a wavelength $\lambda = 2\pi c/\omega$, then the wave approximately maintains a plane wave character. This means that the wave front normals are paraxial rays, and so for a beam propagating in the x_3 -direction

$$\frac{\partial a}{\partial x_3} \ll \frac{\omega}{c} a \Rightarrow \frac{\partial^2 a}{\partial x_3^2} \ll \frac{\omega}{c} \frac{\partial a}{\partial x_3} \ll \frac{\omega^2}{c^2} a. \quad (1.5)$$

We can then approximate (1.4) with the paraxial approximation of the Helmholtz equation

$$\nabla_{\perp}^2 \mathbf{a} - 2i \frac{\omega}{c} \frac{\partial \mathbf{a}}{\partial x_3} = 0, \quad (1.6)$$

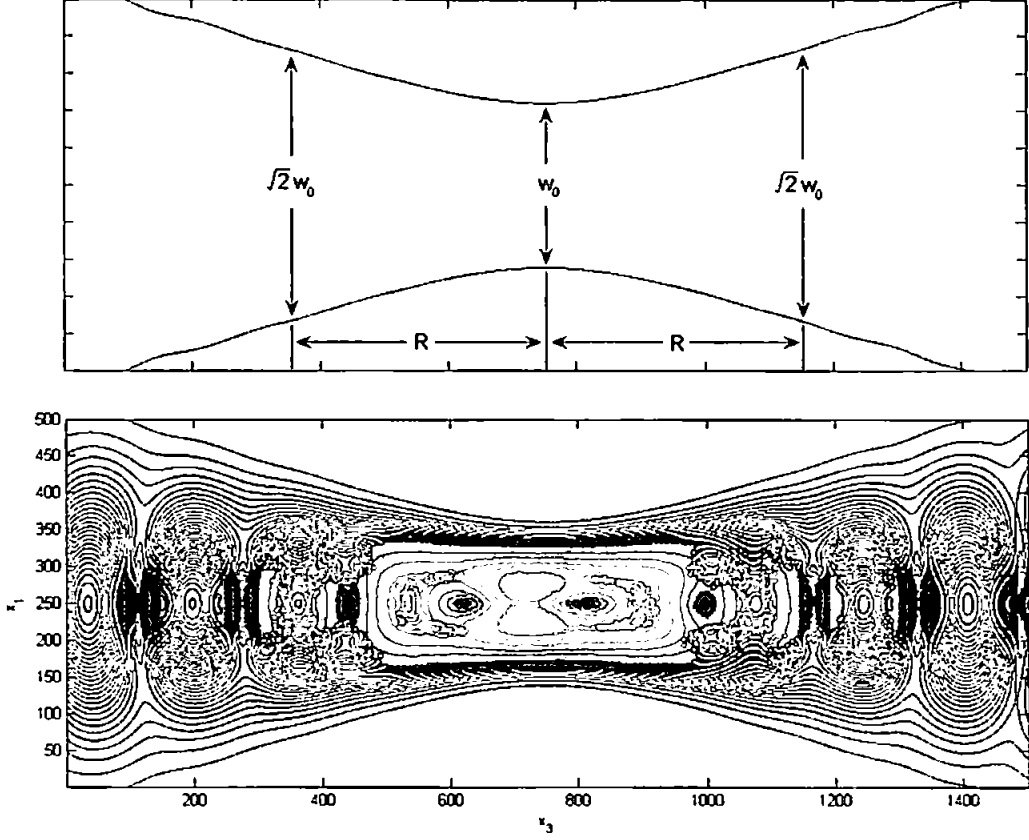
where $\nabla_{\perp}^2 = (\partial_1^2 + \partial_2^2)$. A solution to (1.6) is the Gaussian beam solution

$$a(\mathbf{x}) = \frac{w_0}{w(x_3)} \exp\left(-\frac{|\mathbf{x}_{\perp}|^2}{w^2(x_3)}\right) \exp\left(i \arctan\left(\frac{x_3}{R}\right) - i \frac{\omega |\mathbf{x}_{\perp}|^2}{2C(x_3)}\right), \quad (1.7)$$

where w_0 is the focal spot radius (beam ‘waist’ size), $w(x_3) = w_0(1 + x_3^2/R^2)^{1/2}$ is the beam radius, and the curvature of the wave fronts is given by $C(x_3) = x_3(1 + R^2/x_3^2)$, where we have introduced a quantity called the Rayleigh length $R = w_0^2 \omega / 2c$. If a Gaussian beam, such as we have just described, is focussed down to a waist and then expands again, then the rate of increase of the beam width can be considered small over a distance R from the waist [18]. This is summarised in Figure 1.2, where we also show how the electrical field intensity varies through the beam. The paraxial approximation (1.6) is only valid if $w_0/R < \mathcal{O}(1)$ [29, 30]. This is satisfied provided the beam is not too strongly focussed – for most of the parameter ranges we will consider, this is not expected to be a problem [44], although it may become an issue when considering very high-intensity facilities such as ELI.

In this study we will be devoting our attention to the case of a head-on collision between a beam of electrons and the laser. If we assume that the diameter of the electron beam is narrow compared to the laser waist size, then the electrons will only probe the central region of the laser focus. Under such conditions the Gaussian beam (1.7) can be well approximated by a (temporally) pulsed plane wave [31], which for a long duration pulse tends towards an infinite plane wave. Recent numerical modelling [44] suggests that such assumptions are justified for parameter values similar to the ones we will be considering here. An electromagnetic plane

Figure 1.2: [Top] Diagram showing the dimensions of a typical paraxial Gaussian laser beam. [Bottom] Magnitude of electrical field intensity of the beam. (Arbitrary units.)



wave is described by a field tensor satisfying the homogeneous Maxwell equation $\partial_\mu F^{\mu\nu} = 0$ and that is a function of $k \cdot x$, $F^{\mu\nu} = F^{\mu\nu}(k \cdot x)$, where k is the laser wave vector. As a result of the vacuum Maxwell equation we have

$$k_\mu \frac{\partial F^{\mu\nu}}{\partial(k \cdot x)} = 0, \quad (1.8)$$

which implies (after integrating)

$$k_\mu F^{\mu\nu} = 0, \quad (1.9)$$

expressing the fact that the wave is transverse (up to a constant homogeneous term).

We note that as we move from an infinite plane wave to a pulsed plane wave, and

from a pulsed plane wave to a Gaussian beam, the mathematical modelling increases in complexity.

1.3 A Dimensionless Measure of Laser Intensity

In order to define precisely what we mean by a ‘high-intensity’ laser field and to set the ground for later work, we need to define a measure of laser intensity. A suitable (Lorentz and gauge invariant) definition is [32]

$$a_0^2 \equiv \frac{e^2}{m^2 c^4} \frac{\langle\langle p_\mu T^{\mu\nu} p_\nu \rangle\rangle}{(k \cdot p)^2}, \quad (1.10)$$

where from now on we will take e and m to refer to the electron charge and mass. We define $k^\mu \equiv \omega(1, \mathbf{n})/c$ where ω is the laser frequency and n^μ the propagation four-vector, and we have introduced the energy momentum tensor $T^{\mu\nu}$ (see Appendix A), and the electron four-momentum $p = (E_p/c, \mathbf{p})$, where E_p is the electron energy. The brackets $\langle\langle \dots \rangle\rangle$ denote the proper time average. In the electron rest frame we have $p = (mc, \mathbf{0})$ and thus

$$p_\mu T^{\mu\nu} p_\nu = m^2 c^2 T^{00} = \frac{m^2 c^2}{2} (E^2 + B^2). \quad (1.11)$$

For a plane wave type field, $k \cdot p \sim m\omega$, and so a_0 will recover the non-Lorentz covariant form

$$a_0 = \frac{e E_{\text{rms}}}{\omega m c} = \frac{e E_{\text{rms}} \lambda_L}{m c^2}. \quad (1.12)$$

typically used in the literature. Here $E_{\text{rms}} \equiv \langle E^2 \rangle^{1/2}$ the root mean squared (rms) electric field and we have introduced the laser wavelength $\lambda \equiv c/\omega$. From this definition it can be seen that a_0 can be considered as the ratio of two energies – the

ratio of the energy gain of the electron as it moves over a laser wavelength with the electron's rest energy. We point out that the absence of any factors of \hbar in (1.10) and (1.12) indicate that a_0 is a purely classical quantity. At the same time, the presence of the velocity of light c indicates the relativistic nature of a_0 . It is clear that $a_0 > 1$ describes the regime where the electrons become relativistic. Finally, we note a convenient rule-of-thumb to express a_0 in terms of the laser intensity I [27]

$$a_0^2 \approx 3.7 \times 10^{-19} I \lambda^2, \quad (1.13)$$

for I in Watts/cm² and λ in μm . We are now in a position to introduce some examples of laser facilities.

1.4 A Brief Overview of Experimental Facilities

There is currently a growing interest in using high-powered lasers to test fundamental physics (see e.g. [8]). This is leading to a proliferation of new facilities where such experiments can be conducted. Some of the most relevant to us are the following:

Daresbury At the Daresbury laboratory in northern England there are currently experiments taking place with an order 10 TW laser, $a_0 \approx 1$, and a linear accelerator delivering electrons of energy 35 MeV (giving them a relativistic γ -factor of $\gamma \approx 70$) [33].

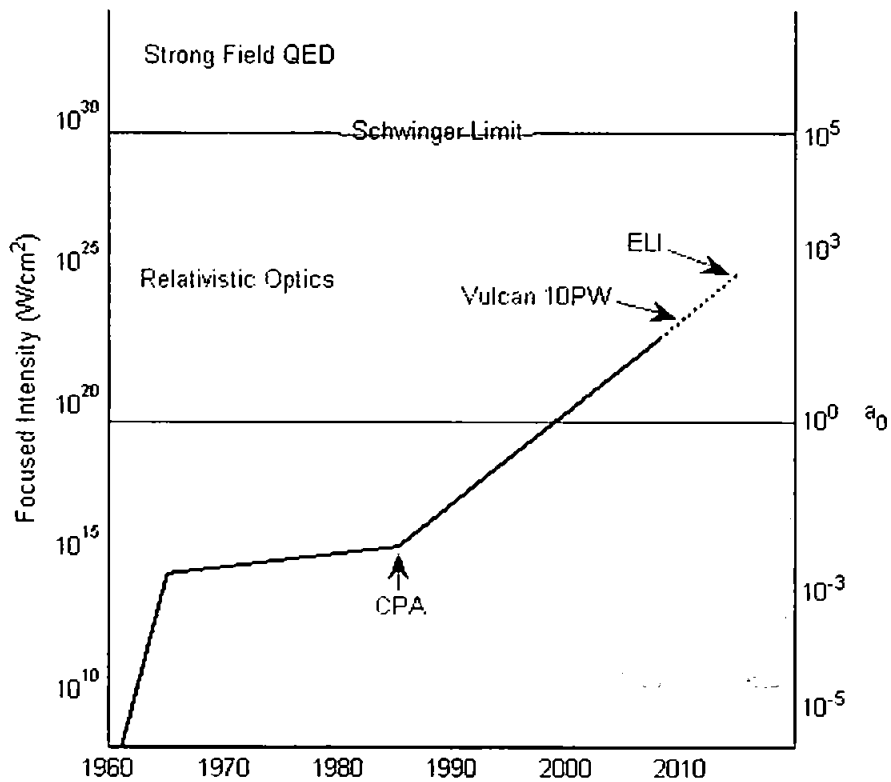
FZD The facility that will feature most extensively in our subsequent discussions is the Forschungszentrum Dresden Rossendorf (FZD) in Germany [34]. This facility has a 150 TW laser giving an $a_0 \approx 20$. There is also a linear accelerator ('ELBE') that can deliver 40 MeV electrons ($\gamma \approx 10^2$). Compton scattering experiments are

due to begin here later this year (2010). We shall often use these parameters in subsequent discussions, referring to them simply as ‘FZD values’.

Vulcan The UK’s Rutherford Appleton Laboratory’s Vulcan laser [35] is currently 1 PW ($a_0 \approx 70$). However, it has recently been announced [36] that it is to be upgraded to 10 PW, increasing its a_0 to 200.

ELI Looking to the future, the European Extreme Light Infrastructure (ELI) project has been initiated [6]. When this is completed it potentially could deliver an $a_0 \sim 5000$, giving us an increase of two orders of magnitude compared to current facilities.

Figure 1.3: Chart showing the development of the laser as a function of time, together with examples of the physics that are accessible at given intensities.



In the table below we give a summary of some of these facilities.

	I [W/cm ²]	a_0
FZD (150TW), Germany	10^{21}	20
Vulcan (1PW), UK	10^{22}	70
Vulcan Upgrade (10PW)	10^{23}	200
ELI	10^{26}	~ 5000

In Figure 1.4 we chart the development of the laser, showing how intensities have increased over time. It shows clearly the impact of CPA, and also how laser intensities are predicted to increase over the next few years.

In this thesis we will study the phenomenology of electron-laser interactions, including the properties of the scattered radiation. In particular, we will be considering the angular and frequency dependence of the scattered radiation, looking for possible experimental signatures of intensity dependence. Note that from here on, except where stated otherwise, we will adopt ‘natural’ units where $\hbar = c = 1$.

Chapter 2

Electron Dynamics in Constant Fields

We begin with the simplest possible case – that of an electron in a constant classical background field. The behaviour of particles in such fields can be obtained analytically, and so will serve as a good starting point from which to consider more complex field configurations.

2.1 Classical Particle Motion

The classical equation of motion for an electron in an arbitrary background field is given by the differential equation (the Lorentz force equation) [37]

$$\dot{p}^\mu = m\ddot{x}^\mu = \frac{e}{m}F^{\mu\nu}(x)p_\nu. \quad (2.1)$$

where the dot denotes differentiation with respect to proper time τ , and we have introduced the electromagnetic field tensor

$$F_{\mu\nu} = \begin{pmatrix} 0 & E_1 & E_2 & E_3 \\ -E_1 & 0 & -B_3 & B_2 \\ -E_2 & B_3 & 0 & -B_1 \\ -E_3 & -B_2 & B_1 & 0 \end{pmatrix}. \quad (2.2)$$

Equation (2.1) is a covariant generalisation of Newton's second law. We wish to solve it to find the particle trajectory $x^\mu(\tau)$. Note that equation (2.1) is only valid under the assumption that any radiative back reaction effects have negligible impact on the particle's motion. We adopt this assumption for the moment, but it is something that we will re-visit later.

In the case of constant fields the field tensor $F^{\mu\nu}$ will be constant, and so (2.1) will be linear and therefore solvable directly by exponentiation. Writing $F^{\mu\nu}$ in matrix form as \mathbb{F} , the solution is

$$p = \exp\left(\frac{e}{m}\mathbb{F}\tau\right)p_0 \equiv \mathbb{A}p_0, \quad (2.3)$$

where p_0 is the initial four-momentum of the electron and the matrix \mathbb{F} has one index up and one down. Due to the antisymmetry of \mathbb{F} , we note that \mathbb{A} is a Lorentz transformation matrix.

Now that we have the four-velocity $u = p/m$, the particle trajectory can be found simply by integrating (2.3). However, we can gain more insight into the properties of the particle orbits by first considering the eigenvalues of \mathbb{F} . In [38] Taub shows how these can be expressed in terms of the scalar and pseudo-scalar invariants of

the field strength tensor,

$$S = -\frac{1}{2}F_{\mu\nu}F^{\mu\nu} = E^2 - B^2, \quad (2.4)$$

$$\mathcal{P} = -\frac{1}{4}F_{\mu\nu}\tilde{F}^{\mu\nu} = \mathbf{E} \cdot \mathbf{B}, \quad (2.5)$$

where $\tilde{F}^{\mu\nu}$ is the dual tensor.

We find that there are four cases and they can be classified in a Lorentz invariant way, according to the values of S and \mathcal{P} ,

$$S = \mathcal{P} = 0, \quad E^2 = B^2, \quad \mathbf{E} \cdot \mathbf{B} = 0 \quad (2.6)$$

$$S < 0, \mathcal{P} = 0, \quad B^2 > E^2, \quad \mathbf{E} \cdot \mathbf{B} = 0 \quad (2.7)$$

$$S > 0, \mathcal{P} = 0, \quad E^2 > B^2, \quad \mathbf{E} \cdot \mathbf{B} = 0 \quad (2.8)$$

$$S \neq 0, \mathcal{P} \neq 0, \quad E^2 - B^2 \neq 0, \quad \mathbf{E} \cdot \mathbf{B} \neq 0 \quad (2.9)$$

We will find that case (2.6) results in particle orbits that are *parabolic*, case (2.7) *elliptic*, case (2.8) *hyperbolic* and case (2.9) *loxodromic*.

It is possible to parameterise the field tensor $F^{\mu\nu}$ in terms of constant 4-vectors chosen from a null tetrad [39]. (We will see in the next chapter that such a formalism will also allow us to parameterise plane wave type fields in terms of a 'light-cone time' $n \cdot x$.) Here we will adopt the null tetrad $(n^\mu, \bar{n}^\mu, e_1, e_2)$ where the propagation vectors n, \bar{n} and polarisation vectors e_1, e_2 are defined as

$$n^\mu = (1, 0, 0, 1) \quad (2.10)$$

$$\bar{n}^\mu = (1, 0, 0, -1) \quad (2.11)$$

$$e_1^\mu = (0, 1, 0, 0) \quad (2.12)$$

$$e_2^\mu = (0, 0, 1, 0). \quad (2.13)$$

Clearly n and \bar{n} are light-like and ϵ_1 and ϵ_2 are space-like. The only non-vanishing scalar products are

$$n \cdot \bar{n} = 2 \quad (2.14)$$

$$\epsilon_1^2 = \epsilon_2^2 = -1. \quad (2.15)$$

We take this opportunity to introduce the notation

$$a^- \equiv n^\mu a_\mu = a^0 - a^3, \quad (2.16)$$

$$a^+ \equiv \bar{n}^\mu a_\mu = a^0 + a^3, \quad (2.17)$$

for an arbitrary four-vector a ; this will be useful to us in later work.

Using the vectors from the tetrad, for each case we construct the 'standard form' of the field tensor

$$F_1^{\mu\nu} = F_1(n^\mu \epsilon_2^\nu - n^\nu \epsilon_2^\mu) = F_1 \begin{pmatrix} 0 & 0 & 1 & 0 \\ 0 & 0 & 0 & 0 \\ -1 & 0 & 0 & -1 \\ 0 & 0 & 1 & 0 \end{pmatrix} \quad (2.18)$$

$$F_2^{\mu\nu} = F_2(\epsilon_2^\mu \epsilon_2^\nu - \epsilon_1^\mu \epsilon_1^\nu) = F_2 \begin{pmatrix} 0 & 0 & 0 & 0 \\ 0 & 0 & 1 & 0 \\ 0 & -1 & 0 & 0 \\ 0 & 0 & 0 & 0 \end{pmatrix} \quad (2.19)$$

$$F_3^{\mu\nu} = F_3(n^\mu \bar{n}^\nu - n^\nu \bar{n}^\mu) = F_3 \begin{pmatrix} 0 & 0 & 0 & -2 \\ 0 & 0 & 0 & 0 \\ 0 & 0 & 0 & 0 \\ 2 & 0 & 0 & 0 \end{pmatrix} \quad (2.20)$$

$$F_4^{\mu\nu} = F_2^{\mu\nu} + F_3^{\mu\nu}. \quad (2.21)$$

The tensors $F_{1,\dots,4}^{\mu\nu}$ defined above are representative of each of the four cases. Any other tensor of the same case can be generated by a Lorentz transform.

By comparing directly with (2.2) we see that: the tensor $F_1^{\mu\nu}$ describes the case of crossed fields (i.e. perpendicular \mathbf{E} and \mathbf{B} fields of equal strength), the tensor $F_2^{\mu\nu}$ describes a constant magnetic \mathbf{B} field, the tensor $F_3^{\mu\nu}$ describes a constant electric \mathbf{E} field, and the final case $F_4^{\mu\nu}$ is a linear sum of cases 1 and 2.

Exponentiating to find the corresponding Lorentz transformation matrices Λ , we find

$$(\Lambda_1)^\mu{}_\nu = \begin{pmatrix} 1 + \frac{1}{2}\left(\frac{e}{m}F_1\tau\right)^2 & 0 & -\frac{e}{m}F_1\tau & \frac{1}{2}\left(\frac{e}{m}F_1\tau\right)^2 \\ 0 & 1 & 0 & 0 \\ -\frac{e}{m}F_1\tau & 0 & 1 & -\frac{e}{m}F_1\tau \\ -\frac{1}{2}\left(\frac{e}{m}F_1\tau\right)^2 & 0 & \frac{e}{m}F_1\tau & 1 - \frac{1}{2}\left(\frac{e}{m}F_1\tau\right)^2 \end{pmatrix} \quad (2.22)$$

$$(\Lambda_2)^\mu{}_\nu = \begin{pmatrix} 1 & 0 & 0 & 0 \\ 0 & \cos\left(\frac{e}{m}F_2\tau\right) & -\sin\left(\frac{e}{m}F_2\tau\right) & 0 \\ 0 & \sin\left(\frac{e}{m}F_2\tau\right) & \cos\left(\frac{e}{m}F_2\tau\right) & 0 \\ 0 & 0 & 0 & 1 \end{pmatrix} \quad (2.23)$$

$$(\Lambda_3)^\mu{}_\nu = \begin{pmatrix} \cosh\left(2\frac{e}{m}F_3\tau\right) & 0 & 0 & \sinh\left(2\frac{e}{m}F_3\tau\right) \\ 0 & 1 & 0 & 0 \\ 0 & 0 & 1 & 0 \\ \sinh\left(2\frac{e}{m}F_3\tau\right) & 0 & 0 & \cosh\left(2\frac{e}{m}F_3\tau\right) \end{pmatrix} \quad (2.24)$$

$$(\Lambda_4)^\mu{}_\nu = \begin{pmatrix} \cosh\left(2\frac{e}{m}F_3\tau\right) & 0 & 0 & \sinh\left(2\frac{e}{m}F_3\tau\right) \\ 0 & \cos\left(\frac{e}{m}F_2\tau\right) & -\sin\left(\frac{e}{m}F_2\tau\right) & 0 \\ 0 & \sin\left(\frac{e}{m}F_2\tau\right) & \cos\left(\frac{e}{m}F_2\tau\right) & 0 \\ \sinh\left(2\frac{e}{m}F_3\tau\right) & 0 & 0 & \cosh\left(2\frac{e}{m}F_3\tau\right) \end{pmatrix}. \quad (2.25)$$

Examining these matrices in sequence, we firstly see that the crossed field tensor $F_1^{\mu\nu}$ results in motion that is *parabolic*. (We note that in the crossed field case, the \mathbf{E} and \mathbf{B} fields will remain perpendicular and equal in magnitude in any given frame.) Next we see that the constant magnetic field tensor $F_2^{\mu\nu}$ results in circular (*elliptical*) motion. The case of the purely magnetic field is the only one with periodic orbits (i.e. the motion is bound, meaning that there is no net acceleration). As an aside, we note that for other tensors in this class, the resulting electron motion will be in an ellipse with eccentricity $\epsilon = E/B$ [41], moving perpendicularly to both the electric and magnetic fields. Moving to the third case we find that the constant electric field tensor $F_3^{\mu\nu}$ results in motion that is *hyperbolic*. The final case, $\Lambda_4^{\mu\nu}$, is a linear sum of $\Lambda_2^{\mu\nu}$ and $\Lambda_3^{\mu\nu}$. The particle motion is a superposition of cases (2) and (3) and is *loxodromic*.

Note that our $F_1^{\mu\nu}$ field tensor is an example of a null field [39], since both its scalar and pseudo-scalar invariants \mathcal{S} and \mathcal{P} are zero. Calculating the first few powers of $F_1^{\mu\nu}$ we find (using (2.14) and (2.15) and omitting the index 1 for ease of notation)

∴

$$F^2 = F^\mu{}_\alpha F^\alpha{}_\nu = n^\mu n_\nu, \quad (2.26)$$

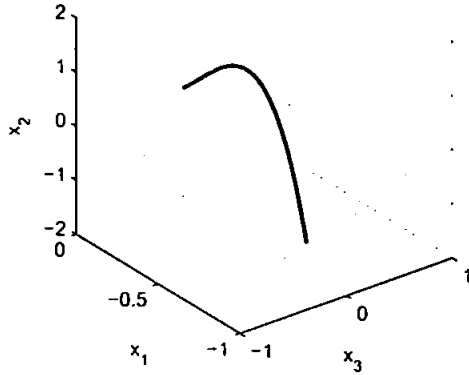
$$F^3 = F^\mu{}_\alpha F^\alpha{}_\beta F^\beta{}_\nu = n^\mu n_\beta F^\beta{}_\nu = 0, \quad (2.27)$$

where the second result is due to the transversality of the field. Hence $F_1^{\mu\nu}$ is nilpotent of degree 3, which is why the exponential series in $\Lambda_2^{\mu\nu}$ is truncated to just three terms. Thus the parabolic nature of the particle orbits.

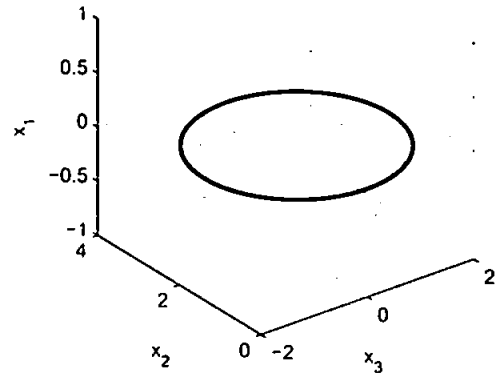
Figure (2.1) shows the motion of a charged particle in each of the four cases. The trajectories are as we would expect for the respective fields.

Figure 2.1: Plots showing the motion of a charged particle in each of the four cases. Plot a) shows parabolic motion in crossed fields. Plot b) shows elliptical motion in a magnetic field. Plot c) shows hyperbolic motion in an electrical field. Plot d) shows loxodromic motion in combined electric and magnetic fields. (Arbitrary units.)

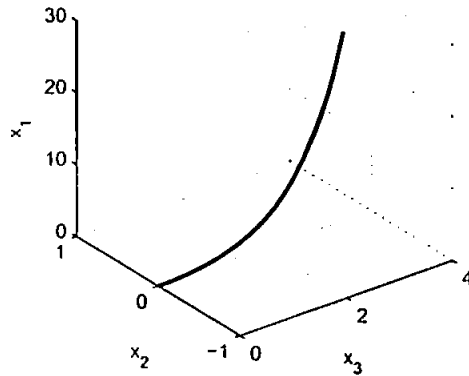
a) F_1 (Crossed fields - magnetic in x_1 , electric in x_2 -direction)



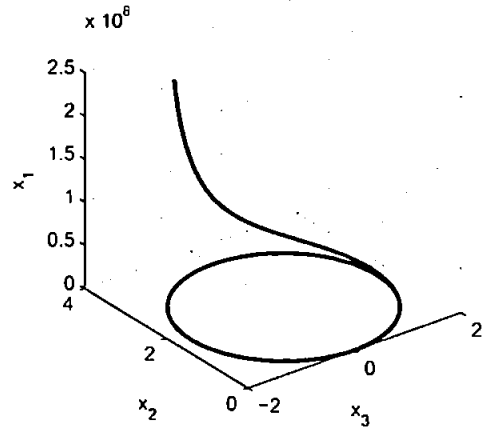
b) F_2 (Magnetic field in x_3 -direction)



c) F_3 (Electric field in x_3 -direction)



d) F_4 (Electric and magnetic fields both in x_3 -direction)



2.2 Particle Radiation

A particle undergoing acceleration will radiate and the properties of this radiation are of interest to us in this study. The calculation of the classical radiation spectrum of an accelerating particle is covered in most electrodynamics textbooks (e.g. [19], [37]), although in most cases the problem is not treated covariantly. A fully covariant discussion is however given by Mitter in [43], and further explored in [11]. The

radiation four-momentum may be expressed

$$P^\nu = \int d^4x \partial_\mu T^{\mu\nu}. \quad (2.28)$$

Employing the energy-momentum balance equation $\partial_\mu T^{\mu\nu} = j_\mu F^{\mu\nu}$, we have

$$P^\nu = \int d^4x j_\mu F^{\mu\nu}. \quad (2.29)$$

Now

$$j_\mu F^{\mu\nu} = j_\mu \partial^\mu A^\nu - j_\mu \partial^\nu A^\mu, \quad (2.30)$$

$$= \partial^\mu (j_\mu A^\nu) - A^\nu \partial^\mu j_\mu - j_\mu \partial^\nu A^\mu. \quad (2.31)$$

The second term is zero due to the continuity equation $\partial^\mu j_\mu = 0$, and when integrated the first term also disappears, leaving us with

$$P^\nu = - \int d^4x j_\mu \partial^\nu A^\mu. \quad (2.32)$$

From the Maxwell equations (in the Lorentz gauge) we have, in integral form,

$$A^\mu(x) = 4\pi \int d^4y D_{\text{ret}}(x-y) j^\mu(y), \quad (2.33)$$

where $D_{\text{ret}}(x-y)$ is the retarded Green's function which, upon inserting into (2.32), gives

$$P^\mu = -4\pi \int d^4x j_\mu(x) \int d^4y j^\nu(y) \partial^\nu D_{\text{ret}}(x-y). \quad (2.34)$$

We can replace the integrand

$$\partial^\nu D_{\text{ret}}(x-y) \rightarrow \frac{1}{2} (\partial^\nu(x) D_{\text{ret}}(x-y) + \partial^\nu(y) D_{\text{ret}}(y-x)), \quad (2.35)$$

which amounts to nothing more than renaming the variables of integration. Then introducing the advanced potential via

$$\partial^\nu(y) D_{\text{ret}}(y-x) = -\partial^\nu(x) D_{\text{av}}(x-y), \quad (2.36)$$

and defining

$$D \equiv D_{\text{ret}} - D_{\text{av}}, \quad (2.37)$$

we have

$$P^\nu = -2\pi \int d^4x d^4y j_\mu(x) j^\mu(y) \partial^\nu D(x-y). \quad (2.38)$$

In a Fourier representation this becomes

$$P^\nu = -\frac{1}{(2\pi)^3} \int d^4k' \text{sgn}(k'^0) \delta(k'^2) k'^\nu \tilde{j}^\mu(k') \tilde{j}_\mu^*(k'). \quad (2.39)$$

where \tilde{j}_μ is the four-dimensional Fourier integral of the current

$$\tilde{j}_\mu(k') = \int d^4x j_\mu(x) \exp(ik' \cdot x). \quad (2.40)$$

and from here on we will drop the tilde in order to simplify the notation. We can interpret $k' = \omega'(1, \mathbf{n}')$ as the scattered radiation wave vector, with frequency ω' in direction \mathbf{n}' . It is the 0-component of P^μ that gives us the radiated energy.

Performing the k^0 integration in (2.39) and converting to polar coordinates, we find

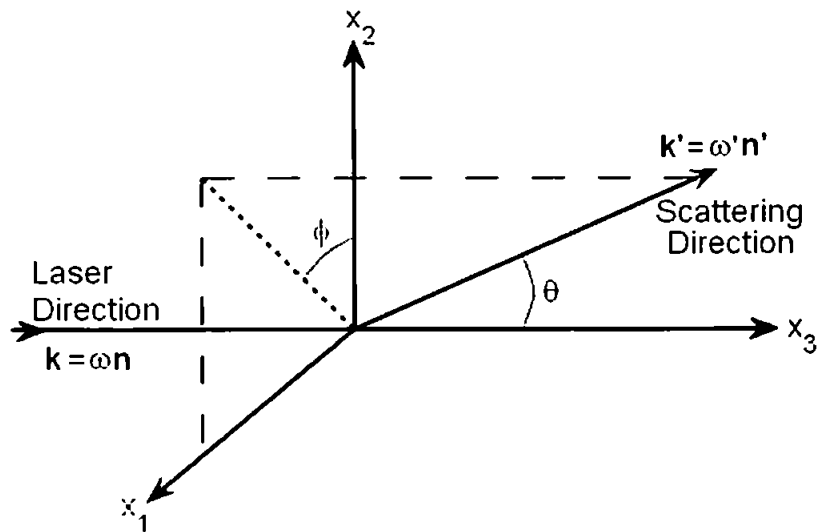
$$P^0 = -\frac{1}{16\pi^3} \int d\omega' d\Omega (\omega')^2 j(k') \cdot j^*(k'), \quad (2.41)$$

$$\equiv \int d\omega' d\Omega \rho(\omega', \mathbf{n}), \quad (2.42)$$

where $\rho(\omega', \mathbf{n}')$ is the spectral density describing the amount of radiation per unit frequency $d\omega'$, per unit solid angle $d\Omega$.

In the case of the constant fields we are considering, the Fourier integrals (2.40) (and thus the radiated energy P^0) can be calculated exactly, although the calculations themselves are somewhat tedious. We choose here to focus our attention on just one of the cases – that of crossed fields. There are two reasons for this. Firstly, the other cases are more commonly explored in electrodynamics textbooks, whereas the crossed field case is not (see e.g. Jackson [19], Landau and Lifshitz [37]). Secondly and most importantly, the crossed field case is, out of the four cases, the one that describes a laser beam most closely. Crossed fields describe either the high-intensity or the long wavelength limit of a linearly polarised plane wave, which we will consider in the next chapter.

Figure 2.2: Geometry of the scattered radiation.



To begin the calculation we must first define the geometry, which is that given in Figure 2.2. To simplify matters somewhat we will limit ourselves to a consideration of the ‘head-on’ case only. Thus for a crossed field with electric component in the x_1 direction and magnetic in x_2 , the electron will have an initial four-velocity of

$$u_0 = \gamma(1, 0, 0, -\beta). \quad (2.43)$$

To evaluate the integral (2.41) we first need to find the electron’s velocity $u^\mu(\tau)$ and trajectory $x^\mu(\tau)$. These we find by solving the Lorentz equation (2.1). From (2.22) it is clear that $u^\mu(\tau)$ will be quadratic in τ and $x^\mu(\tau)$ cubic. Before we calculate the spectral density ρ , we can make use of some features of the light-cone formalism we have adopted. One property of this formalism is that we can write the norm of the four-current as [45]

$$j \cdot j^* = \frac{1}{2}j^+j^{-*} + \frac{1}{2}j^-j^{+*} - |j_\perp|^2. \quad (2.44)$$

Now, the current conservation equation $k' \cdot j = 0$ allows us to eliminate j^+ from (2.44) giving

$$j \cdot j^* = 2\frac{k'_\perp}{k'^-}\text{Re}(j_\perp j^{-*}) - \frac{k'^+}{k'^-}|j^-|^2 - |j_\perp|^2. \quad (2.45)$$

We begin our calculation of $\rho(\omega', \mathbf{n}')$ by finding $j^-(k')$. From the discussion above, we know that the argument of the exponential in (2.40) is going to be a cubic polynomial, and thus we expect to obtain an Airy function in our solution. The prefactor is proportional to $u^- = u^0 - u^3 = \text{const}$ and so we find

$$j^-(k') = e\gamma(1 + \beta)\exp(iB_2) \int_{-\infty}^{\infty} dx^- \exp(i(b_3\tau^3 + B_1\tau)) \quad (2.46)$$

$$= 2e\gamma(1 + \beta)\exp(iB_2) \int_0^{\infty} dx^- \cos(-b_3\tau^3 - B_1\tau). \quad (2.47)$$

where

$$B_1 = \frac{3b_1b_3 - b_2^2}{3b_3}, \quad B_2 = \frac{2b_2^2 - 9b_1b_2b_3}{27b_3^2}, \quad (2.48)$$

and

$$b_1 = -\frac{1}{2}\gamma((1+\beta)k^+ + (1-\beta)k^-), \quad (2.49)$$

$$b_2 = \gamma(1+\beta)\frac{eE}{2m}k_1, \quad (2.50)$$

$$b_3 = -\gamma(1+\beta)\frac{e^2E^2}{6m^2}k^-. \quad (2.51)$$

Employing standard identities (see e.g. [46]), we find we may indeed express j^- in terms of the Airy function Ai .

$$j^-(k') = 2e\gamma(1+\beta)\exp(iB_2)\left((3b_3)^{-\frac{1}{3}}\pi\text{Ai}(Z)\right), \quad (2.52)$$

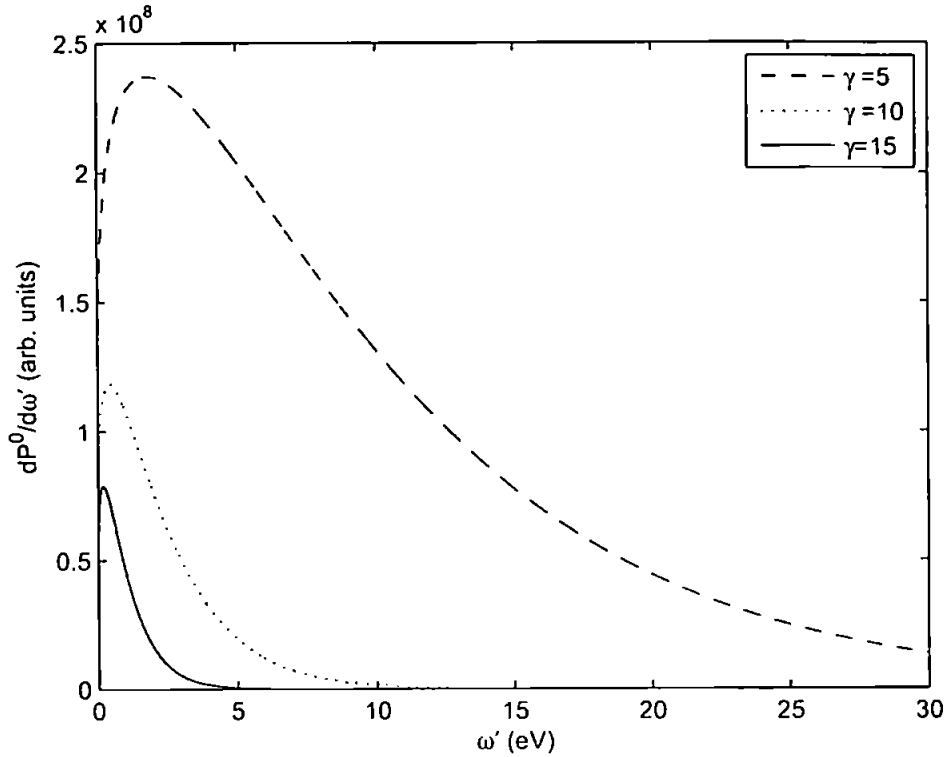
where $Z = (3b_3)^{-1/3}B_1$. So now we are just left with finding $j_\perp = (j_1, j_2)$. From our expression for u_2 we find immediately that $j_2 = 0$. Thus all that remains is to find j_1 . In the case of crossed fields we find that we can express j_1 in terms of the k^+ derivative of j^-

$$j^1 = 2i\frac{eE}{m}\frac{1}{\gamma(1+\beta)}\frac{\partial}{\partial k^+}(j^-(k')) \quad (2.53)$$

$$= 2\pi\frac{e^2E}{m}\gamma(1+\beta)(3b_3)^{-1/3}\exp(iB_2)\left(i(3b_3)^{-1/3}\text{Ai}(Z)' - \frac{1}{3}\frac{b_2}{b_3}\text{Ai}(Z)\right) \quad (2.54)$$

We now have everything we require to calculate (2.44) and hence the radiated energy P^0 . Doing so, we find that the radiation is almost exclusively confined to the $\theta = \pi$ (back scattering) direction. In Figure 2.2 we show the radiation spectrum for various initial electron γ -factors. We see that the signal strength of the radiated energy decreases as the electron γ -factor increases, while at the same time the peak

Figure 2.3: Radiated energy spectra for an electron in constant crossed fields. Interaction is considered 'head-on', with initial γ -factors as indicated. Evaluated at $\theta = \pi$.



emitted frequency also decreases (is red-shifted).

Now that we have given detailed consideration to the behaviour of an electron in the four cases of constant electromagnetic fields and, in particular, having calculated the radiation spectra for an electron in crossed fields, we are ready to move on to consider plane wave backgrounds. Plane wave fields are the next step up in realism and complexity in our modelling of a laser beam.

Chapter 3

Electron Dynamics in Classical Plane Waves

3.1 Introduction

Having studied the dynamics of electrons in constant fields, we are now ready to consider the case of a time dependent infinite plane wave. Specifically, we consider the case where we have (time dependent) electric and magnetic components in the transverse (x_1, x_2) directions, while the wave propagates in the longitudinal (x_3) direction. Such a field may be described by the field strength tensor

$$F^{\mu\nu}(x) = F_1(k \cdot x) f_1^{\mu\nu} + F_2(k \cdot x) f_2^{\mu\nu}, \quad (3.1)$$

where the constant tensors f_j are defined

$$f_j^{\mu\nu} \equiv n^\mu \epsilon_j^\nu - n^\nu \epsilon_j^\mu. \quad (3.2)$$

We note that the tensors $f_j^{\mu\nu}$ are examples of crossed field tensors, like $F_1^{\mu\nu}$ in the previous chapter. Since the scalar and pseudo-scalar invariants vanish for such fields, our plane wave tensor (3.1) is a null field. The field amplitudes F_j depend

on the Lorentz invariant phase $k \cdot x$ where, as previously, k is the laser wave vector $k^\mu = \omega n^\mu$. Applying the Lorentz force equation

$$\dot{u}^\mu = \frac{e}{m} F^{\mu\nu} (k \cdot x) u_\nu, \quad (3.3)$$

we find that $k \cdot u$ is conserved in proper time τ

$$\frac{d(k_\mu u^\mu)}{d\tau} = \frac{e}{m} k_\mu F^{\mu\nu} u_\nu \quad (3.4)$$

$$= 0, \quad (3.5)$$

where we have made use of (2.27) and the fact that plane waves are transverse.

Integrating (3.4) we find

$$k \cdot x = \tau k \cdot u \quad (3.6)$$

$$\tau = \frac{k \cdot x}{k \cdot u}, \quad (3.7)$$

where we have assumed the electron is initially at the origin ($x_0 = 0$). Hence we see that the 'light-cone time' $n \cdot x$ is directly proportional to the proper time τ . This means that we can trade the x dependence in (3.1) for proper time τ , and so the equation of motion (3.3) becomes linear and thus solvable by exponentiation.

So, from equation (2.1) we have

$$\frac{d^2 x}{d\tau^2} = \frac{e}{m} (F_1(\tau) f_1 + F_2(\tau) f_2) \frac{dx}{d\tau}. \quad (3.8)$$

which has solution

$$\frac{dx}{d\tau} = \exp\left(\frac{e}{m}(G_1(\tau)f_1 + G_2(\tau)f_2)\right) u_0. \quad (3.9)$$

where

$$G_j(\tau) = \int_{\tau_0}^{\tau} d\tau' F_j(\tau'). \quad (3.10)$$

and u_0 is the initial 4-velocity at time $\tau = \tau_0$. Using the fact that the F_j are linearly independent together with result (2.27), we have

$$\frac{dx}{d\tau} = \left[\mathbf{1} + \frac{e}{m} (G_1(\tau)f_1 + G_2(\tau)f_2) + \frac{e^2}{2m^2} (G_1^2(\tau)f_1^2 + G_2^2(\tau)f_2^2) \right] u_0. \quad (3.11)$$

Integrating to find the particle trajectory, we have (explicitly)

$$\begin{aligned} x^0 &= x_0^0 + u_0^0(\tau - \tau_0) - \frac{e}{m} (u_0^1 H_1(\tau) - u_0^2 H_2(\tau)) + \frac{e^2}{2m^2} (n \cdot u) \int_{\tau_0}^{\tau} d\tau' G_1^2 + G_2^2, \\ x^1 &= x_0^1 + u_0^1(\tau - \tau_0) - \frac{e}{m} (n \cdot u) H_1(\tau), \\ x^2 &= x_0^2 + u_0^2(\tau - \tau_0) - \frac{e}{m} (n \cdot u) H_2(\tau), \\ x^3 &= x_0^3 + u_0^3(\tau - \tau_0) - \frac{e}{m} (u_0^1 H_1(\tau) - u_0^2 H_2(\tau)) + \frac{e^2}{2m^2} (n \cdot u) \int_{\tau_0}^{\tau} d\tau' G_1^2 + G_2^2, \end{aligned}$$

where we have defined $H_j(\tau)$ such that

$$H_j(\tau) \equiv \int_{\tau_0}^{\tau} d\tau' G_j(\tau') = \int_{\tau_0}^{\tau} d\tau' \int_{\tau_0}^{\tau'} d\tau'' F_j(\tau''). \quad (3.12)$$

These equations describe the motion of a particle in a transverse field given by any field tensor satisfying (3.1) and, for an infinite plane wave, agree with the expressions found by Taub [38].

We will now use these results to study the behaviour of electrons in infinite plane waves, considering various polarisations. For infinite plane waves, the integrals (3.12) are solvable analytically, and so we can find the electron trajectory without having to resort to numerics.

3.2 Particle Motion

To be specific, we will focus our attention on the plane wave field defined as follows

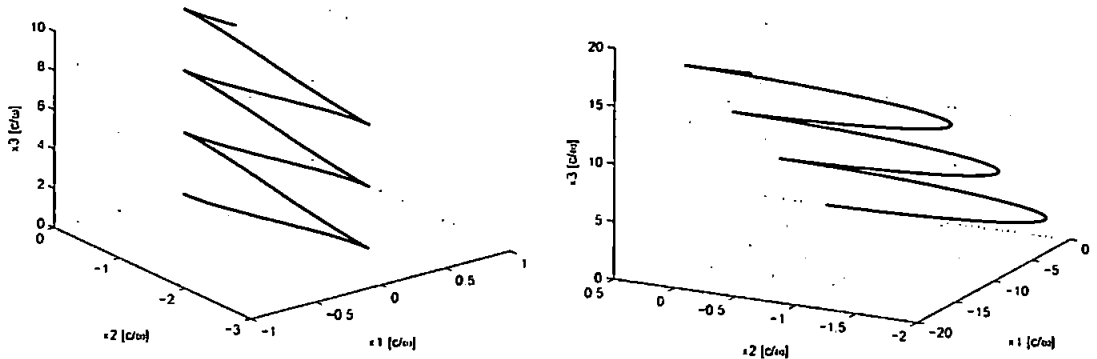
$$F_1 = \delta A \sin \omega\tau, \quad (3.13)$$

$$F_2 = \sqrt{1 - \delta^2} A \cos \omega\tau. \quad (3.14)$$

Here A is the wave amplitude and the wave polarisation is encoded in the parameter δ . Linear polarisation corresponds to $\delta = 0, \pm 1$; circular polarisation to $\delta = \pm 2^{(-1/2)}$. Other values of δ correspond to varying degrees of elliptical polarisation. Regardless of the choice of δ , the rms electric field averaged over one laser cycle is $E_{\text{rms}} = A/\sqrt{2}$. This means that we can write the laser intensity (1.12) as

$$a_0 = \frac{eA}{\sqrt{2}\omega m}. \quad (3.15)$$

Figure 3.1: Electron trajectory in a plane wave of linear polarisation [left plot] and circular polarisation [right plot]. Laser intensity is $a_0 = 1$ and the particle is initially at rest.



We once again consider the case of a head-on collision between the electron and

the laser field

$$k = \omega(1, 0, 0, 1) = \omega(1, \hat{z}), \quad (3.16)$$

$$u_0 = \gamma(1, 0, 0, -\beta) = \gamma(1, -\beta\hat{z}). \quad (3.17)$$

Plots of typical trajectories for the linear and circular cases are shown in Figure 3.1. It can be seen from these plots that the particle oscillates in the transverse (x_1, x_2) plane and propagates forwards in the longitudinal (x_3) direction. This forward drift motion of the particle is worth considering in more detail. If we consider the 0- and 3-components of the particle trajectory, we find that they can be decomposed into a sum of their constant and oscillatory components

$$x^\mu(\tau) = \langle x^\mu \rangle + X^\mu(\tau), \quad (3.18)$$

where $X^\mu(\tau)$ is the oscillatory component and the constant component $\langle x^\mu \rangle$ is the Fourier zero mode

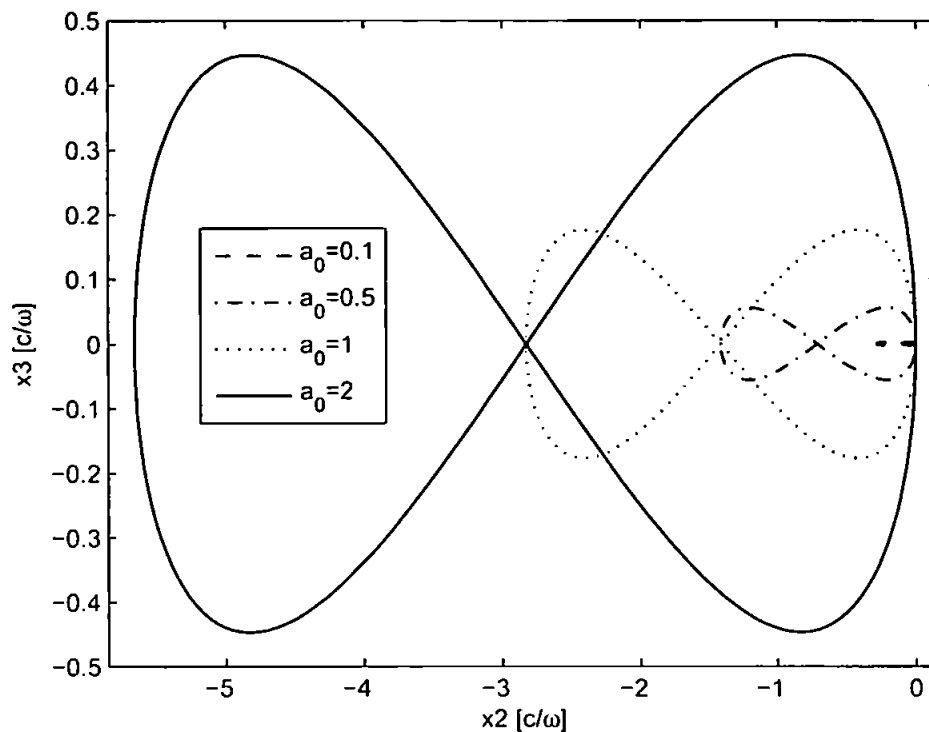
$$\langle x^\mu \rangle \equiv \frac{\omega}{2\pi} \int_0^{2\pi/\omega} d\tau' x^\mu(\tau'). \quad (3.19)$$

Using (3.19) we can calculate the longitudinal drift velocity

$$v_{\text{drift}} = \frac{\langle x^3 \rangle}{\langle x^0 \rangle} = \frac{u_0^3 + a_0^2 u^- (\delta^2 + \frac{1}{2})}{u_0^0 + a_0^2 u^- (\delta^2 + \frac{1}{2})}. \quad (3.20)$$

It is interesting to consider the effects of boosting to a frame where the drift velocity is zero, i.e. to the frame where the electron is at rest on average. The results of such a boost for the cases of linear and circular polarisation are shown in Figures 3.2 and 3.3, respectively. In the case of linear polarisation the electron exhibits a figure-of-eight motion, which increases in size proportionally to a_0 . (We note that these plots

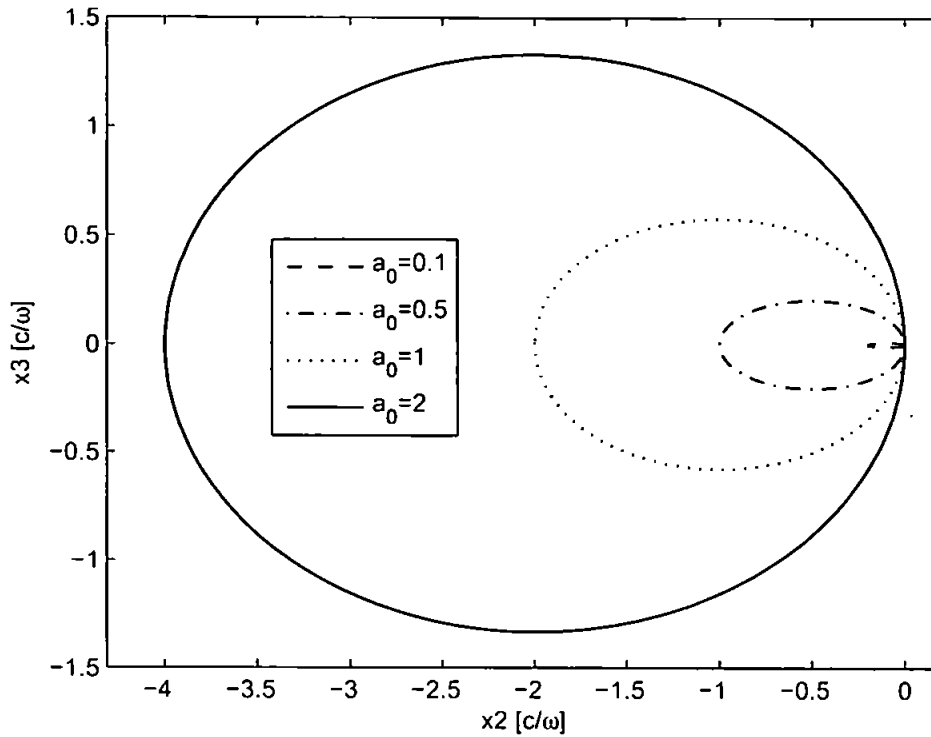
Figure 3.2: Electron motion in the average rest frame (linear polarisation) for various a_0 .



are consistent with those by Sarachik and Schappert in [47].) The electron motion follows a Lissajous curve of proportion 2:1. For circular polarisation we find that the electron follows an elliptical trajectory. Figure 3.4 shows the electron trajectory in the average rest frame for various degrees of elliptical polarisation. We can see clearly how the trajectory makes the transition from figure-of-eight to circular as we change the polarisation.

The transverse oscillations of the electron in the laser field lead to an interesting and somewhat surprising effect. Since in the average rest frame the electrons complete a whole orbit during a single laser cycle, it makes sense to consider only the average momentum of the electron over the cycle, since the laser photons cannot resolve the details of the oscillatory motion [27]. Working in the average rest frame we define a *quasi-momentum* q such that q^2 is equal to the square of the proper

Figure 3.3: Electron motion in the average rest frame (circular polarisation) for various a_0 .



time average of the momentum p

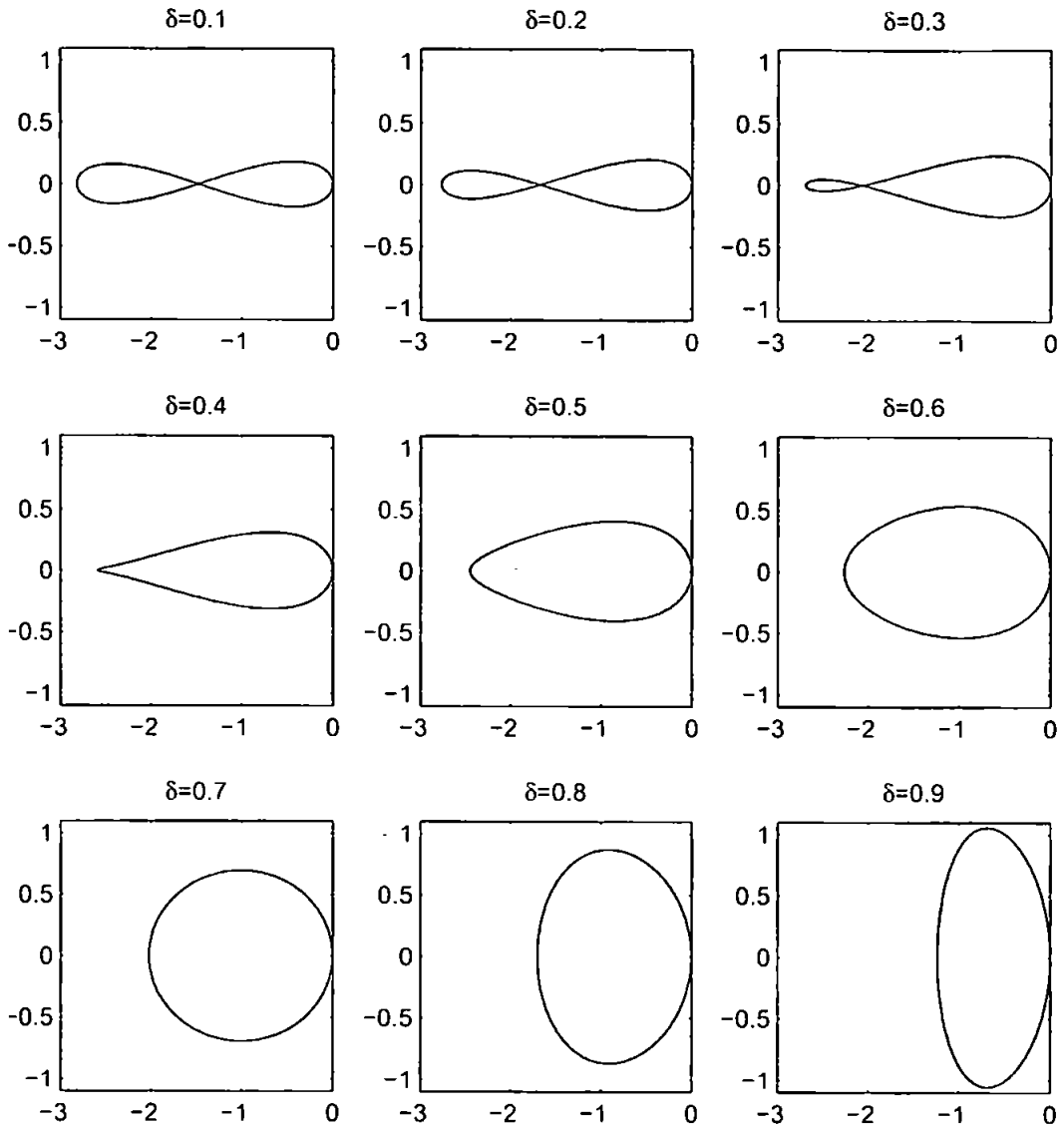
$$q^2 \equiv \left[\frac{\omega}{2\pi} \int_0^{2\pi/\omega} d\tau' p(\tau') \right]^2 = m^2(1 + a_0^2). \quad (3.21)$$

Hence, analogously to the on-shell condition $p^2 = m^2$, we are able to define an *effective mass* for the electron in the laser field

$$m_*^2 \equiv q^2 = m^2(1 + a_0^2). \quad (3.22)$$

In effect, to the laser photons the electron doesn't appear to oscillate; instead it appears to have an intensity dependent shifted mass m_* .

Figure 3.4: Electron motion in the average rest frame for varying degrees of polarisation, $a_0 = 1$. Horizontal axis x_2 , vertical axis x_3 .



3.3 Particle Radiation

As we did in Chapter 2 for crossed fields, we now bring our attention to the radiation emitted by an electron in a plane wave. The radiated energy can be found once again by evaluating the integral (2.41). This calculation involves the evaluation of several nested integrals, and would therefore normally necessitate a recourse to numerics. However, for the case of circular polarisation, the circular symmetry of the electron's

orbit makes an analytical evaluation of the expression possible. Performing the calculation, one finds that the energy radiated per unit solid angle $dP^0/d\Omega$ can be expressed as an infinite series of Bessel functions. These Bessel sums may be written in closed form, giving an analytical expression for $dP^0/d\Omega$. For an electron at rest in the lab frame, this may be written as

$$\frac{dP^0}{d\Omega} = \frac{e^2\omega^2 a_0^2}{64\pi} \left(\frac{1}{(1-\theta)^{\frac{7}{2}} \left(1 + \frac{1}{2}a_0^2 \sin^2\left(\frac{1}{2}\theta\right)\right)^4} \right) \times \left(\frac{\left(\cos\theta - \frac{1}{2}a_0^2 \sin^2\left(\frac{1}{2}\theta\right)\right)^2}{\left(1 + \frac{1}{2}a_0^2 \sin^2\left(\frac{1}{2}\theta\right)\right)} (4 + \Theta^2) + (1 - \Theta^2)(4 + 3\Theta^2) \right), \quad (3.23)$$

where

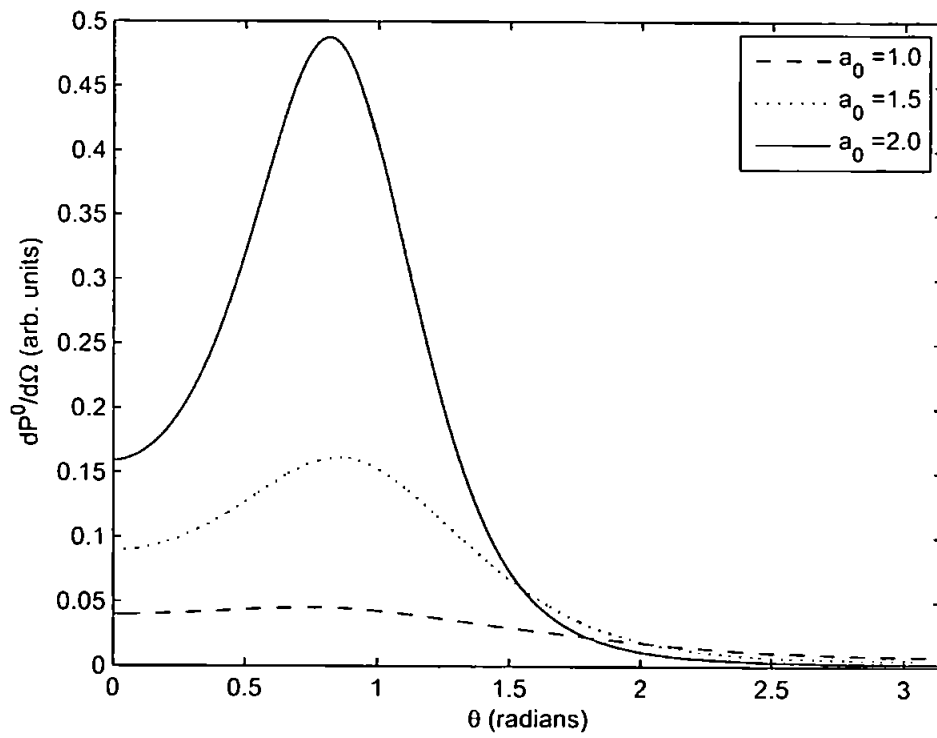
$$\Theta = \frac{a_0 \sin\theta}{\sqrt{2} \left(1 + \frac{1}{2}a_0^2 \sin^2\left(\frac{1}{2}\theta\right)\right)}. \quad (3.24)$$

For details of the calculation we refer the reader to Sarachik and Schappert [47] and Esarey *et al* [48]. We note that the solid angle measure $d\Omega$ is a function of the scattering angle θ only, since the circular symmetry of the electron motion in a circularly polarised plane wave means that the radiated energy has no azimuthal (ϕ) dependence.

We consider the angular distribution of the radiated energy for various laser intensities in Figure 3.5. This is of particular interest to us, since in Chapter 5 we will be considering the properties of the emitted radiation using a strong field QED approach. We can see from Figure 3.5 that the peak radiated energy moves towards the $\theta = 0$ (forward scattering) direction as the laser intensity increases. It is also clear that the signal strength increases with the laser intensity.

Before we go on to consider the the electron dynamics in an infinite plane wave from a QED perspective, in the next chapter we will introduce a numerical scheme to calculate the electron trajectory in an arbitrary classical background field.

Figure 3.5: Plot showing the angular distribution of the radiated energy for an electron in a circularly polarised plane wave. Calculations are for the lab frame, where the electron is assumed to be initially at rest ($\gamma = 1$).



Chapter 4

Electron Dynamics in Arbitrary Classical Fields

So far we have solved the Lorentz force equation (2.1) for the cases of constant fields and plane waves. In these cases the electron velocities and trajectories are obtainable analytically. However, if we are to progress to more complex/realistic field configurations, then we will be forced to resort to numerics.

4.1 Covariant Matrix Numerics

A standard approach to numerically solving the Lorentz force equation (2.1) would involve taking a discretisation of proper time into steps of length h . Under such a discretisation we would have

$$\frac{d}{d\tau}u^2 = 2u \cdot \dot{u} = \mathcal{O}(h^n) \neq 0; \quad n > 0, \quad (4.1)$$

for a numerical scheme of order n . The result of this would be that the on-shell condition $p^2 = mc^2$ (i.e. $u^2 = c^2$) would be violated. The introduction of such an unphysicality could lead to numerous undesirable effects including, for example, that the acceleration \dot{u} will no longer be spacelike. In fact, when the discretisation

error is considered in relation to p^2 , we find that

$$p^2 = m^2 u^2 \rightarrow m^2(u^2 + Kh^n), \quad (4.2)$$

for some constant K . Hence the introduction of a discretisation error can effectively be viewed as a mass/momentum shift of the electron. In the previous chapter we saw that, in a plane wave, an electron experiences a *laser*-induced mass shift. It follows that if we are to study such effects using a numerical scheme, it is undesirable for such a scheme to introduce its own *discretisation*-induced mass shift. With this in mind, we present a new type of numerical scheme which is manifestly covariant and *precisely* preserves the on-shell condition $u^2 = c^2$.

Our numerical scheme is based upon a $\text{SL}(2, \mathbb{C})$ representation of the four-velocity. This method was used by Itzykson and Zuber [75] to find the analytical solution to (2.1) for constant electric and magnetic fields, and is considered from a mathematical perspective in [76]. However, what we propose here is to use the method as a basis for a numerical scheme that can be used to solve the Lorentz force equation (2.1) for completely arbitrary field configurations. We begin by introducing the matrix basis $\sigma^\mu \equiv (\mathbf{1}, \boldsymbol{\sigma})$ where $\boldsymbol{\sigma}$ denotes the three Pauli matrices

$$\sigma^1 = \begin{pmatrix} 0 & 1 \\ 1 & 0 \end{pmatrix}, \quad \sigma^2 = \begin{pmatrix} 0 & -i \\ i & 0 \end{pmatrix}, \quad \sigma^3 = \begin{pmatrix} 1 & 0 \\ 0 & -1 \end{pmatrix}. \quad (4.3)$$

which satisfy

$$\sigma^a \sigma^b = \delta_{ab} + i\epsilon_{abc} \sigma^c, \quad (4.4)$$

where ϵ_{abc} is the Levi-Civita tensor in three-dimensions. Now we introduce the

matrix U which represents the particle four-velocity in this basis

$$U \equiv u^\mu \sigma_\mu \in \text{SL}(2, \mathbb{C}). \quad (4.5)$$

Using (4.4) we find the following commutator and anti-commutator relations

$$\frac{1}{2} [\sigma_k, U] = i \epsilon_{kam} u^a \sigma^m, \quad \frac{1}{2} \{\sigma_k, U\} = \sigma_k u^0 + u^k. \quad (4.6)$$

Using these we find we can re-write the equation of motion (2.1) as

$$\dot{U} = \frac{e}{m} (\mathbb{E}^\dagger U + U \mathbb{E}), \quad (4.7)$$

where

$$\mathbb{E}^\dagger \equiv (\mathbf{E} + i\mathbf{B}) \cdot \boldsymbol{\sigma}. \quad (4.8)$$

Introducing the time-ordering operator

$$\mathcal{L}(\tau) \equiv \mathcal{T} \left\{ \int_0^\tau d\tau' \mathbb{E}^\dagger(\tau') \right\}, \quad (4.9)$$

we may write the implicit general solution to (4.7) as

$$U(\tau) = \mathcal{L}(\tau) U(0) \mathcal{L}^\dagger(\tau). \quad (4.10)$$

In order to turn this into a numerical method, we must discretise (4.10). To do this we introduce a discrete set of $n + 1$ equally spaced proper times τ_k ($k = 0, \dots, n$)

$$\tau_0 = 0, \quad \tau_k = k, \quad \tau_n = \tau, \quad \mathbb{E}_k \equiv \mathbb{E}(x(\tau_k)). \quad (4.11)$$

Making use of the Baker-Campbell-Hausdorff formula [65], we then find approximately (up to order $\mathcal{O}(d\tau^2)$)

$$\mathcal{L} = \exp \left\{ \mathbb{E}_n^\dagger d\tau \right\} \times \dots \times \exp \left\{ \mathbb{E}_1^\dagger d\tau \right\} =: \mathbb{L}_n. \quad (4.12)$$

where ' \times ' denotes matrix multiplication. Thus our numerical solution becomes

$$U_n = \mathbb{L}_n U(0) \mathbb{L}_n^\dagger, \quad (4.13)$$

such that

$$U(\tau) = U_n(\tau) + \mathcal{O}(d\tau). \quad (4.14)$$

In order to utilise this method we must solve (4.13) iteratively. We begin with an initial guess for $u(\tau_i)$ based upon our value for $u(\tau_{i-1})$. Then we use the trapezium rule to calculate an initial guess for the particle position $x(\tau_i)$. Once we have the position we can insert it into the expression for the electric fields to find the value of $\mathbb{E}^\dagger(\tau_i)$, which we subsequently use to find an improved four-velocity $u(\tau_i)$ via (4.13). This procedure is iterated until the particle positions $x(\tau_i)$ and velocities $u(\tau_i)$ do not change within given error margins.

Now a crucial point is that, in our $SL(2, \mathbb{C})$ representation, the on-shell condition $u^2 = c^2$ reads

$$\det U(\tau) = c^2 = 1. \quad (4.15)$$

Due to the fact that $\text{tr} \sigma_k = 0$, we have

$$\det \exp \left\{ \mathbb{E}_i^\dagger d\tau \right\} = \exp \left\{ \text{tr} \mathbb{E}_i^\dagger d\tau \right\} = 1, \quad (4.16)$$

and so

$$\det \mathbb{L}_i = \det \mathbb{L}_i^\dagger = 1. \quad (4.17)$$

Hence

$$\det U_n(\tau) = \det U(0) = c^2, \quad (4.18)$$

meaning that the on-shell condition is *exactly* preserved by the discretisation.

4.2 Numerical Examples

We test our code using a light-cone time ($n \cdot x$) dependent linearly polarised plane wave field, encapsulated in a Gaussian pulse. In the notation of Chapter 3 we have

$$F_1 = P(n \cdot x) \sin(k \cdot x), \quad (4.19)$$

$$F_2 = 0, \quad (4.20)$$

where $P(n \cdot x) = P(\tau)$ is the pulse function which we define to be

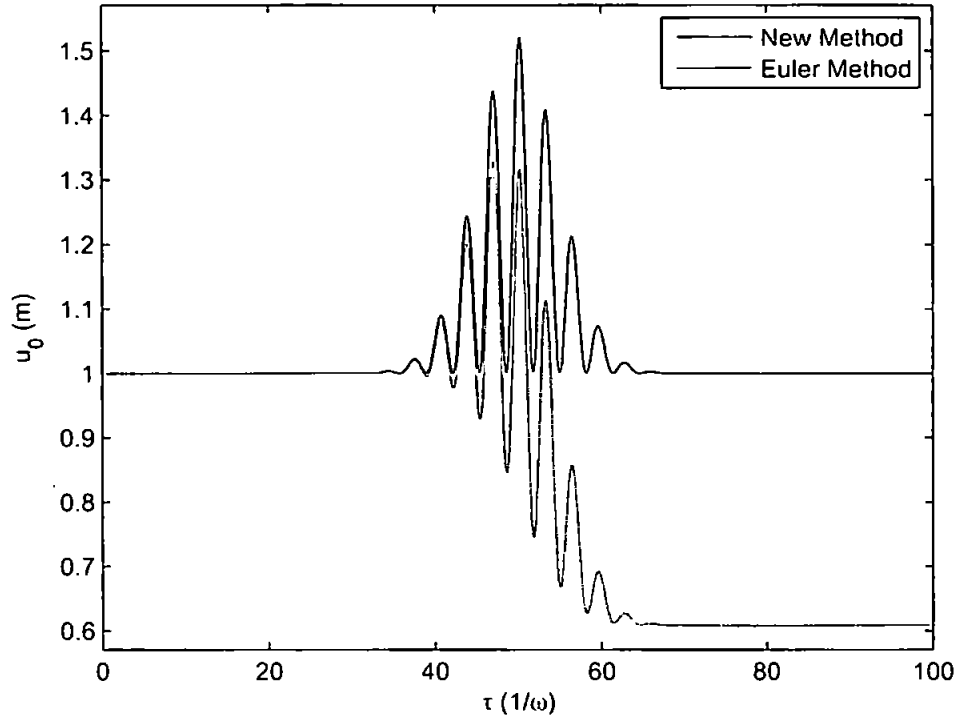
$$P(\tau) = A \exp\left(-\frac{(\tau - \tau_0)^2}{\eta^2}\right), \quad (4.21)$$

where we have once again traded light-cone time $n \cdot x$ for proper time¹ τ using (3.7). The constant τ_0 specifies the centre of the pulse and η is a measure for the number of laser wavelengths within the width of the pulse. Neglecting the radiative back-reaction effects and proceeding along the same lines as in Chapter 3, we can solve the equation of motion (2.1) analytically down to the final integrals, which must

¹Note that we expressed P in terms of τ here in the text to improve the clarity of notation. In our actual numerical experiments our codes will calculate in terms of the light-cone time $n \cdot x$.

be evaluated numerically. This will give us a benchmark against which to test our code.

Figure 4.1: The results of calculating u_0 numerically using our method and using the Euler method, $u_0 = 1$, $\eta = 10$, $d\tau = 0.125$.



In order to quantify the accuracy of the new method, we introduce two measures of numerical error. The first is the Euclidean norm ϵ_{cuc} defined

$$\epsilon_{\text{cuc}} = \sqrt{\frac{1}{\Delta\tau} \int_{\tau_0 - \Delta\tau}^{\tau_0 + \Delta\tau} d\tau P^2(\tau) \sum_{\mu=0}^3 [u^\mu(\tau) - u_{\text{ani}}^\mu(\tau)]^2}. \quad (4.22)$$

with $u_{\text{ani}}(\tau)$ being the analytical solution. Since we are now dealing with a pulsed field, it is important to choose the region $\Delta\tau$, over which we consider the errors, with care. This is because the numerical errors are very small when the field strengths are very low, and so the error can be made arbitrarily small by increasing the width

$\Delta\tau$ of interest. Therefore we define our parameters as follows:

$$\tau_0 = \frac{1}{N} \int_{-\infty}^{\infty} d\tau' \tau' P^2(\tau'), \quad N = \int_{-\infty}^{\infty} d\tau' P^2(\tau'), \quad (4.23)$$

$$\Delta\tau = 2\sqrt{\tau_2 - \tau_0^2}, \quad \tau_2 = \frac{1}{N} \int_{-\infty}^{\infty} d\tau' (\tau')^2 P^2(\tau'). \quad (4.24)$$

Thus it can be seen that we are considering the Euclidean norm over a region that covers one standard deviation each side of the centre of the pulse τ_0 . Our other measure of numerical error will be the maximum norm ϵ_{\max}

$$\epsilon_{\max} = \max_{\mu, \tau} [|u^\mu(\tau) - u_{\text{nl}}^\mu(\tau)|], \quad (4.25)$$

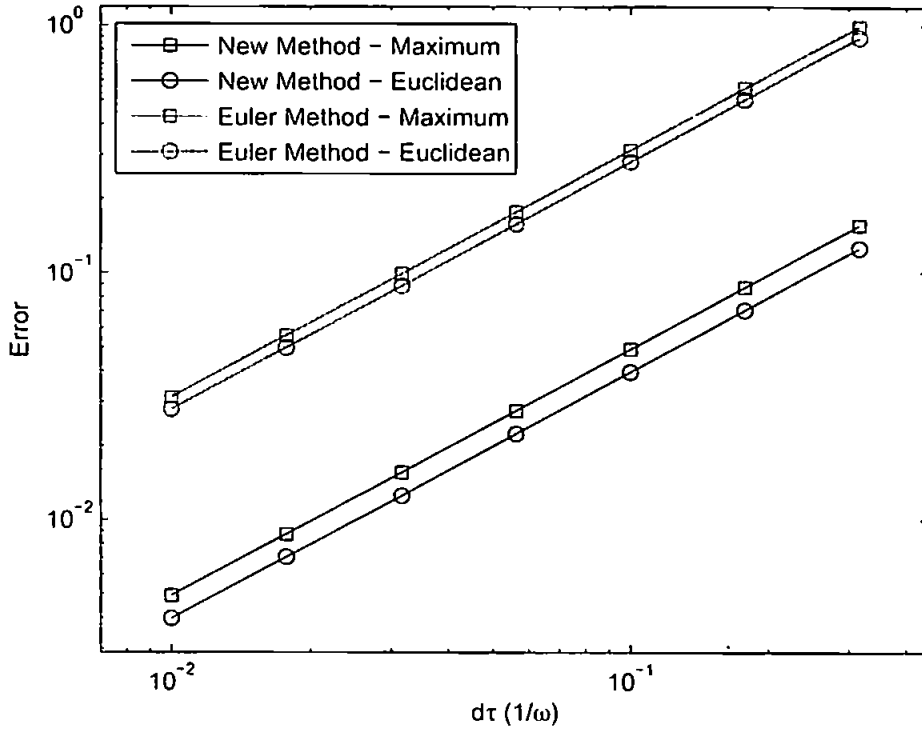
We also consider it useful to compare our method directly with a conventional numerical scheme; in this case we will choose to compare with the Euler method [77]. While a higher order method would be more accurate, we have chosen the Euler method because, like our method, it is first order and so we will be comparing like with like.

For a pulsed plane wave field our definition of a_0 (1.12) needs qualifying, since E_{rms} averaged over all proper time will be zero. The most convenient solution is for us to adopt the definition

$$a_0 = \frac{eE_{\text{max}}}{\omega m}. \quad (4.26)$$

Figure 4.1 shows u_0 for an electron subjected to the field (4.19) for $a_0 = 1$, $\eta = 10$, calculated using our new method and using the Euler method. The discretisation size is $d\tau = 0.125 \approx 0.02\omega$ periods, which we can see is too coarse for the Euler method to perform effectively, while the difference between our method and the analytical solution is less than the thickness of the plotting lines. In Figure 4.2 we consider the errors as a function of the discretisation size. As we would expect for

Figure 4.2: Numerical errors for both methods as a function of the proper time discretisation size $d\tau$.



first order methods, both schemes produce errors that increase linearly with $d\tau$. We find for our method

$$\epsilon_{\text{euc}} \approx 0.39d\tau, \quad \epsilon_{\text{max}} \approx 0.49d\tau, \quad (4.27)$$

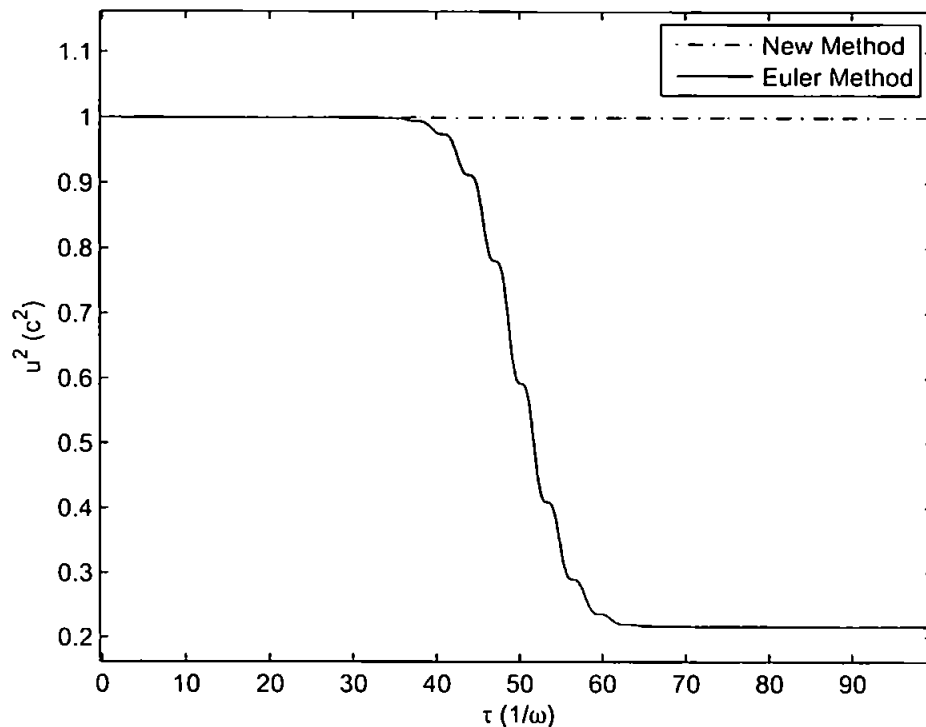
and for the Euler method

$$\epsilon_{\text{euc}} \approx 2.8d\tau, \quad \epsilon_{\text{max}} \approx 3.1d\tau. \quad (4.28)$$

Finally, in Figure 4.3 we demonstrate the fact that our new method preserves the on-shell condition $u^2 = c^2$, whereas the Euler method (a conventional scheme) does not.

In summary, we have developed a novel numerical scheme for solving the Lorentz

Figure 4.3: Plot demonstrating that our numerical scheme preserves the on-shell condition $u^2 = c^2$, whereas the Euler method does not.



force equation (2.1) for an electron in an arbitrary background field. Unlike conventional discretisation schemes, our method is fully covariant, precisely preserving the on-shell condition. The method we have presented is a first order scheme, and so we have compared it directly with a conventional first order method – the Euler method. We found our method to be well-behaved, more accurate than the Euler method, and we confirmed numerically that the on-shell condition is indeed preserved. Although we have not considered the effect of the radiation back-reaction on the electron motion, the scheme we have presented here could be adapted to incorporate this. More information on this is given in Appendix B. It is hoped that the covariant method presented here will be of use to researchers studying the effects of the beam profile on the electron dynamics.

Chapter 5

Nonlinear Compton Scattering of an Electron in a Plane Wave

5.1 Introduction

Having outlined the behaviour of an electron in a classical plane wave, we now move on to study such behaviour from a quantum perspective. We thus consider the nonlinear Compton scattering that occurs when an electron collides with a high intensity plane wave laser field. Since this study is motivated primarily by the advent of high intensity laser facilities, we will pay particular attention to intensity dependent effects in the scattering processes. Such scattering processes have been considered previously, most notably by Brown and Kibble [49], Goldman [51] and Nikishov and Ritus [52, 53, 20, 26]. In this chapter we will re-visit this work in light of the recent increases in laser intensities, outlined in Chapter 1. We will consider nonlinear Compton scattering involving a very high intensity laser ($a_0 > 1$) and electrons of moderate to high energy (i.e. $\gamma \sim 1 \dots 100$). The phenomenology of the scattering processes with such parameter values has now become experimentally relevant.

5.2 Volkov Electrons and the S-Matrix

Specifically, we consider the nonlinear Compton scattering that is the sum of the sub-processes

$$e^- + n\gamma_L \rightarrow e^- + \gamma, \quad n \in \mathbb{N} \quad (5.1)$$

where an electron absorbs n laser photons γ_L and then emits a single photon γ . For a plane wave, the energy density $T^{00} = (E^2 + B^2)/2 = E^2$. The laser photons have energy $\hbar\omega$, so in a volume V containing n_γ photons we have

$$E^2 = \frac{n_\gamma \hbar\omega}{V} \equiv N_\gamma \hbar\omega. \quad (5.2)$$

Since the laser intensity a_0 is proportional to E^2 (see (1.12)), it must therefore be proportional to the photon density N_γ . The precise relationship can be written

$$a_0^2 = 4\pi\alpha\nu^2\lambda^3 N_\gamma, \quad (5.3)$$

where α is the fine structure constant and we have introduced the rescaled (dimensionless) measure of frequency

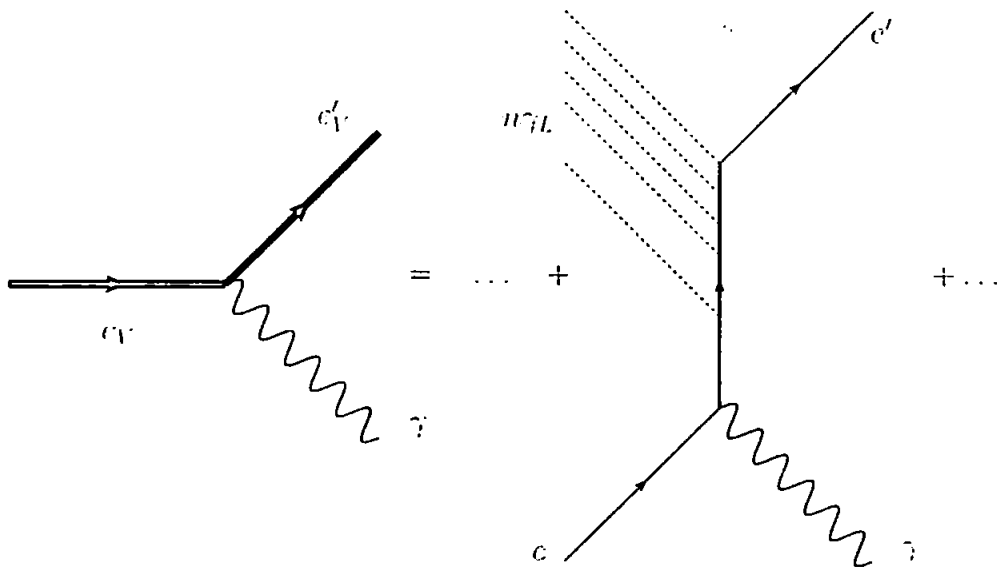
$$\nu \equiv \frac{\omega}{m}. \quad (5.4)$$

As the authors state in [20], the probability for a given n th order scattering process (5.1) is proportional to $a_0^{2n} \sim N_\gamma^n$. Hence for $n > 1$ the probability becomes *non-linear* in the photon density and thus the process is known as *nonlinear* Compton scattering.

From (5.3) we see that for $a_0 \sim 1$ there are of order $\lambda^3 N_\gamma \sim 10^{12}$ photons in a laser wavelength cubed. With such a high photon density it seems reasonable to

neglect the effects of beam depletion in the scattering process. Therefore we shall adopt the formalism used by Nikishov and Ritus [52] and Brown and Kibble [49], where the electrons interact with a quantum photon field \hat{A}_μ plus a classical background field $\mathcal{A}_\mu(x)$. In effect, the electron lines in the Feynman diagrams become ‘dressed’ by the background field \mathcal{A}_μ . Diagrammatically, they are represented by heavy lines as shown in the left-hand side of Figure 5.1. Such diagrams can be expanded into an infinite sum of conventional QED diagrams (i.e. those involving free electron propagators), each one representing the scattering process involving n laser photons. We note that the analogous S-matrix element, corresponding to the Feynman diagram on the left hand side of Figure 5.1 but with ‘naked electrons’, would vanish due to momentum conservation.

Figure 5.1: Feynman diagram for the nonlinear Compton scattering of an electron in a background field. The thick lines represent electrons dressed by the background field. The diagram can be expanded into an infinite series of conventional QED Compton scattering diagrams, each involving the absorption of n laser photons.



Once again we take our background field to be a plane wave dependent on the light-cone time $k \cdot x$, $\mathcal{A}_\mu \equiv \mathcal{A}_\mu(k \cdot x)$. We are fortunate that the Dirac equation can be solved exactly for such a field (the ‘Volkov solution’ [54]), giving us the electron

wave function

$$\Psi_p(x) = e^{iS} \left(1 + \frac{e}{k \cdot p} \not{k} A\right) u_p \equiv e^{iS} \Gamma_p u_p, \quad (5.5)$$

where we have adopted the Feynman slash notation, $\not{a} \equiv \gamma^\mu a_\mu$, and S is the Hamilton-Jacobi classical action

$$S = -p \cdot x - \frac{1}{2k \cdot p} \int_0^{k \cdot x} d\phi [2eA \cdot p - e^2 A^2] \equiv -p \cdot x - I_p. \quad (5.6)$$

At this point we will define our background field to be

$$A^\mu = a_1^\mu \cos(k \cdot x) + a_2^\mu \sin(k \cdot x), \quad (5.7)$$

where the four-amplitudes a_j are equal in magnitude and orthogonal $a_j \cdot a_k = -a^2 \delta_{jk}$ and satisfy the Landau gauge condition $a_j \cdot k = 0$. Thus we are specifically considering the case of circular polarisation, since this is the only case where the photon emission rate calculations are expressible in terms of standard functions. In terms of our plane wave definition given in Section 3.2, this corresponds to setting $\delta = 2^{-1/2}$ and multiplying the amplitudes A by a factor ω .

Applying the kinetic momentum operator $\hat{p} - eA = i\partial - eA$ to the Volkov solution (5.5), and (suggestively) denoting the time-average of the result by q , we find

$$q = p + \frac{a_0^2 m^2}{2(k \cdot p)} k \equiv p + q_L. \quad (5.8)$$

Thus the electron acquires an additional *intensity-dependent* longitudinal momentum q_L , caused by the presence of the laser field. The zero component of the quasi-momentum q^0 was first found by Volkov [54], while the generalisation to the four-vector q^μ is due to Sengupta [56]. Squaring q , we find that the intensity dependent

momentum shift leads to an intensity dependent mass shift

$$q^2 = m^2(1 + a_0^2) \equiv m_*^2. \quad (5.9)$$

This is precisely the same momentum/mass shift that we found in our classical analysis in Section 3.2.

As we are going to be studying the photon emission rates, we need to know the S-matrix elements for the scattering process. These were originally calculated by Nikishov and Ritus [52] and are presented by Landau and Lifshitz in [57]. Here we will briefly run through the calculation, but adopting the more physically transparent formalism used by Heinzl *et al* [59] in their study of pair-production.

The S-matrix relating the final electron state f to the initial state i is

$$S_{fi} = -ie \int d^4x \bar{\Psi}_{p'} \not{\epsilon} e^{-ik' \cdot x} \not{A} \Psi_p, \quad (5.10)$$

where ϵ is the polarisation four-vector. We find

$$S_{fi} = ie \int d^4x e^{i(p-p'-k') \cdot x} \mathcal{M}(k \cdot x), \quad (5.11)$$

where $\mathcal{M} = e^{i(I_p - I_{p'})} \bar{u}_{p'} \not{\Gamma}_{p'} \not{A} \Gamma_p u_p$. Since Ψ_p is an eigenfunction of \mathbf{p} , we obtain after integrating out the spatial coordinates

$$S_{fi} = -ie(2\pi)^3 \delta^{(3)}(\mathbf{p} - \mathbf{p}' - \mathbf{k}') \int dx^- e^{i(p^- - p'^- - k'^-) \cdot x} \mathcal{M}(x^-). \quad (5.12)$$

Now, for a plane wave, I_p can be decomposed into a constant average (Fourier zero mode) plus an oscillatory component. The average over a wavelength is precisely the longitudinal component of the quasi-momentum (5.8), so we find we can write

the action (5.6) as

$$S_p = -p \cdot x - (q_- - p_-)x^- + \delta I_p, \quad (5.13)$$

where $(q_- - p_-)x^-$ comes from the Fourier zero mode and δI_p the oscillatory component. Introducing the boost invariant, light-cone quasi-momentum fractions

$$\frac{q_-}{k_-} - \frac{q'_-}{k'_-} - \frac{k'_-}{k_-} \equiv Q - Q' - K', \quad (5.14)$$

and changing variables from x^- to $k \cdot x = \omega x^-$, we can write

$$S_{fi} = -ie(2\pi)^3 \frac{1}{k_-} \delta^{(3)}(\mathbf{p} - \mathbf{p}' - \mathbf{k}') \int d(k \cdot x) e^{i(Q - Q' - K')k \cdot x} M(k \cdot x), \quad (5.15)$$

where $M = \mathcal{M}$ but with $I \rightarrow \delta I$. Now M is a purely oscillatory, periodic function and so we can expand it into the Fourier series

$$M(k \cdot x) = \sum_n \widetilde{M}_n e^{in k \cdot x}. \quad (5.16)$$

Thus we find

$$S_{fi} = -ie(2\pi)^3 \frac{1}{k_-} \delta^{(3)}(\mathbf{p} - \mathbf{p}' - \mathbf{k}') \sum_n \widetilde{M}_n \delta(Q - Q' - K' + n), \quad (5.17)$$

and so the S-matrix can be expressed as a ' δ -comb'. Hence we see that the quantity $Q - Q' - K' + n$ is conserved, which is equivalent to writing $q_- + nk_- = q'_- + k'_-$. Now, we can see from (5.8) and Section 3.2 that the quasi-momentum q differs from the momentum p only in the light-cone component, therefore it follows that the full quasi-momentum is conserved in the scattering process,

$$q + nk = q' + k'. \quad (5.18)$$

5.3 Kinematics

We now study the kinematics resulting from the quasi momentum conservation (5.18). We begin by introducing the Mandelstam invariants s, t, u , [57, 58]

$$s_n = (q + nk)^2 = m_*^2 + 2nk \cdot p, \quad (5.19)$$

$$t_n = (nk - k')^2 = -2nk \cdot k', \quad (5.20)$$

$$u_n = (nk - q')^2 = m_*^2 - 2nk \cdot p', \quad (5.21)$$

where we have used the fact that, since k is lightlike,

$$q \cdot k = p \cdot k, \quad q' \cdot k = p' \cdot k. \quad (5.22)$$

Note that the three Mandelstam variables are not independent of each other since $s_n + t_n + u_n = 2m_*^2$. Also since they are n -dependent, they will be different for each scattering process. From (5.19) and (5.20) it is immediately clear that the invariants are subject to the conditions

$$s_n \geq s_{n-1}, \quad (n > 1) \quad (5.23)$$

$$t_n \leq 0. \quad (5.24)$$

We also find

$$s_n u_n = m_*^4 - 4n^2 (k \cdot p)^2 \leq m_*^4, \quad (5.25)$$

which means that one of the boundaries of the physical region in the Mandelstam plane is a hyperbola. If we fix a line $s = s_n$ then, for the n th order scattering process.

the physically allowed ranges for t and u are

$$\begin{aligned} t_{\min} &= 2m_*^2 - s_n - m_*^4/s_n & u_{\max} &= m_*^4/s_n & \text{back scattering} \\ t_{\max} &= 0 & u_{\min} &= 2m_*^2 - s_n & \text{forward scattering} \end{aligned} \quad (5.26)$$

To see how the Mandelstam parameters relate to the scattered photon frequencies, we return to the quasi-momentum equation (5.8). Squaring both sides and substituting in (5.22), we can eliminate q'

$$nk \cdot p = k' \cdot p + \left(n + a_0^2 \frac{m^2}{2k \cdot p}\right) k \cdot k', \quad (5.27)$$

since $k^2 = k'^2 = 0$. In order to simplify our discussion, we will from here on assume that the photons and electrons collide head-on. This means that there is now only one angle to consider – the scattering angle of the photon θ . Therefore,

$$k = \omega(1, \mathbf{n}), \quad p = (E_p, -|\mathbf{p}|\mathbf{n}), \quad (5.28)$$

and

$$\mathbf{n} \cdot \mathbf{p} = -|\mathbf{p}|, \quad \mathbf{n}' \cdot \mathbf{p}' = -|\mathbf{p}'| \cos \theta. \quad (5.29)$$

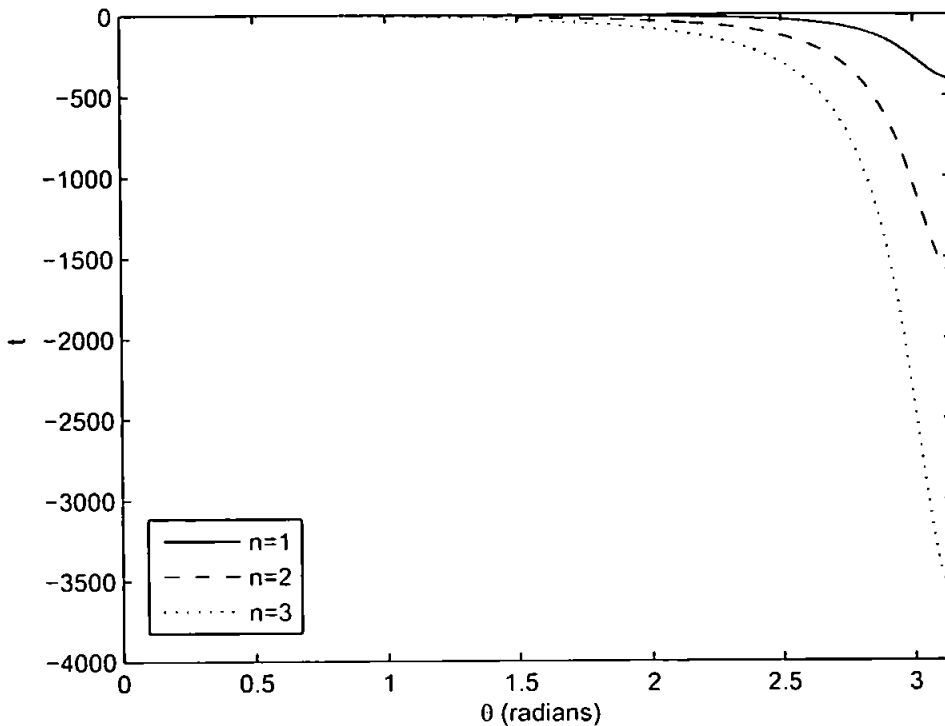
Considering just the momentum (zero) components, we can rearrange (5.27) to give an expression for the frequency of the scattered photon,

$$\nu'_n = \frac{n\nu}{1 + j_n(1 - \cos \theta)}, \quad (5.30)$$

where

$$j_n = \frac{n\nu - \gamma\beta + a_0^2\gamma(1 - \beta)/2}{\gamma(1 + \beta)}. \quad (5.31)$$

Figure 5.2: The dependence of t on θ (FZD values). We see that t attains its minimum for forward scattering ($\theta = \pi$).

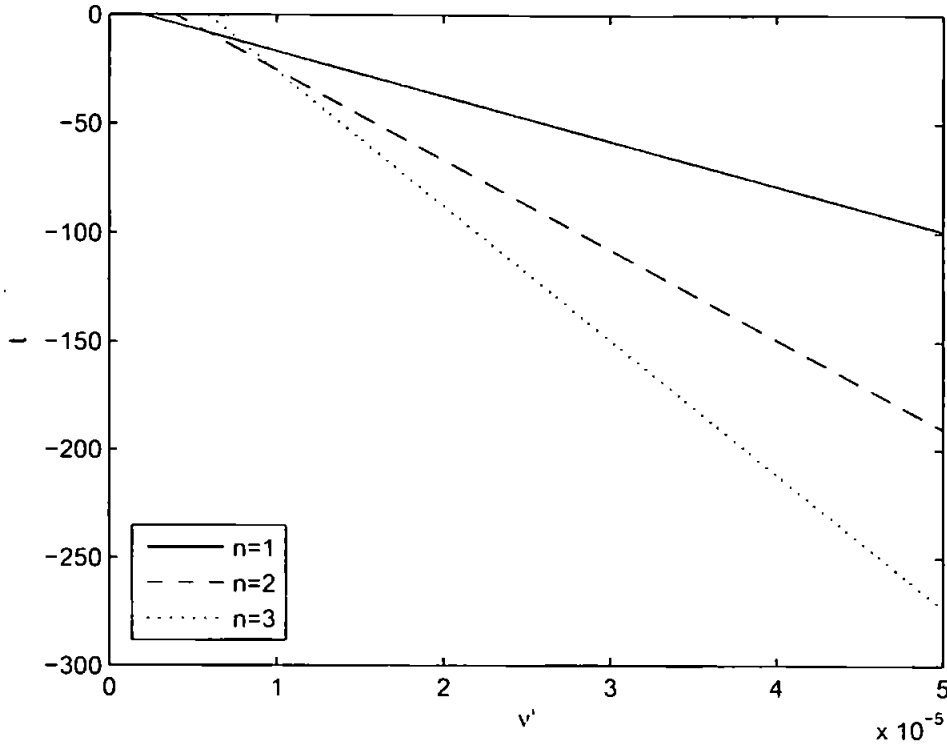


It can be seen that when $j_n < 0$ the maximum emission frequency occurs when the photons are backscattered ($\theta = \pi$). Conversely, when $j_n > 0$ the maximum frequency occurs for forward scattering ($\theta = 0$). We note that the frequency ranges of the scattered photons are dependent on the number of laser photons absorbed, n . The spectrum resulting from the scattering process where $n = 1$ will be referred to as the 'fundamental harmonic'. Where $n > 1$ laser photons are involved, these spectra will be referred to as 'higher harmonics'.

It should be noted that the linear Compton case, well known from physics text books, occurs in the limit $a_0 \rightarrow 0$, $n = 1$ (i.e. in the low intensity limit). Thus the possibility of the electron absorbing $n > 1$ laser photons and subsequently generating a higher harmonic, is exclusive to the nonlinear regime.¹

¹The emission of higher ($n = 2, 3$) harmonics has been observed experimentally by colliding an electron with a *linearly* polarised laser beam. In such a beam the electron (classically speaking) exhibits a figure-of-eight motion, which causes the scattered photon frequency spectrum to have an

Figure 5.3: The dependence of t on ν' (FZD values).



From (5.30) we can see that $\nu'_n(0) = n\nu$. Thus, in the case $j_n < 0$ the emitted photon frequency is blue shifted relative to laser photons, and in the case $j_n > 0$ it is red shifted,

$$j_n < 0 \implies n\nu < \nu'_n(\theta) < \nu'_n(\pi) \quad \text{blue shift} \quad (5.32)$$

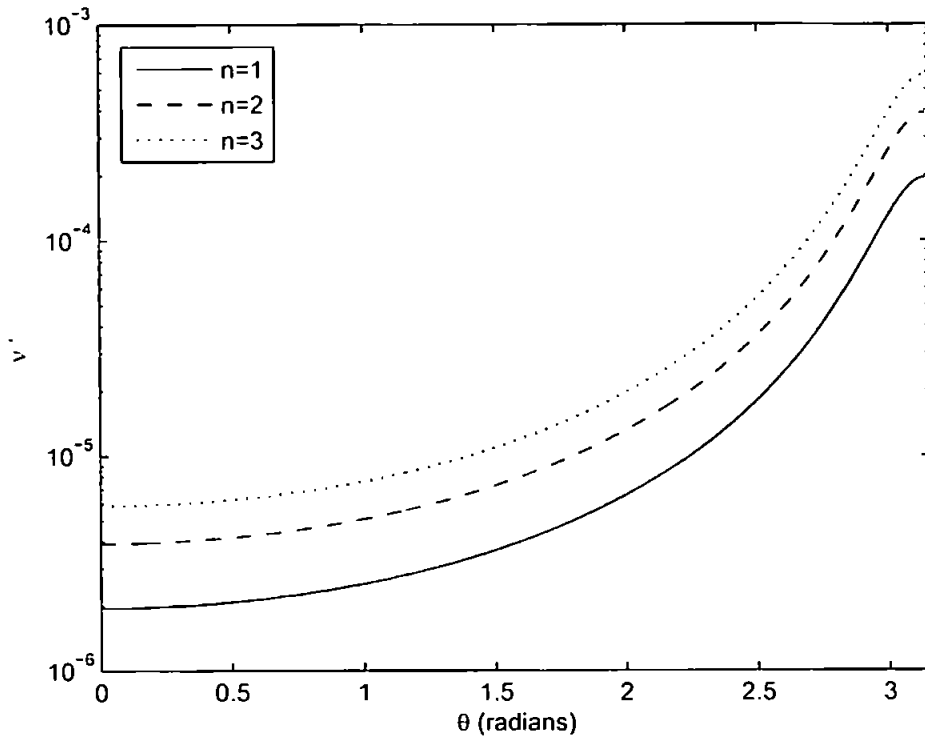
$$j_n > 0 \implies \nu'_n(\pi) < \nu'_n(\theta) < n\nu \quad \text{red shift.} \quad (5.33)$$

Sometimes, in the literature, the case of a red shift is referred to as 'Compton scattering' and that of a blue shift as 'inverse Compton scattering'. Since these are frame dependent statements, we choose not to make the distinction in this discussion.

The frequency range given by (5.32), (5.33) corresponds to the t interval in the

additional dependence on the azimuthal angle, ϕ . The second and third harmonics were then able to be identified by observing the resulting quadrupole and sextupole radiation patterns, respectively [61, 60] (see also [19]). Such an observation is not possible using a circularly polarised laser, due to the azimuthal symmetry of the scattered photon distribution (resulting from the circular motion of the electrons in such a field).

Figure 5.4: Plot showing the relationship between θ and ν' . $\gamma = 100$, $\omega = 1$, $m = 0.511$ MeV, $a_0 = 20$.



Mandelstam representation (5.26). Evaluating the Mandelstam invariants explicitly in terms of ν' and θ , we have

$$s_n = m_*^2 + 2nm^2\nu\gamma(1 + \beta) \quad (5.34)$$

$$t_n = -2nm^2\nu\nu'(1 - \cos\theta) \quad (5.35)$$

$$u_n = m_*^2 - 2nm^2\nu(\gamma(1 + \beta) - \nu'(1 - \cos\theta)). \quad (5.36)$$

Figures 5.2 and 5.3 show the relationship between t_n and θ and ν' respectively. As discussed, we see that t_n achieves its minimum when $\nu' = \nu'_{\max}$ or $\theta = \pi$. Figure 5.3 shows that there is a linear relationship between t_n and ν' , unlike between t_n and θ , where there is a rapid decrease in the value of t_n as $\theta \rightarrow \pi$.

We return now to consider the relationship between the scattered photon frequency ν' and the scattering angle θ . Figure 5.4 shows a plot of ν' as a function of θ

for typical parameter values. It is evident that emitted frequency is maximal when $\theta = \pi$ (backscattering). Provided $j_n \neq 0$, it is possible to use (5.30) to trade ν' for θ in our expressions (and vice versa). (When $j_n = 0$ the scattered frequency ν'_n loses its θ -dependence, collapsing to the line $n\nu$.)

For parameter values similar to those at the FZD (i.e. $a_0 \sim 20$, $\gamma \sim 100$) we find $j_n > 0$, and so the maximum frequency of the emitted photons is given by

$$\nu'_{\max(\text{FZD})} = \frac{(1 + \beta)^2 \gamma^2 n \nu}{1 + a_0^2 + 2\nu n(1 + \beta)\gamma}. \quad (5.37)$$

For large γ this gives us

$$\nu'_{\max(\text{FZD})} \approx \frac{4\gamma^2 n \nu}{1 + a_0^2}. \quad (5.38)$$

At this point it is useful to define an effective γ , much in the same spirit as our effective mass,

$$\gamma_*^2 \equiv \frac{E_p^2}{m_*^2} = \frac{\gamma^2}{1 + a_0^2}, \quad (5.39)$$

thus (5.38) becomes²

$$\nu'_{\max(\text{FZD})} \approx 4\gamma_*^2 n \nu. \quad (5.42)$$

For a given n we can plot the fixed line $s = s_n$ on the Mandelstam diagram. For $n = 1, 2, 3, 4$, these lines are shown in Figure 5.5. From our above consideration

²It is interesting to compare this to the case of linear Compton scattering, where we have

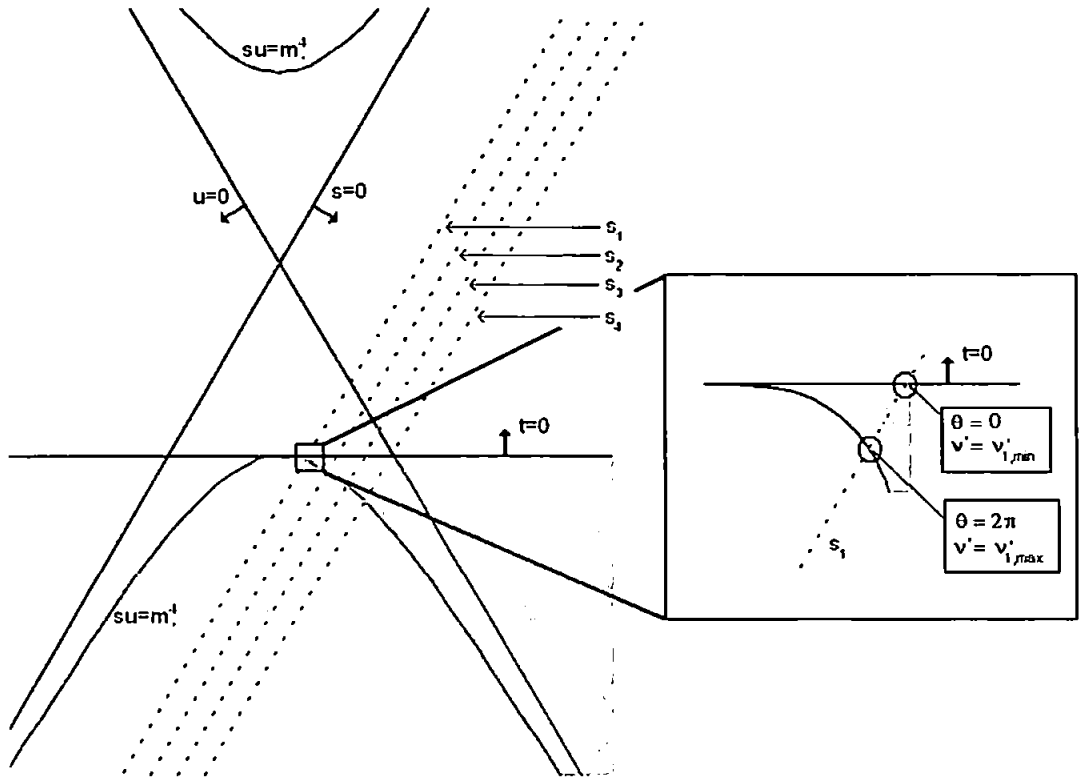
$$\nu'_{\max} = \frac{4\gamma^2 \nu}{1 + 4\gamma\nu}. \quad (5.40)$$

which for large γ becomes

$$\nu'_{\max} \approx 4\gamma^2 \nu. \quad (5.41)$$

of t , we can see that, as we move downwards along the sections of these lines that are in the physical region, we are moving along the ranges $\nu' = \nu'_{\min} \dots \nu'_{\max}$ and $\theta = 0 \dots 2\pi$. The point where the lines $s = s_n$ meet the hyperbola $su = m_e^2$ is the point where $\nu' = \nu'_{\max}$ and $\theta = \pi$.

Figure 5.5: Mandelstam plot for nonlinear Compton scattering (5.1) using FZD values. The shaded area shows the physical region of the Mandelstam plane.



5.4 Photon Emission Rates

We now return to our S-matrix calculation (5.17). The S-matrix may be translated into an emission rate, which we would expect to be comprised of Bessel functions, since it consists of an exponential of Volkov phases. Indeed, we find that the differential rate for the emission of a single photon of frequency ν' by the n th harmonic

process (5.1) is

$$\frac{dW_n}{dx} = \frac{1}{(1+x)^2} \mathcal{J}_n(a_0, \nu, \nu'_n, z), \quad (5.43)$$

which was previously obtained by Nikishov and Ritus [20]. The function \mathcal{J}_n is defined

$$\mathcal{J}_n(a_0, \nu, \nu'_n, z) = -\frac{4}{a_0^2} J_n^2(z) + \left(2 + \frac{x^2}{1+x}\right) [J_{n-1}^2(z) + J_{n+1}^2(z) - 2J_n^2(z)], \quad (5.44)$$

where J_n are the Bessel functions of the first kind. We have introduced the three new kinematic (and Lorentz) invariants x , y and z

$$x \equiv \frac{k \cdot k'}{k \cdot p'}, \quad y_n \equiv \frac{2nk \cdot p}{m_*^2}, \quad z \equiv \frac{2a_0}{y_1} \sqrt{\frac{x(y_n - x)}{1 + a_0^2}}. \quad (5.45)$$

Physically, y_n represents the maximum recoil of the electron during the scattering process. The relationship of x and y to the Mandelstam invariants is

$$x = \frac{t}{u - m_*^2} \quad (5.46)$$

$$y_n = \frac{s_n}{m_*^2} - 1. \quad (5.47)$$

From our analysis of the physically allowed ranges of the Mandelstam invariants in Section 5.3, we find that the kinematically allowed range of x for the n th harmonic is

$$0 \leq x \leq y_n. \quad (5.48)$$

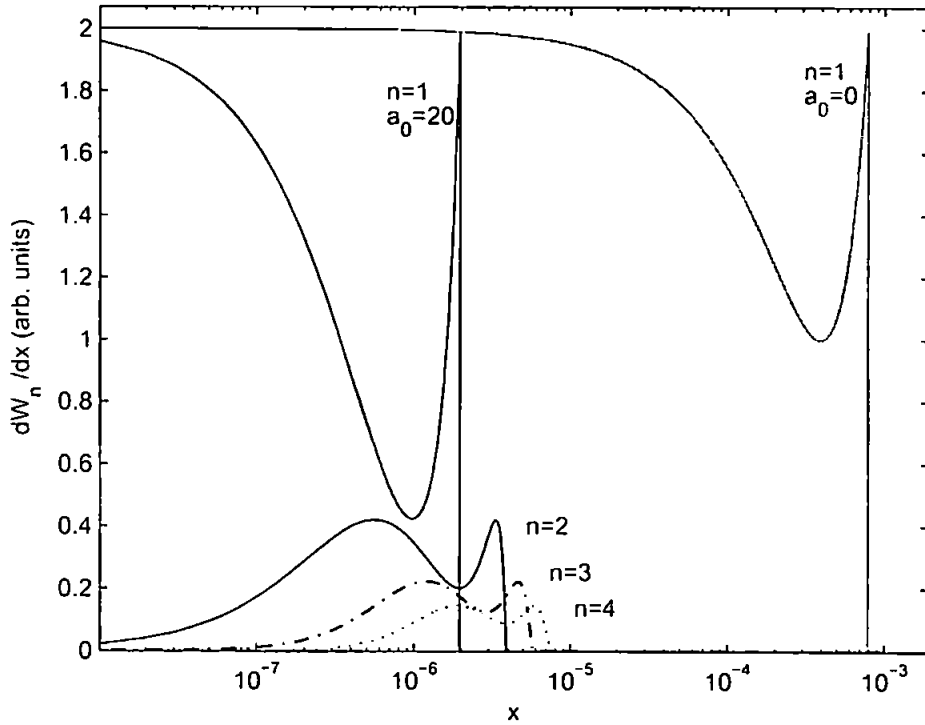
Outside of this range the rate for the n th harmonic vanishes. (We see that for x outside of this range the Bessel parameter z becomes complex.) To obtain the total

emission rate we simply sum over all the harmonics,

$$\frac{dW}{dx} = \sum_{n=1}^{\infty} \frac{dW_n}{dx}. \quad (5.49)$$

In Figure 5.6 we show the first few partial emission rates as a function of x . It

Figure 5.6: Partial emission rates for nonlinear Compton scattering as a function of x (FZD values). The emission rate for linear Compton scattering is shown for comparison.



can be seen that the higher harmonics have a reduced signal strength compared to the fundamental harmonic, and that each subsequent higher harmonic is reduced compared to the previous one. Also included in the plot is the emission rate corresponding to linear Compton scattering. A striking observation is that the edge $x = y_1$ of the (nonlinear) fundamental harmonic, which we will from here on refer to as the 'Compton edge', has been shifted to the left by several orders of magnitude compared to the linear case. The size of this shift may be calculated analytically as

follows. Evaluating y_n explicitly we find

$$y_n = \frac{2\gamma(1 + \beta)n\nu}{1 + a_0^2} = ny_1. \quad (5.50)$$

Thus we may express y_n as a function of a_0 , allowing us to write

$$y_n = y_n(a_0) = ny_1(a_0) = \frac{n}{1 + a_0^2}y_1(0). \quad (5.51)$$

We can therefore see that the fundamental harmonic will be shifted by a factor of $1/(1 + a_0^2)$ to the left compared to the linear case. This is a highly significant result since it offers an experimentally detectable signal of the mass shift (5.9).

Figure 5.7 shows the total emission rate summed to 30, 60 and 100 harmonics. We can see that convergence only becomes an issue at the far extremity of the plot ($x \gtrsim 10^{-5}$). An interesting observation is that the peak at the Compton edge (from here on known as the ‘Compton peak’) gets bolstered by the higher harmonics, increasing the signal strength compared to the linear peak.

Frequency Parameterisation

Using (5.30) to eliminate θ from our expressions, it is possible to express the emission rate (5.43) in terms of the scattered photon frequency ν'

$$\frac{dW_n}{d\nu'} = \frac{dW_n}{dx} \frac{dx}{d\nu'} = -\frac{1}{\gamma(1 + \beta)j_n} \mathcal{J}_n(a_0, \nu, \nu'_n, z). \quad (5.52)$$

The frequency range of each individual harmonic is determined by (5.32) and (5.33).

In Figure 5.8 we have plotted the first few individual harmonics for FZD parameter values. As with the x parameterisation, we see that each harmonic has a reduced signal strength compared to the previous one, the difference being most noticeable between the fundamental and second harmonic.

Figure 5.7: Sum of partial emission rates as a function of x (FZD values). Dashed, lower curve: $n = 1 \dots 20$; dotted, middle curve: $n = 1 \dots 60$; solid, top curve: $n = 1 \dots 100$. The emission rate for linear Compton scattering is shown for comparison (in grey).

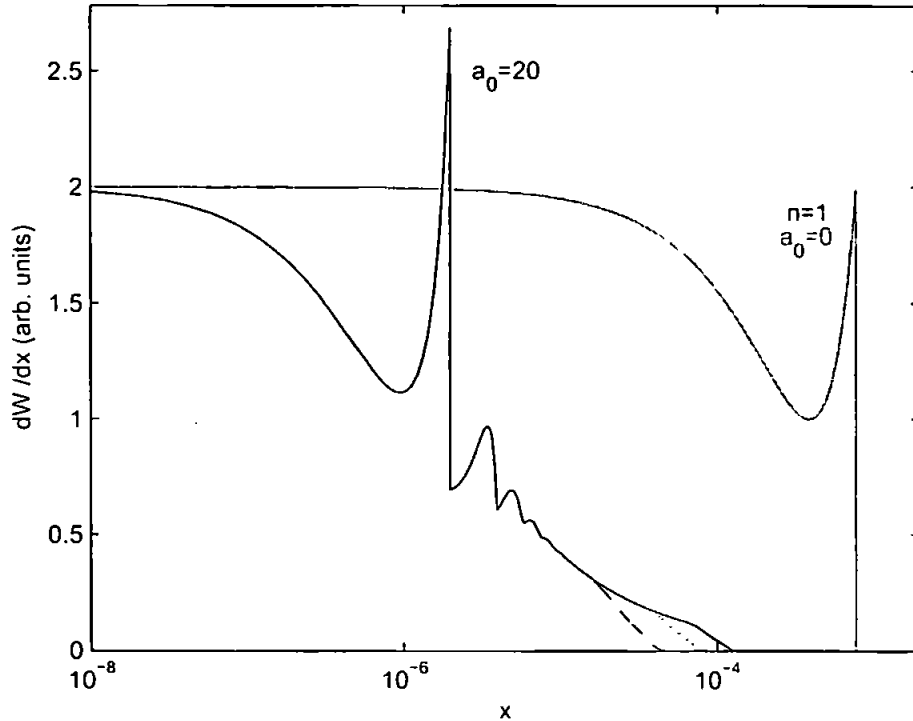
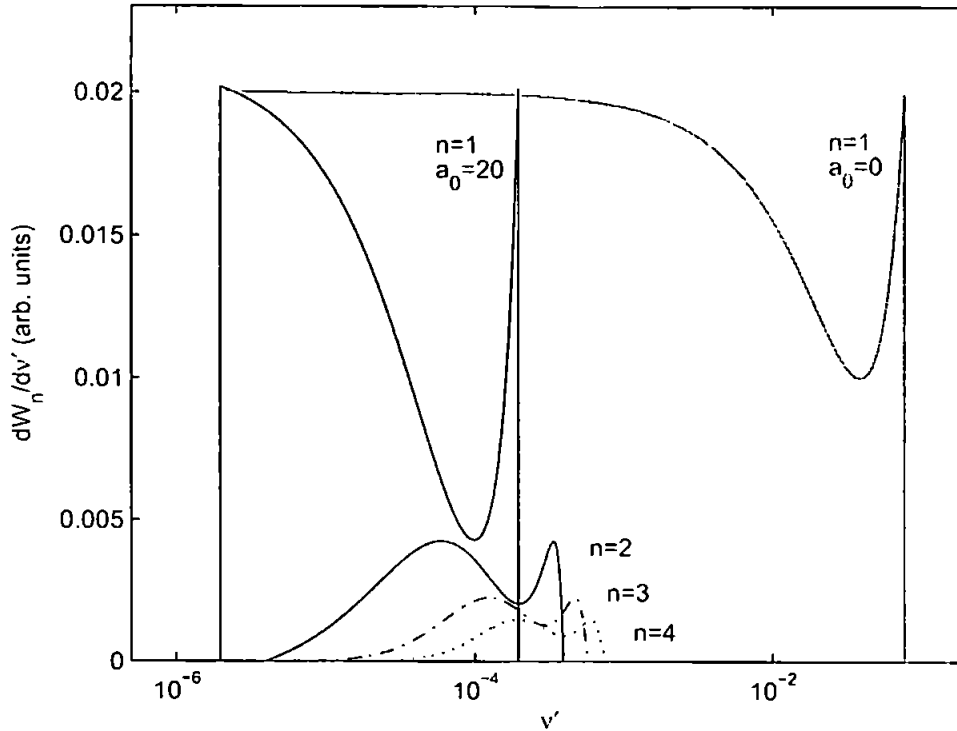


Figure 5.9 shows the total spectrum for the same parameter values. It is clearly evident that, analogously to the phenomenology of the x parameterisation, the Compton edge experiences a frequency red shift compared to the linear Compton case. We emphasise that the total frequency range is blue shifted, relative to the incoming photon frequency ν , due to the presence of the higher harmonics. This can be seen from (5.32) and (5.33). Once again it can be seen that the higher harmonics bolster the (fundamental harmonic's) Compton peak, increasing its signal strength as compared to linear Compton scattering.

In an experimental context the red shift of the spectra is important for two reasons. Firstly, the observation of the frequency shift will provide experimental evidence of the electron mass shift. Secondly, the measurement of the red shift

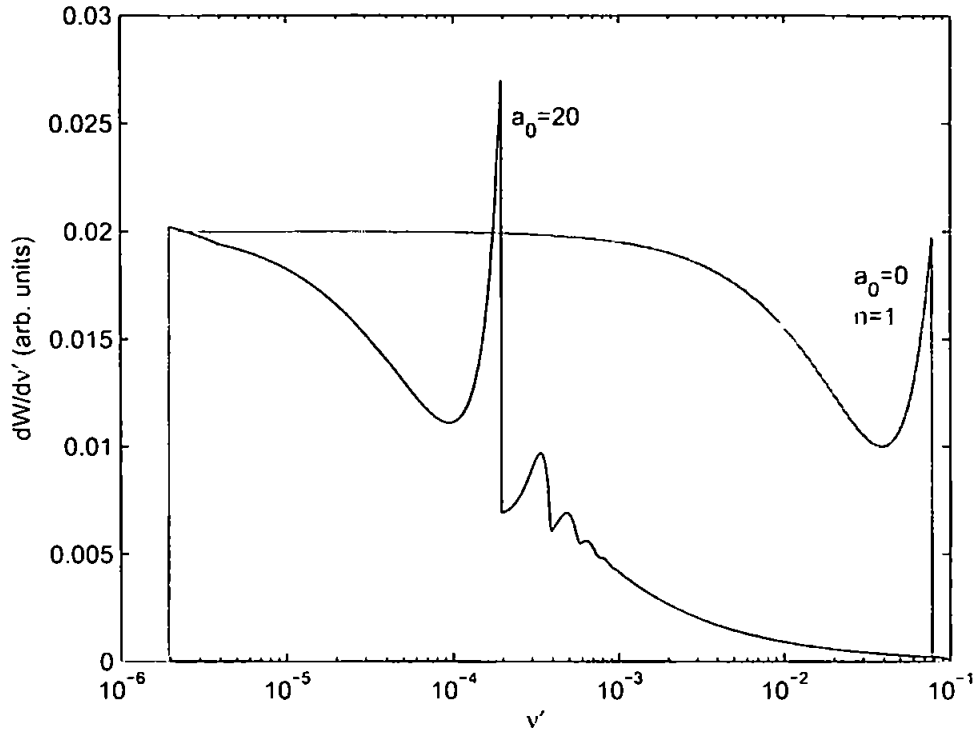
Figure 5.8: Individual harmonic spectra for nonlinear Compton scattering (FZD values). The spectrum for linear Compton scattering is included for comparison.



could be used to determine the laser intensity a_0 by (5.30) and (5.31). Looking once again at the emission spectra in Figure 5.9, we see that it should, in principle, be possible to observe the peaks corresponding to $n = 1, 2, 3$ and even 4. This assumes of course that the presence of various background effects, not included in our theoretical analysis, will not be too detrimental to the signal quality.

Previously we have discussed the dependency of the scattered photon frequency ν' on the sign of j_n . We now consider this in more detail in the context of the emission spectra. Recall from (5.32) and (5.33) that, for $j_n < 0$ (> 0), the emitted photon frequency (for a given scattering process) is blue (red) shifted relative to the laser photons. This implies that, by tuning the 'free' parameters γ and a_0 , it should, at least in principle, be possible to change from a blue shift to a red shift. In particular, at the point where j_n changes sign the n th harmonic will collapse to the single line $\nu'_n = n\nu$. Setting (5.31) equal to zero we find that, in order for the

Figure 5.9: Emission spectrum for nonlinear Compton scattering (FZD values). Spectrum for linear Compton scattering is included for comparison.



nth harmonic to collapse, the critical value of a_0 must be

$$a_{0,\text{crit}}^2 \equiv \frac{2(\gamma\beta - n\nu)}{\gamma(1 - \beta)}. \quad (5.53)$$

For large γ we find

$$a_{0,\text{crit}} = 2\gamma - n\nu - \frac{3 + n^2 + \nu^2}{4\gamma} + \mathcal{O}\left(\frac{1}{\gamma^2}\right). \quad (5.54)$$

Thus we may approximate

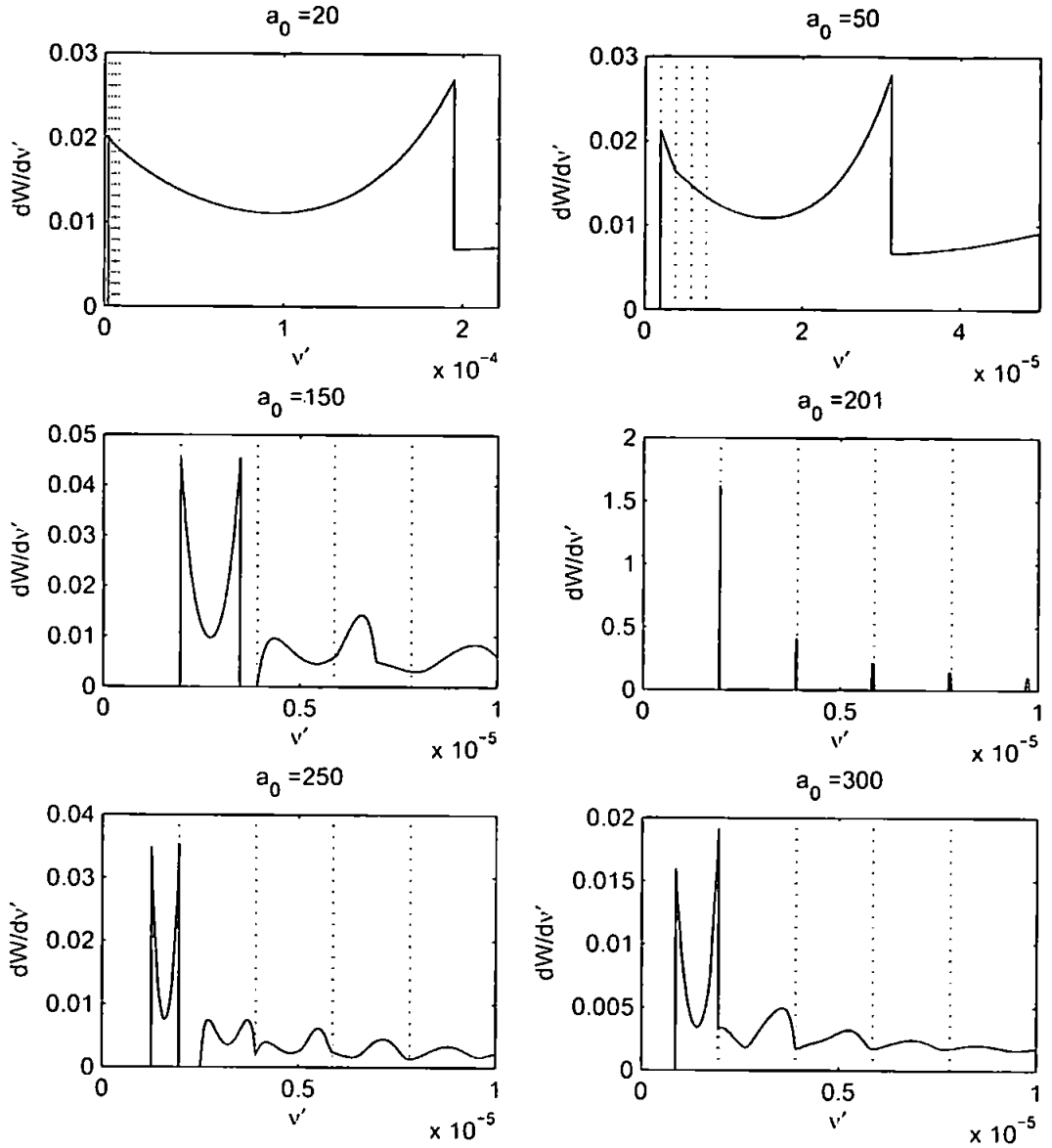
$$a_{0,\text{crit}} \approx 2\gamma. \quad (5.55)$$

for large γ and *all* small n (i.e. $n^2 \ll 4\gamma$). In the case of linear Compton scattering, the point where there is no frequency shift in the scattering process ($\nu' = \nu$) is the

point where the total momentum $\mathbf{P} = \mathbf{k} + \mathbf{p}$ equals zero. This is, of course, the centre-of-mass frame for the collision. Making the analogy to nonlinear Compton scattering, we see that the point where the n th harmonic collapses is the point where the total momentum $\mathbf{P} = n\mathbf{k} + \mathbf{q} = n\mathbf{k} + \mathbf{p} + \mathbf{q}_L$ equals zero. Therefore we can consider the point where $j_n = 0$ to define a ‘centre-of-mass’ frame for the n th scattering process.

Evaluating (5.53) for the FZD values we find that the fundamental harmonic will collapse for $a_0 \approx 200$. In Figure 5.10 we show a sequence of plots of the total spectra with a_0 going from 20 to 300. Looking at the plots we observe the following. In the subcritical regime ($a_0 < a_{0,\text{crit}}$, first three plots) the harmonic ranges are blue shifted relative to the frequencies $n\nu$ (shown as dotted vertical lines). This is more clearly seen in Figure 5.11 where we have plotted the individual harmonics. As a_0 is increased the harmonic ranges shrink (i.e. the right-hand edges are increasingly less blue shifted) and gaps begin to appear between the individual harmonics. At the critical a_0 the fundamental harmonic does indeed collapse to the line $\nu' = \nu$, disappearing from the plot. The $n = 2, 3, 4, \dots$ harmonics are very narrow for this value of a_0 since, assuming that γ is large enough for (5.54) to hold, the expansion of $a_{0,\text{crit}}$ is only n dependent in the second term and above. As a_0 increases further (into the supercritical regime), the fundamental and first few higher harmonics are red shifted relative to the lines $n\nu$ (again best seen from Figure 5.11). The harmonic ranges begin to increase again and the gaps begin to close. Hence, as we have discussed, there is an analogy between tuning the laser parameter a_0 and changing the Lorentz frame in which the processes are considered, as the quasi-momentum (and hence \mathbf{P}) change continuously as a function of a_0 . This is shown diagrammatically in Figure 5.12.

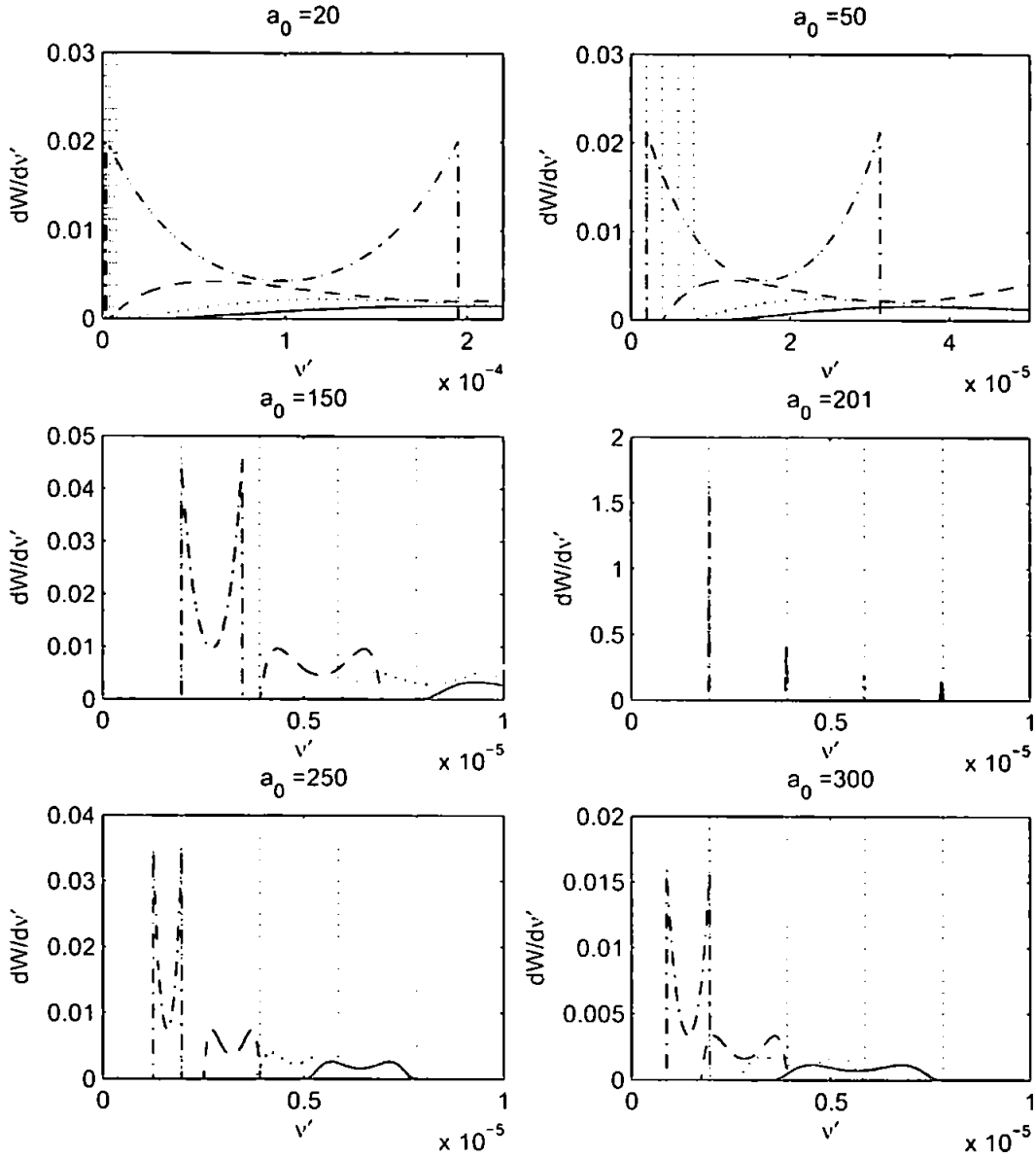
Figure 5.10: Sequence of emission spectra for nonlinear Compton scattering showing the transition from the subcritical ($a_0 < a_{0,\text{crit}}$) to the supercritical ($a_0 > a_{0,\text{crit}}$) regime. $\gamma = 100$, $a_{0,\text{crit}} \approx 200$. The vertical (dotted) lines correspond to the frequencies $n\nu$.



Angular Parameterisation

Alternatively we can consider the emission rates as a function of the scattering angle θ . Using (5.30) to now eliminate ν' from our expressions, we calculate the angular

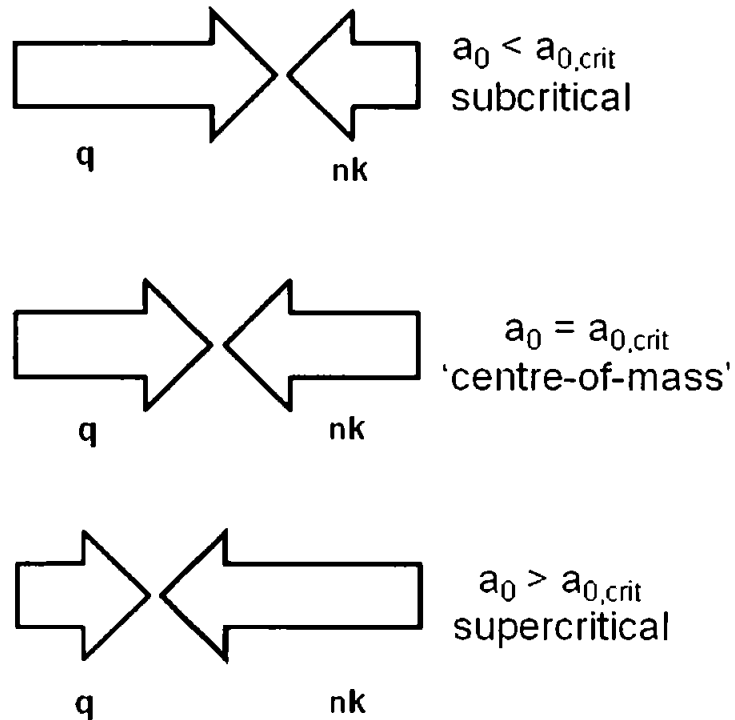
Figure 5.11: Sequence of individual emission harmonics for nonlinear Compton scattering showing the transition from the subcritical ($a_0 < a_{0,\text{crit}}$) to the supercritical ($a_0 > a_{0,\text{crit}}$) regime. $\gamma = 100$. $a_{0,\text{crit}} \approx 200$. The vertical (dotted) lines correspond to the frequencies $n\nu$. The grey lines show the total (summed) spectra. The harmonics are coded: dashdot: $n = 1$, dashed: $n = 2$, dotted: $n = 3$, solid: $n = 4$.



emission rate to be

$$\frac{dW_n}{d\Omega} = \frac{dW_n}{dr} \frac{dr}{d\Omega} = \frac{n\nu}{\gamma(1+\beta)[1+j_n(1-\cos\theta)]^2} \mathcal{J}_n(a_0, \nu, \nu'_n, z). \quad (5.56)$$

Figure 5.12: Diagrams showing how the centre-of-mass frame becomes intensity dependent.

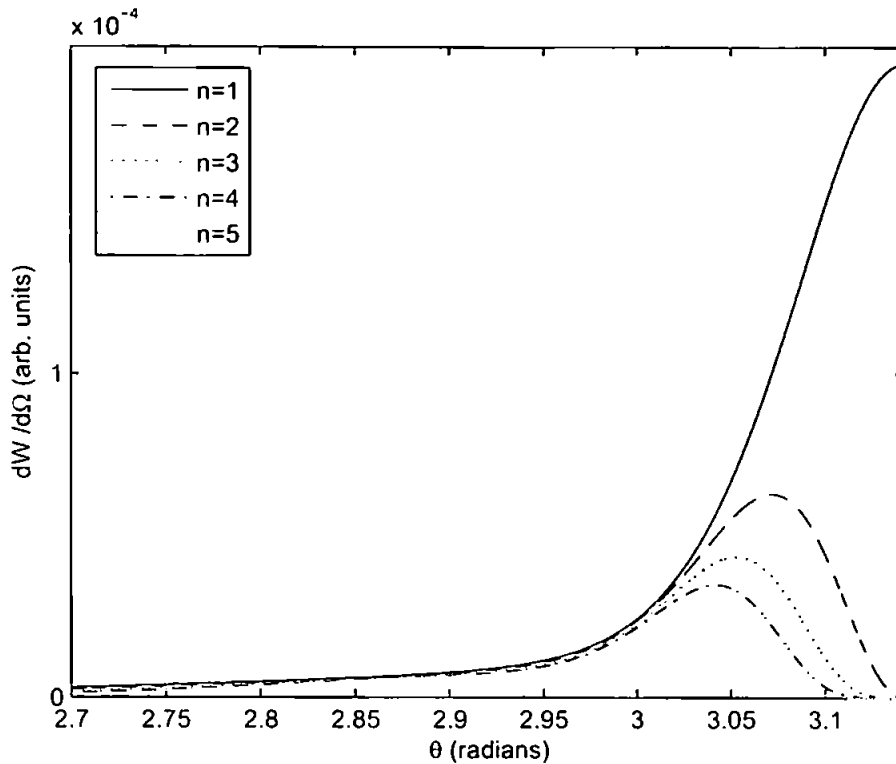


Here we have used the angular measure $d\Omega = \sin\theta d\theta$, which is the solid angle measure up to a factor of 2π since the circularly polarised laser field is not dependent on the azimuthal angle ϕ .

In Figures 5.13 and 5.14 we show the first few individual angular harmonics for the FZD values. We see that for these parameter values, the main emission intensity for each harmonic is concentrated in the region close to $\theta = \pi$ (back scattering direction). However, it is only the fundamental harmonic that is non zero actually at the point $\theta = \pi$. The higher harmonics fall to zero at this point, exhibiting what are known as 'dead cones'. Thus true back scattering occurs only for the scattering process where $n = 1$.

Figure 5.15 contains a sequence of plots of the individual harmonics for various a_0 (again, FZD values). We see that as a_0 is increased, the bulk of the signal for

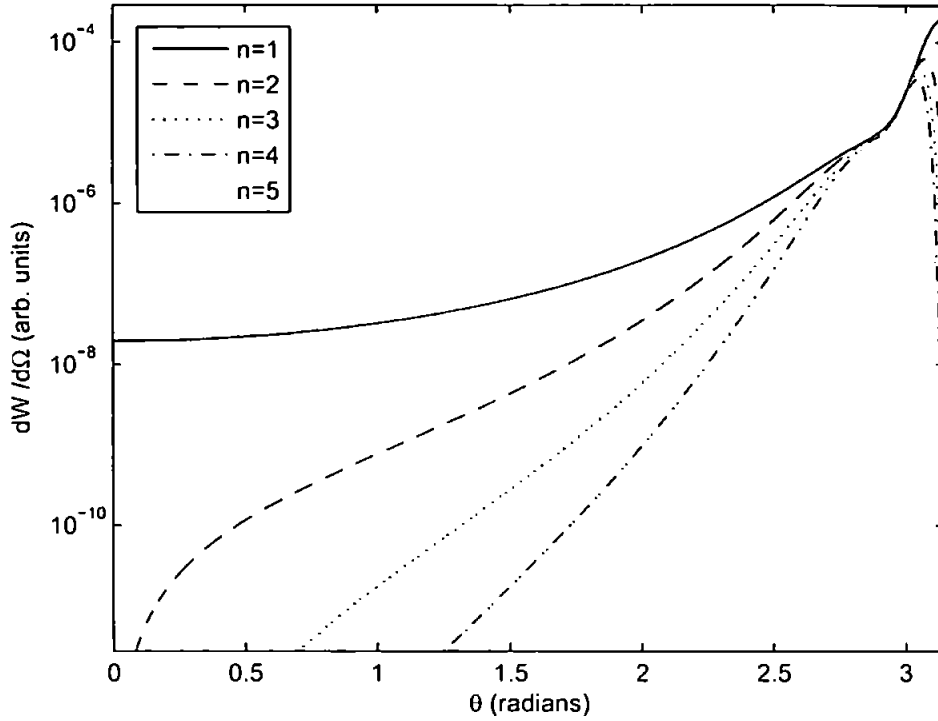
Figure 5.13: First 5 angular harmonics for nonlinear Compton scattering (FZD values). Only the fundamental harmonic contributes at $\theta = \pi$.



each harmonic begins to shift away from $\theta = \pi$. As a_0 reaches 200 the harmonics become symmetrical about $\theta = \pi/2$, with the fundamental harmonic contributing in both the forward ($\theta = 0$) and back scattering ($\theta = \pi$) directions. As a_0 is increased further, the harmonics shift further to the forward direction. Just as it did in the back scattering direction for low a_0 , the fundamental harmonic now contributes in the forward direction while the higher harmonics, though moving increasingly close to $\theta = 0$, still exhibit dead cones at this actual point.

Before we can sum the harmonics to calculate the total emission rate, we are forced to confront the issue of convergence. (We note that this was not an issue with the ν' parameterisation since, due to (5.32) and (5.33), a given frequency interval only contains a finite number of harmonics. With the θ parameterisation *all* the harmonics are constrained to the finite range $\theta = 0 \dots \pi$.) To begin, we note that the kinematic invariants x and z both have an n dependence, which we will now

Figure 5.14: Log plot of the first 5 angular harmonics for nonlinear Compton scattering (FZD values).



write explicitly as $x_n \equiv x$ and $z_n \equiv z$. Evaluating these invariants we find that they scale with n like

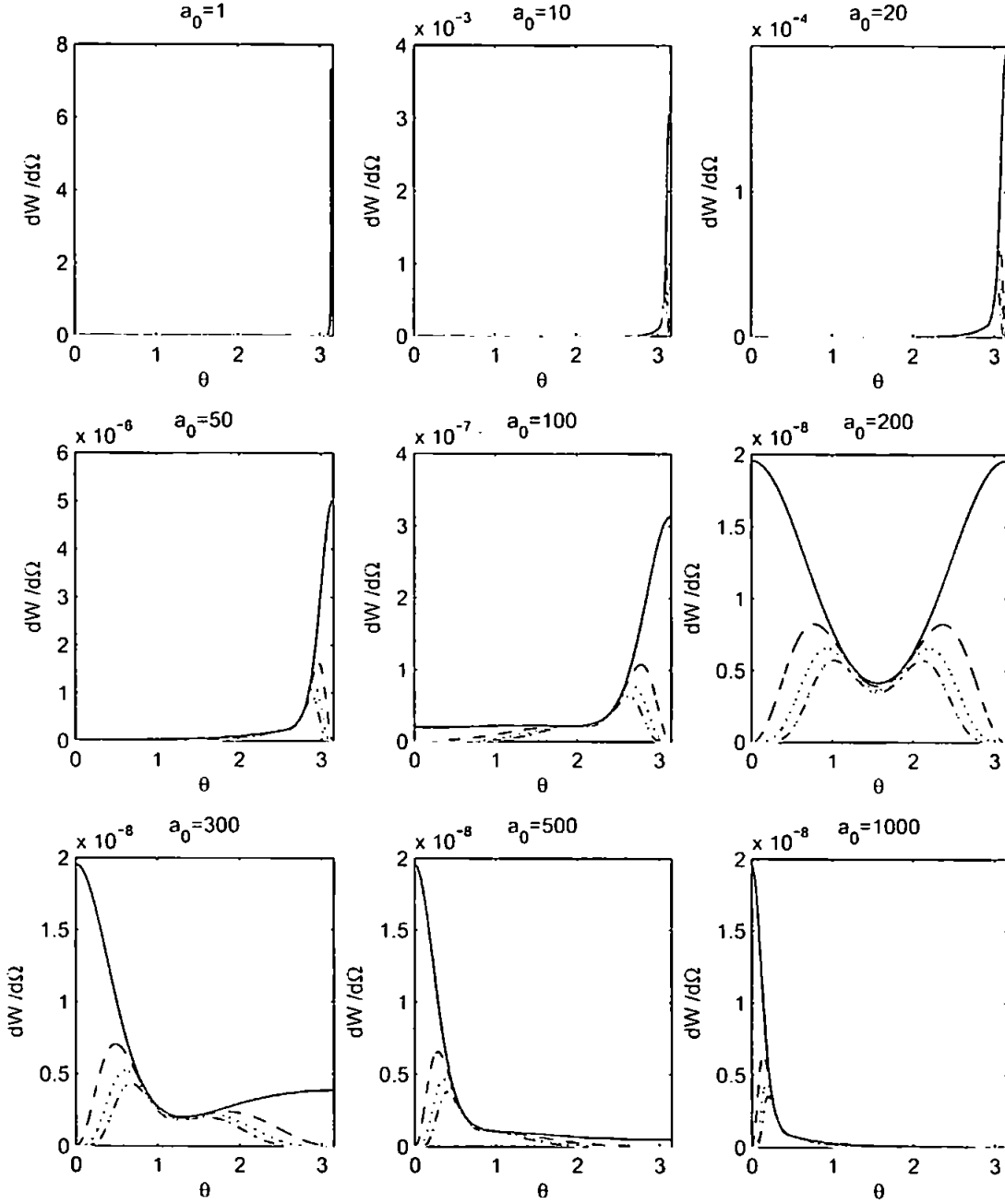
$$x_n(\theta) = \frac{2n\nu(1 - \cos\theta)}{\gamma[(1 + \beta)(1 + \cos\theta) + (1 + a_0^2)(1 - \beta)(1 - \cos\theta)]} = nx_1(\theta) \quad (5.57)$$

$$z_n(\theta) = 2n\sqrt{\frac{a_0^2}{1 + a_0^2}}\sqrt{\frac{x_1}{y_1}\left(1 - \frac{x_1}{y_1}\right)} = nz_1(\theta). \quad (5.58)$$

and we already have $y_n = ny_1$ from (5.50). We find it useful at this point to introduce the rescaled variable

$$r \equiv \frac{x_1}{y_1}, \quad 0 \leq r \leq 1. \quad (5.59)$$

Figure 5.15: Sequence of plots showing the first 5 angular harmonics for various a_0 ($\gamma = 100$). Solid line (black): $n = 1$, dashed: $n = 2$, dotted: $n = 3$, dashdot: $n = 4$, solid grey: $n = 5$.



Thus we may rewrite (5.58) as

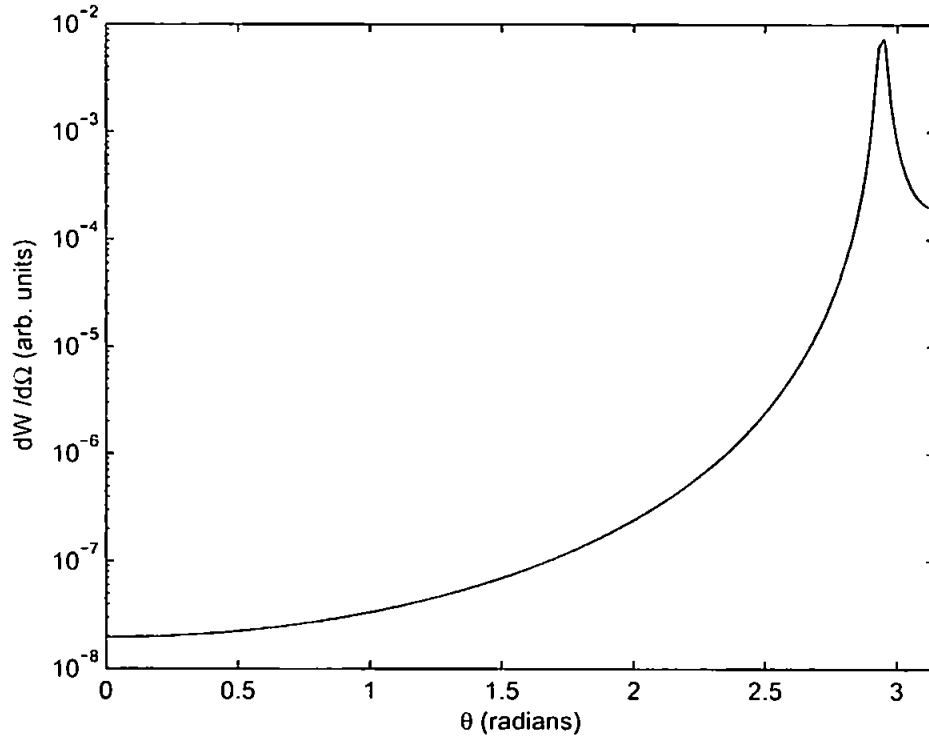
$$z_n(\theta) = 2n \sqrt{\frac{a_0^2}{1 + a_0^2}} \sqrt{r(1-r)}. \quad (5.60)$$

A simple differentiation shows that z_1 achieves its maximum when $r = 1/2$, and

thus z_1 lies in the interval

$$0 \leq z_1 \leq \sqrt{\frac{a_0^2}{1+a_0^2}} < 1. \quad (5.61)$$

Figure 5.16: Log plot of the angular emission rate summed to the first 5000 harmonics (FZD values).



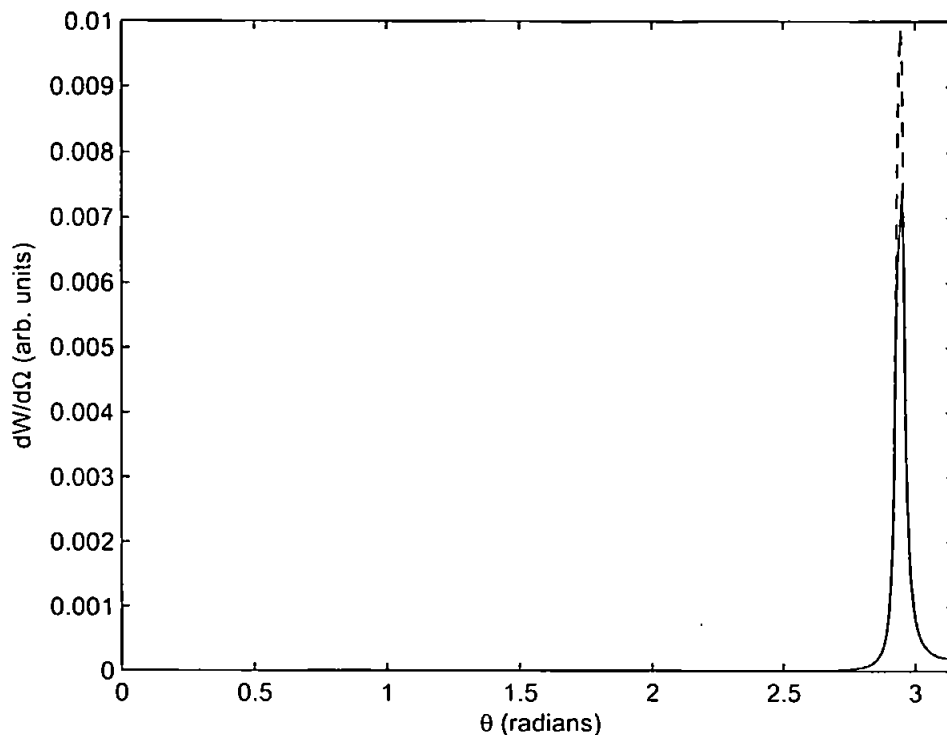
We are now ready to consider the total emission rate

$$\sum_{n=1}^{\infty} \frac{dW_n}{d\Omega} = \frac{n\nu}{\gamma(1+\beta)[1+j_n(1-\cos\theta)]^2} \mathcal{J}_n(z_n), \quad (5.62)$$

where we now have

$$\mathcal{J}_n(z_n) = -\frac{4}{a_0^2} J_n^2(nz_1) + \left(2 + \frac{n^2 r_1^2}{1+n r_1}\right) (J_{n+1}^2(nz_1) + J_{n-1}^2(nz_1) - 2J_n^2(nz_1)).$$

Figure 5.17: Angular emission rate summed to 5000 (solid line) and 10000 (dotted line) harmonics (FZD values). They only differ at the point $\theta = \theta_0 \approx 2.94$, which is the location of the peak.



Employing the Bessel function identity [46]

$$J_{n\pm 1}(z) = \frac{n}{z} J_n(z) \mp J'_n(z), \quad (5.63)$$

where the prime denotes the derivative of the Bessel function with respect to the argument z , we may write the emission rate as

$$\begin{aligned} \sum_{n=1}^{\infty} \frac{dW_n}{d\Omega} &= \sum_{n=1}^{\infty} A \left(\frac{(1-z_1^2)n^3x_1^3}{(1+nx_1)^3} + \frac{2(1-2z_1^2)n^2x_1^2}{(1+nx_1)^3} + \frac{(1-3z_1^2)nx_1}{(1+nx_1)^3} \right) J_n^2(nz_1) \\ &+ \sum_{n=1}^{\infty} B \left(\frac{n^3x_1^3}{(1+nx_1)^3} + \frac{2n^2x_1^2}{(1+nx_1)^3} + \frac{2nx_1}{(1+nx_1)^3} \right) J_n'^2(nz_1). \end{aligned}$$

where A and B are the n -independent prefactors

$$A = \frac{2\nu + x_1\gamma((1 + \beta) - (1 - a_0^2)(1 - \beta))}{\nu a_0^2 z_1^2 (1 - \cos \theta)},$$

$$B = \frac{4(1 - z_1^2)[2\nu + x_1\gamma((1 + \beta) - (1 + a_0^2)(1 - \beta))]}{2\nu z_1^2 (1 - \cos \theta)}.$$

We see that the terms of interest are the series of the form

$$\sum_{n=1}^{\infty} \frac{n^N}{(1 + nx_1)^3} J_n^2(nz_1) \quad \text{and} \quad \sum_{n=1}^{\infty} \frac{n^N}{(1 + nx_1)^3} J_n'^2(nz_1),$$

where $N \in \{1, 2, 3\}$. Since $x_1 > 0$ we can bound the series from above, e.g.

$$\sum_{n=1}^{\infty} \frac{n^N}{(1 + nx_1)^3} J_n^2(nz_1) < \sum_{n=1}^{\infty} n^N J_n^2(nz_1) \equiv S_N, \quad (5.64)$$

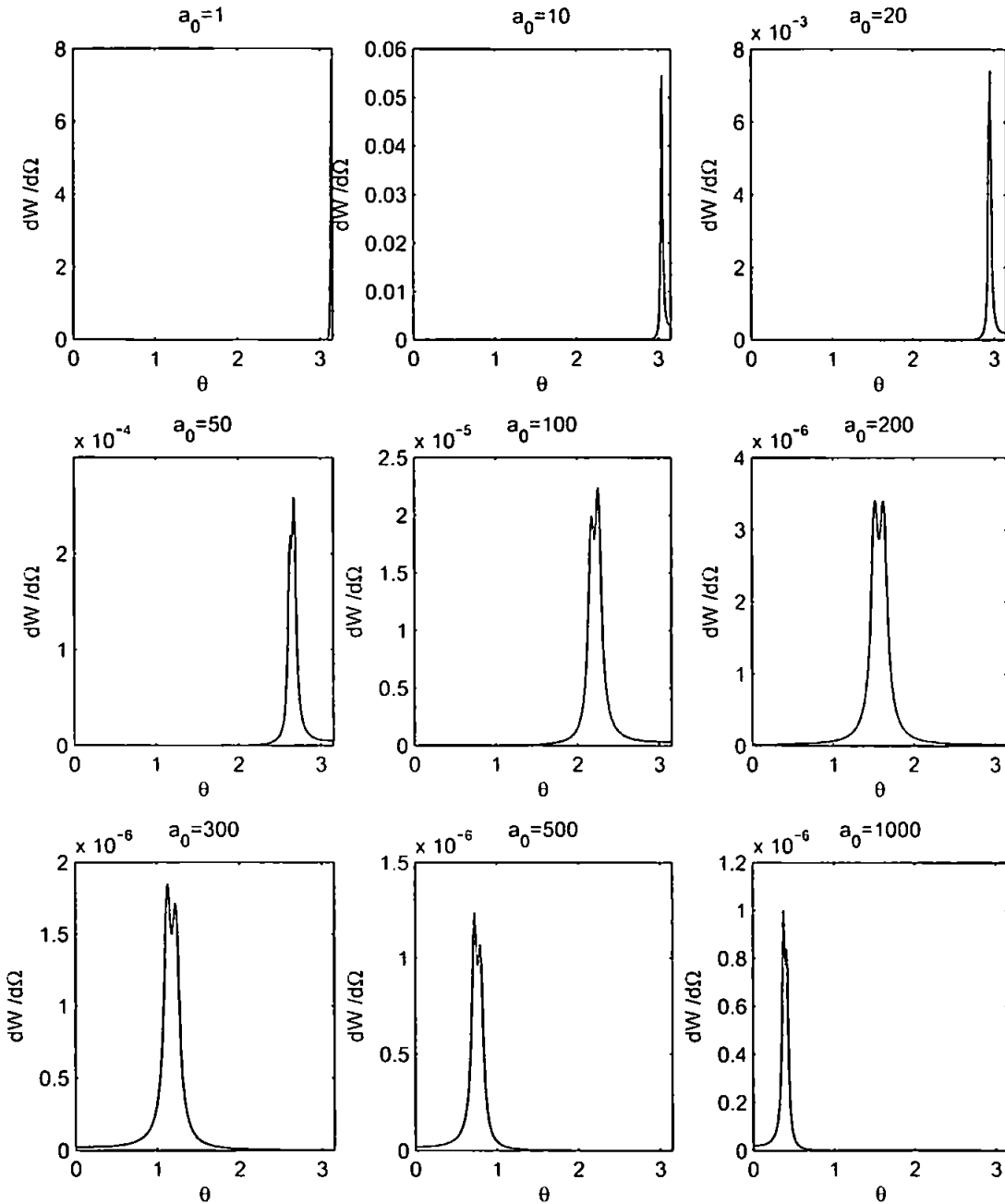
$$\sum_{n=1}^{\infty} \frac{n^N}{(1 + nx_1)^3} J_n'^2(nz_1) < \sum_{n=1}^{\infty} n^N J_n'^2(nz_1) \equiv S'_N. \quad (5.65)$$

The series S_N and S'_N are examples of Kapteyn series of the second kind and are known to converge when $0 \leq z_1 \leq 1$, which is true in our case due to (5.61). For an excellent discussion of these series and their convergence, we refer the reader to the papers [62] and [63] by Lerche and Tautz. In [62] the authors state that summing the series to 1000 terms yields errors below 10^{-6} for $z_1 \lesssim 0.95$. However, the convergence becomes very slow for z_1 close to 1. Thus the convergence will be slowest when z_1 is maximal, which we found earlier to be when $r = 1/2$. Calculating r explicitly, we find the angle where z_1 is maximised to be

$$\theta_0 = \arccos \frac{1 + a_0^2 + \gamma(1 - \beta)}{1 + a_0^2 + \gamma(1 + \beta)}. \quad (5.66)$$

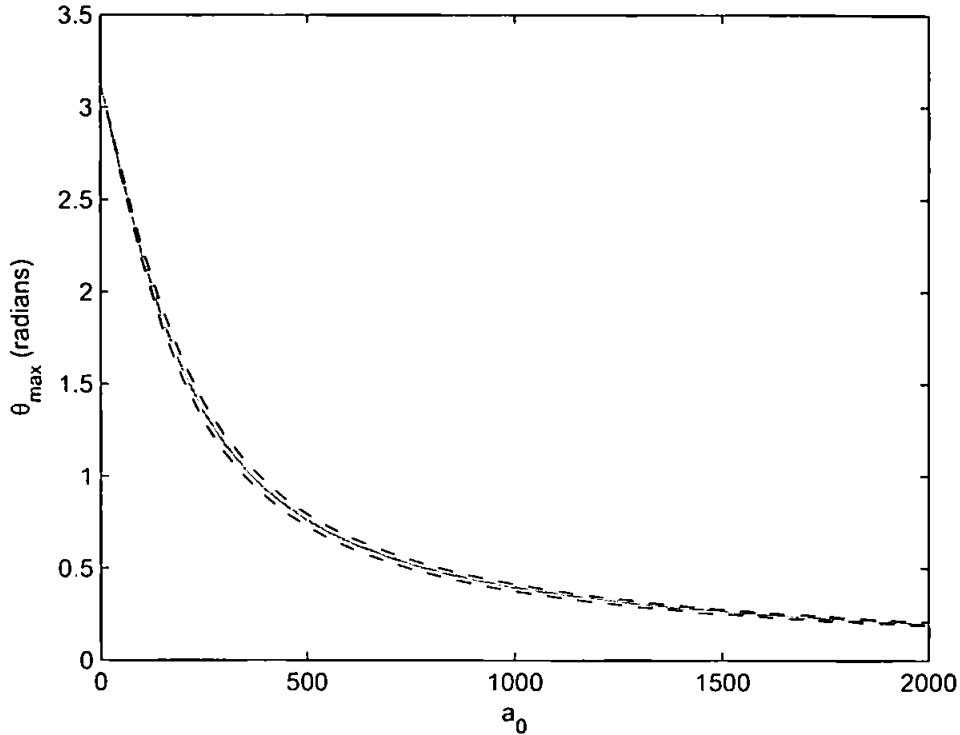
Figure 5.16 shows a plot of the emission rate summed to 5000 terms. We expect the convergence to be good everywhere apart from the small region around $\theta = \theta_0 \approx 2.94$, which is the location of the peak. In order to test how well the series

Figure 5.18: Sequence of plots showing the angular emission rate summed to 5000 harmonics for various a_0 ($\gamma = 100$).



has converged, in Figure 5.17 we have plotted the emission rate (for FZD values) summed to 5000 and 10000 terms. We can see that, as predicted, they only differ at the actual peak and so Figure 5.16 provides a relatively accurate representation of the angular emission rate. Considering this plot now with more confidence, we note the following observations. Firstly, for these parameter values the peak emission

Figure 5.19: Black dotted (outer lines): the angular positions of the two emission rate peaks as a function of a_0 (summed to 5000 harmonics, $\gamma = 100$). Grey solid (inner line): the angle θ_0 which defines the maximum of z_1 . We see that the point where z_1 is maximal and the convergence is slowest, corresponds to the local minima between the two peaks.



is close to the back scattering ($\theta = \pi$) direction, although the rate falls off at $\theta = \pi$ (the remaining shoulder at this point being solely due to the fundamental harmonic). Secondly, the angular rate is practically zero in the forward scattering ($\theta = 0$) direction.

In Figure 5.18 we investigate the dependence of the angular spectra on a_0 . We see that as a_0 is increased, the peak emission rate moves from the back scattering direction to the forward direction. In other words the laser gets 'stiffer' compared to the electron beam - the photons don't 'bounce back' (backscatter) so easily, but continue forwards (i.e. forward scatter) instead. It can be seen that the peak takes the form of a double peak which becomes symmetrical for $a_0 \approx 200$. In Figure 5.19 we determine numerically the positions of the two peaks and compare them to our

expression for θ_0 (5.66). It can be seen from this plot that θ_0 , the point where z_1 is maximal and convergence is slowest, corresponds to the local minima between the two peaks.

5.5 The Classical Limit

Having calculated the photon emission rates quantum mechanically, we now assess how these calculations compare to their classical counterparts. Keeping with the formalism we have used throughout this chapter, the classical limit may be expressed as (see Nikishov and Ritus [52])

$$y_n = \frac{2nk \cdot p}{m_*^2} \ll 1, \quad (5.67)$$

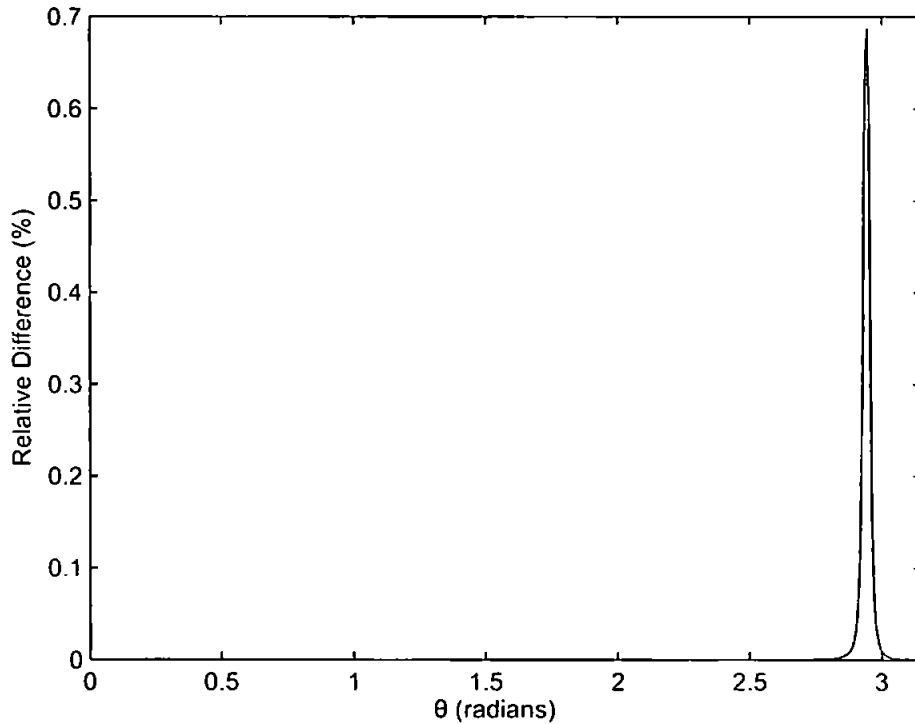
which is equivalent to stating that m_* is the dominant energy scale. Since y_n represents the recoil of the electron during the scattering process, the classical (Thomson) limit amounts to neglecting the transfer of momentum from the laser photons to the electron. From (5.67) we can see that we are in the classical limit if we have a large a_0 , and are not considering harmonics with a very large harmonic number. Since $x_n \leq y_n$, (5.67) may be expressed as

$$x_n \ll 1. \quad (5.68)$$

Thus we reach the classical limit if we take $x_n = nx_1$ to zero in our sums (5.64), (5.65). This argument is valid for large a_0 since for low harmonic numbers (5.68) clearly holds, and for high harmonic numbers the contributions to the sums are heavily suppressed by J_n^2 . In other words, this means that the bounding expression (5.64), (5.65) for the summed angular emission rate (5.62) is also the classical limit. If we now compare the quantum and classical (i.e. ‘Compton’ and ‘Thomson’)

emission rates we find, for $a_0 = 20$, that the graphs are nearly indistinguishable. Plotting the relative difference we find that it is effectively zero everywhere apart from a small region around $\theta = \theta_0$, where it rises to about 0.7% (Figure 5.20). This

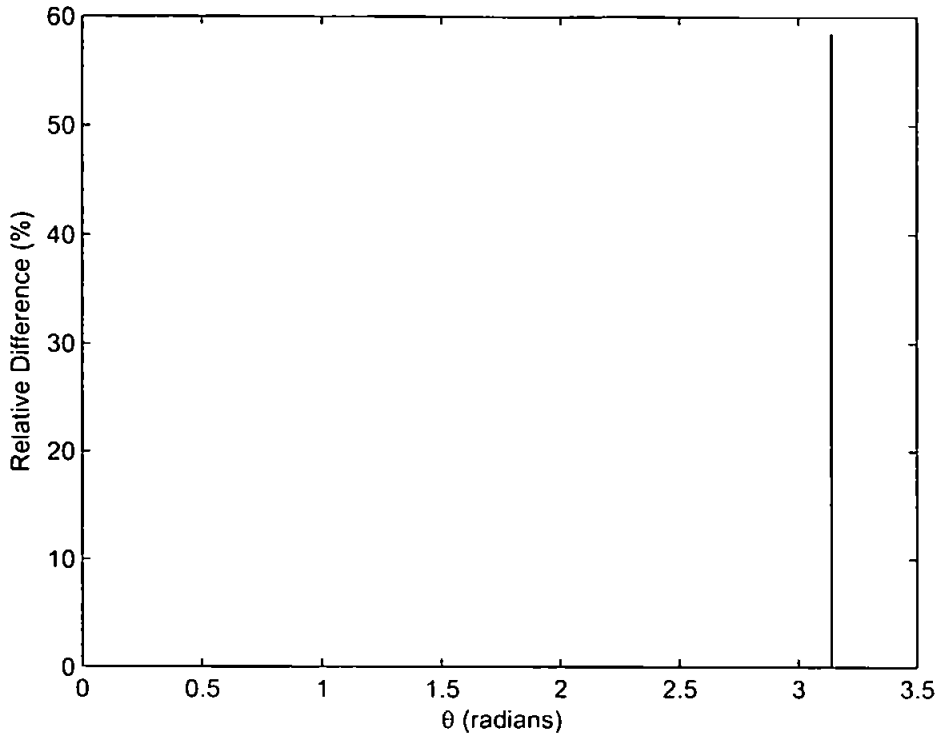
Figure 5.20: Relative difference of the photon emission rates $|\text{Compton} - \text{Thomson}|/\text{Compton}$ as a function of the scattering angle θ . FZD values, with harmonics summed to $n = 10000$.



is as we would expect since, for the FZD, $y_n \sim \mathcal{O}(10^{-6}) \ll 1$ putting us squarely in the classical regime. However, if we consider the SLAC E-144 experiment [28] where $\gamma \approx 10^5$ and $a_0 \approx 0.4$, then $y_n \sim \mathcal{O}(1)$ implying that quantum effects should be important. This is indeed the case – the difference between the quantum and classical calculations is as high as 60% (Figure 5.21).

As a final remark, we note that throughout this chapter we have considered the emission spectra in terms of the photon emission rates dW_n . We can relate these to

Figure 5.21: As Figure 5.20 but for parameter values corresponding to the SLAC E-144 experiment.



the emitted photon intensity dI_n by the relation [52]

$$dI_n = m\nu' dW_n. \quad (5.69)$$

5.6 Summary

To summarise, we have considered the phenomenology of laser-electron collisions using a strong field QED approach. Modelling the laser beam as an infinite plane wave, we analysed the signatures of intensity effects in Compton scattering. The main intensity effects are due to the intensity dependent mass shift $m^2 \rightarrow m_*^2 = m^2(1 + a_0^2)$ of the electron in the laser field. We predict that this will result in a redshift of the kinematic Compton edge for the fundamental harmonic, with the harmonic collapsing to a line spectrum for a critical a_0 . If observed, this will provide experimental

evidence of the electron mass shift. Our analysis also predicts the presence of higher harmonic peaks ($n > 1$) in the photon spectra. We emphasise that, for a circularly polarised laser field, the higher harmonics have not been detected in any previous experiment. We then considered the angular distribution of the emitted photons. This involved evaluating the sums of infinite series, the terms of which being functions of Bessel functions. This we achieved by employing Kapteyn series results. We subsequently found that, for low intensities, the peak emission is in the back scattering ($\theta = \pi$) direction. As the laser intensity is increased, the peak moves towards the forward scattering ($\theta = 0$) direction. Loosely speaking, at higher intensities the laser beam becomes ‘stiffer’ and so the laser photons stop ‘bouncing back’ from the electron (back scattering), instead continuing to move forwards (forward scattering). Finally, for the FZD parameters we found that the classical limit was in good agreement ($\lesssim 0.7\%$) with the strong field QED calculation. Thus, when carrying out more detailed modelling of the FZD experiments (considering the effects of the beam profile, for example), one can utilise the numerical scheme we presented in Chapter 4. For different parameter values, where $y_n \ll 1$ no longer holds, the classical limit no longer offers a suitable approximation and so one must proceed using strong field QED.

Chapter 6

Conclusion and Outlook

6.1 Summary

It is now 50 years since the invention of the laser and we find ourselves pushing the limits of what can be achieved. The next few years will see a succession of new experimental facilities coming online, each one with a power unmatched by anything that has gone before it. The resulting, unprecedentedly high, electromagnetic field strengths will allow the probing of fundamental physics in previously inaccessible regimes. The kinds of physics available (strong field QED – namely Compton scattering, vacuum birefringence and pair production) were outlined in Chapter 1. In this thesis we chose to devote our attention to the dynamics of electrons in such fields, with particular attention paid to intensity effects in the nonlinear Compton scattering emission spectra. The reason for this is that, out of all the different physical processes that it is possible to study using a laser field, nonlinear Compton scattering is the only one that does not have a minimum threshold of laser intensity, and is the most readily accessible with the facilities we expect to become available in the next few years.

We began our study in Chapter 2 by considering the classical behaviour of an electron in a constant electromagnetic field. Neglecting the effects of the radiative

back-reaction on the electron motion, the governing equation of motion is the Lorentz force equation (2.1). For the case of constant fields, this is solvable directly by exponentiation. The resulting electron orbits can be divided into four (Lorentz invariant) cases, classified by the values of the scalar and pseudo-scalar invariants of the field strength tensor. Parameterising the field tensor using a null tetrad, we demonstrated that the four cases result in electron motion that is either parabolic, elliptic, hyperbolic or loxodromic. In the parabolic case the field tensor describes crossed fields. Crossed fields are the most relevant case for us, since they represent either the high intensity or the long wavelength limit of an infinite plane wave. We thus proceeded to calculate the radiated energy spectra for an electron in a crossed field background. Doing so, we found that the radiation is almost exclusively backscattered, and the radiation signal strength decreases as the initial electron γ -factor is increased.

Having considered crossed fields, we then moved on to study infinite plane waves. The plane wave field tensors we considered were linear combinations of the (constant) crossed field tensors, multiplied by a light-cone time ($u \cdot x$) dependent prefactor. These fields are null and, due to their transversality, we found that the light cone time is directly proportional to the particle's proper time τ . Hence the Lorentz force equation becomes linear, and once again solvable by exponentiation. Calculating the electron trajectories we confirmed that, in the average rest frame, the electron exhibits figure-of-eight motion for a linearly polarised wave, and circular motion for a circularly polarised wave. The size of the orbits is proportional to the laser intensity a_0 . Considering the proper time average of the electron's momentum over a laser cycle, it was shown that the electron acquires a quasi-momentum, which in turn gives rise to an intensity dependent mass shift. In the case of circular polarisation, the radiated energy can be expressed in closed form. Evaluating the expression given by Sarachik and Schappert [47] for an electron initially at rest, we found that

the signal strength of the emitted radiation increases with the laser intensity. We also found that the emission peak moves closer to the forward scattering ($\theta = 0$) direction as the intensity is increased.

If one is to move on to consider more realistic/complex field configurations (modelling the laser field as a Gaussian beam, for example), then the Lorentz force equation will have to be solved numerically. Conventional numerical schemes are not covariant and will introduce a discretisation error into the on-shell condition. Therefore, in Chapter 4 we introduced a novel, first order numerical scheme based upon a $SL(2, \mathbb{C})$ representation of the electron four-velocity. Our method is fully covariant and so precisely preserves the on-shell condition. Using the example of a pulsed plane wave, we successfully demonstrated our new method and also compared it directly with a conventional first order scheme (the Euler method). We found our method to be more accurate, and we confirmed numerically that the on-shell condition is indeed preserved. We also remark that our method could be adapted to incorporate the radiative back-reaction, by solving the Landau-Lifshitz equation. More details are given in Appendix B.

Once we had studied the electron dynamics classically, we returned to consider the case of an infinite plane wave from a strong field QED perspective. Motivated by recent advances in laser technology, we paid particular attention to intensity effects in the emitted photon spectra. We found that the intensity dependent electron mass shift $m^2 \rightarrow m_*^2 \equiv m^2(1 + a_0^2)$ gives rise to an intensity dependent frequency shift of the kinematic Compton edge for the fundamental harmonic ($\omega' = 4\gamma^2\omega \rightarrow 4\gamma^2\omega/a_0^2$). In fact, for a given harmonic, we found that the notion of a 'centre-of-mass' frame becomes intensity dependent, with the first few harmonics collapsing to line spectra for $a_{0,\text{crit}} \approx 2\gamma$. For parameter values away from $a_0 = a_{0,\text{crit}}$ we found that the presence of the higher harmonics in the emission spectra serve to bolster the signal strength of the Compton peak. If detected in an experiment, this would be the

first time that the higher harmonics are detected for a circularly polarised laser field. After considering the emission spectra, we then turned our attention to the angular emission rates. We found that for low a_0 most of the emitted radiation is in the backscattering ($\theta = \pi$) direction. However, as a_0 is increased the emission peak moves away from $\theta = \pi$ and towards the forward scattering direction. This can be understood figuratively by saying that at low intensities the laser photons ‘bounce back’ off the electron (i.e. backscatter), whereas at higher intensities the laser becomes ‘stiffer’ and so the photons continue in a forwards direction (forward scatter). In order to calculate the angular rates we had to sum over an infinite number of harmonics. We solved this problem by realising that the sums could be bounded by Kapteyn series that can be written in closed form. We also found that the bounding expressions represent the classical limit to the problem, enabling us to compare the classical and quantum calculations with each other. For the FZD parameters we found that the classical limit was in very good agreement ($\lesssim 0.7\%$) with the full strong field QED calculation. This means that if one were to carry out more detailed modelling of the FZD experiments (e.g. considering the effects of the beam profile), one could utilise the numerical scheme we developed in Chapter 4. However, for different parameter values, where the condition

$$y_n = \frac{2nk \cdot p}{m_e^2} \ll 1 \quad (6.1)$$

no longer holds, the classical limit no longer offers a suitable approximation and so one must proceed using strong field QED. This was aptly demonstrated for the SLAC E-144 experiment, where we found that the relative difference between the classical and QED calculation is as high as 60%.

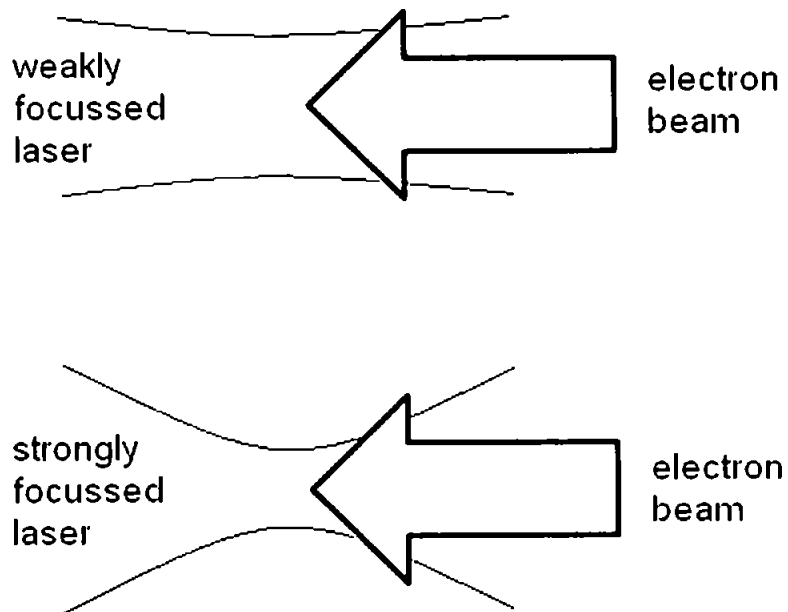
6.2 Further Developments and Outlook

Over the next few years we can expect a wealth of new experimental data against which to compare our theoretical predictions. The results from the FZD will be especially interesting for us, since they will allow us to gauge the validity of our reasoning in Chapter 5. It would be particularly exciting to confirm our predictions regarding the tunability of the Compton peak in the emission spectrum. If demonstrated, this process could potentially provide a source of monochromatic X-rays of tunable frequency, which could be of use in cancer therapies and other scientific fields. In terms of fundamental physics benefits, if the experiments are able to detect the presence of the higher harmonics in the emission spectrum, this would be the first time that they were detected for a circularly polarised laser field.

While our analysis of an infinite plane wave laser model was an important first step, the challenge now is to consider a more realistic model of the laser beam. Indeed, since our work on the emission spectrum for an electron in an infinite plane wave was carried out, other authors have begun to give consideration to the effects that changing from an infinite plane wave to a pulsed plane wave has on the spectrum. In particular, the work by Heinzl, Seipt and Kämpfer [44] contains a classical calculation of the emission spectrum for an electron in a circularly polarised, pulsed plane wave (not including the radiative back-reaction). Their key finding was that, since the field strength varies as the electron passes through the pulse, radiation generated at different times will be of different frequencies. The result of this is that the emission harmonics develop additional oscillatory substructures, which are not present in the plane wave analysis. As well as considering finite temporal effects, at much higher intensities it will also be necessary to consider finite spatial effects. This is because one of the ways in which the laser intensity can be increased is by focussing the beam more strongly. This will mean that the electron beam will no

longer be narrow compared to the laser beam waist size, and so we can no longer assume that the electrons probe just the central focus region – see Figure 6.2. Thus one must move beyond plane wave models and treat the laser as a Gaussian beam. For parameter values that place us well within the classical domain, the numerical scheme we introduced in Chapter 4 can be utilised. However, outside of the classical regime we will be forced to find a way to perform such calculations using strong field QED.

Figure 6.1: The implications of beam focussing on our modelling. For a strongly focussed beam, the electrons can no longer be assumed to probe just the central focus, and so spatial effects must be taken into consideration.



Aside from nonlinear Compton scattering, the intensities available at future facilities – ELI in particular – will allow other processes to be studied. The intensities expected at ELI may be high enough to detect the effects of vacuum birefringence on the polarisation of probe photons, although it will still be well below the Schwinger limit at which vacuum pair production may take place. However, pair production experiments are possible, utilising phenomena such as the Breit-Wheeler process. Finally, we must make some remarks concerning the radiative back reaction. In this

thesis our classical analysis neglected these effects, and so took the Lorentz equation to govern the electron motion. However, the numerical scheme introduced in Chapter 4 could be adapted to solve the Landau-Lifshitz equation, which incorporates the back reaction via reduction of order. Nevertheless, one often finds that for parameter ranges where the back reaction becomes important, quantum effects also become significant. Thus we must ask whether one can disentangle the radiation reaction from quantum corrections. There are many contributions to the literature on this subject, but we consider the notes by McDonald [79] to be particularly useful.

Appendix A

Notation

Throughout we will be working in four-dimensional Minkowski space, defined with a metric such that a covariant vector x_μ ($\mu = 0, 1, 2, 3$) is related to its contravariant counterpart x^μ by

$$x_\mu = g_{\mu\nu}x^\nu, \quad g = \text{diag}(1, -1, -1, -1), \quad (\text{A.1})$$

where repeated indices are summed over. A particle's position $x^\mu(\tau)$ is parameterised by its proper time τ , such that

$$d\tau = \sqrt{dx_\mu dx^\mu}. \quad (\text{A.2})$$

Thus we may define a particle's four-velocity as

$$du_\mu \equiv \frac{dx_\mu}{d\tau} = \gamma(c, \mathbf{v}), \quad (\text{A.3})$$

where \mathbf{v} is the standard three-velocity $\mathbf{v} = d\mathbf{x}/dx^0$ and

$$\gamma = \frac{1}{\sqrt{1 - v^2/c^2}}, \quad (\text{A.4})$$

Similarly, a particle's four-momentum is simply $p_\mu \equiv mu_\mu = (E_p/c, \mathbf{p})$, where m is the particle mass and $E_p = m\gamma$ is its energy. An electromagnetic field is characterised by its four-potential $A_\mu = (\phi, \mathbf{A})$, which in turn allows us to define the electric field intensity \mathbf{E}

$$\mathbf{E} = -\frac{1}{c} \frac{\partial \mathbf{A}}{\partial x^0} - \text{grad}\phi. \quad (\text{A.5})$$

and the magnetic field intensity

$$\mathbf{B} = \text{curl}\mathbf{A}. \quad (\text{A.6})$$

We define the antisymmetric tensor $F_{\mu\nu}$ (the electromagnetic field tensor)

$$F_{\mu\nu} = \partial_\mu A_\nu - \partial_\nu A_\mu \quad (\text{A.7})$$

$$= \begin{pmatrix} 0 & E_1 & E_2 & E_3 \\ -E_1 & 0 & -B_3 & B_2 \\ -E_2 & B_3 & 0 & -B_1 \\ -E_3 & -B_2 & B_1 & 0 \end{pmatrix}, \quad (\text{A.8})$$

where we have introduced the notation

$$\partial_\mu \equiv \frac{\partial}{\partial x^\mu} = \left(\frac{\partial}{\partial x^0}, \nabla \right). \quad (\text{A.9})$$

We also introduce the electromagnetic energy-momentum tensor

$$T_{\mu\nu} \equiv \frac{1}{\mu_0} \left(-F_{\mu\alpha} F^\alpha{}_\nu - \frac{1}{4} g_{\mu\nu} F^{\delta\gamma} F_{\delta\gamma} \right). \quad (\text{A.10})$$

Appendix B

The Radiation Back-Reaction

In this Appendix we consider the full equation of motion for an electron in an electromagnetic field – including the radiative back-reaction. The classical action for such a system can be written as [37]

$$S = -m \int d\tau - e \int d^1x j^\mu A_\mu - \frac{1}{4} \int d^2x F^{\mu\nu} F_{\mu\nu}, \quad (\text{B.1})$$

where the gauge potential A^μ refers to the total field and j^μ is the four-current as defined in (2.40). We can express the field strength tensor as a sum of the tensor describing the external laser field $F_{\text{ext}}^{\mu\nu}$, plus the tensor describing the back-reaction on the field $F_{\text{R}}^{\mu\nu}$

$$F^{\mu\nu} = F_{\text{ext}}^{\mu\nu} + F_{\text{R}}^{\mu\nu}. \quad (\text{B.2})$$

Assuming the laser field is a solution of the vacuum Maxwell equations

$$\partial_\mu F_{\text{ext}}^{\mu\nu} = 0. \quad (\text{B.3})$$

and varying the action with respect to the gauge field A^μ and to the trajectory x^μ , one finds the following governing equations

$$\partial_\mu F_{\text{R}}^{\mu\nu} = j^\nu(x), \quad (\text{B.4})$$

$$\dot{u}^\mu = \frac{e}{m}(F_{\text{ext}}^{\mu\nu} + F_{\text{R}}^{\mu\nu})u_\nu. \quad (\text{B.5})$$

The solution to these equations is due to Lorentz [69], Abraham [70] and Dirac [71] and is presented clearly by Coleman [72]. The resulting equation of motion is known as the Lorentz-Abraham-Dirac equation and can be expressed in the form

$$\ddot{u}^\mu = \frac{e}{m}F_{\text{ext}}^{\mu\nu}u_\nu - \frac{2}{3}\frac{e^2}{4\pi m}(\ddot{u}^\mu + \dot{u}^2 u^\mu). \quad (\text{B.6})$$

We draw the reader's attention to the presence of the infamous second derivative term \ddot{u}^μ (third derivative of x^μ), which leads to the existence of runaway solutions.

A well known solution to this problem is to replace the \ddot{u}^μ and \dot{u}^2 terms using the Lorentz force equation (2.1) [37], thus 'reducing the order' of (B.6). The resulting equation is known as the Landau-Lifshitz equation

$$\ddot{u}^\mu = \frac{e}{m}F^{\mu\nu}u_\nu - \frac{2}{3}\frac{e^2}{4\pi} \left\{ \frac{e}{m^2}\dot{F}^{\mu\nu}u_\nu + \frac{e^2}{m^3}F^{\mu\alpha}F_\alpha{}^\nu u_\nu - \frac{e^2}{m^3}u_\alpha F^{\alpha\nu}F_\nu{}^\beta u_\beta u^\mu \right\}, \quad (\text{B.7})$$

where we have changed notation to $F \equiv F_{\text{ext}}$ and we will from now on drop the subscript for clarity. This derivation is valid under the conditions that, in the instantaneous electron rest frame, both the laser frequency $\hbar\omega$ and the electric field energy eE are much smaller than the electron rest energy mc^2 [37]. The derivation of the Landau-Lifshitz equation has recently been underpinned with more mathematical rigour in [73] and [74].

Denoting the square of $F^{\mu\nu}$ by $\Theta^{\mu\nu}$

$$\Theta^{\mu\nu} \equiv F^{\mu\alpha} F_{\alpha}{}^{\nu}, \quad (\text{B.8})$$

we can write (B.7) as

$$\dot{u}^{\mu} = \frac{e}{m} (F^{\mu\nu} + G^{\mu\nu}) u_{\nu} =: \frac{e}{m} H^{\mu\nu} u_{\nu}, \quad (\text{B.9})$$

where

$$G^{\mu\nu} \equiv -\frac{2}{3} \frac{e}{4\pi} \left\{ \frac{e}{m} \dot{F}^{\mu\nu} - \frac{e^2}{m^2} (u^{\mu} \Theta^{\nu}{}_{\alpha} - u^{\nu} \Theta^{\mu}{}_{\alpha}) u^{\alpha} \right\}, \quad (\text{B.10})$$

is manifestly anti-symmetric. We note once again that in the special case of a plane wave field $\Theta^{\mu\nu} = T^{\mu\nu}$. The fact that the Landau-Lifshitz equation can be expressed as a combination of anti-symmetric tensors (B.9) means that the new numerical scheme we presented in Chapter 4 could be adapted to solve it.

To solve the Landau-Lifshitz equation using our numerical scheme, we would adopt a $\text{SL}(2, \mathbb{C})$ basis and discretise, just as in Chapter 4. However, when defining our electric field matrix (4.8)

$$\mathbb{E}^{\dagger} = (\mathbf{E} + i\mathbf{B}) \cdot \boldsymbol{\sigma}, \quad (\text{B.11})$$

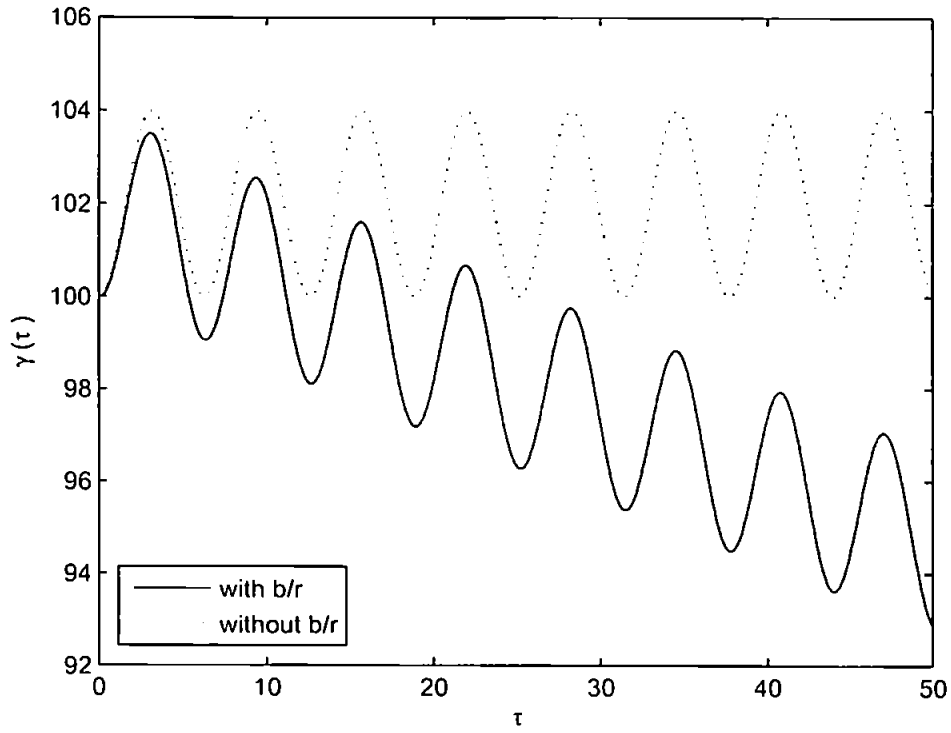
we now take our \mathbf{E} and \mathbf{B} fields to include the *full* electromagnetic field, i.e.

$$H_{0i}(x) =: E_i(x), \quad H_{ik}(x) =: -\epsilon_{ikm} B_m(x). \quad (\text{B.12})$$

It has recently been shown by Di Piazza [68] that, for the case of a plane wave field, the Landau-Lifshitz equation can be solved analytically. Using this solution, in Figure B.1 we show a plot of the electron γ -factor for the FZD parameters, show-

ing both the Lorentz (no back-reaction) and Landau-Lifshitz (with back-reaction) solutions. The difference between them is $\mathcal{O}(1\%)$ over the first laser cycle.

Figure B.1: Plot showing the electron γ -factor for a circularly polarised plane wave, with and without radiation damping effects (FZD values).



Bibliography

- [1] C. H. Townes, *The First Laser from A Century of Nature: Twenty-One Discoveries that Changed Science and the World*, The University of Chicago Press (2003).
- [2] Physics World (Topical Issue) ‘*The Laser at 50*’, 23, 5 (2010).
- [3] Encyclopaedia of Laser Physics and Technology
http://www.rp-photonics.com/chirped_pulse_amplification.html.
- [4] D. Strickland and G. Mourou, *Compression of Amplified Chirped Optical Pulses*, Opt. Commun. 56, 219 (1985).
- [5] V. Yanovsky *et al*, *Ultra-High Intensity 300 TW Laser at 0.1 Hz Repetition Rate*, Optics Express 16, 2109 (2008).
- [6] The European Extreme Light Infrastructure (ELI) project:
<http://extreme-light-infrastructure.eu>.
- [7] T. Tajima (ed.) *Report on the ELI Science*, Scientific Advisory Committee of Extreme Light Infrastructure (2009), available to download from
<http://www.eli-laser.eu>.
- [8] F. Amiranoff *et al*, *Proposal for a European Extreme Light Infrastructure (ELI)* (2005), available to download from <http://www.eli-laser.eu>.
- [9] The Large Hadron Collider, <http://lhc.web.cern.ch/lhc/>.

- [10] F. Grüner *et al*, *Design Considerations for Table-Top, Laser-Based VUV and X-ray Free Electron Lasers*, Appl. Phys. B **86**, 431 (2007).
- [11] W. Thomlinson, P. Suortti and D. Chapman, *Recent Advances in Synchrotron Radiation Medical Research*, Nuc. Instr. and Meth. in Phys. Res. A **543**, 288 (2005).
- [12] R. Neutze *et al*, *Potential for Biomolecular Imaging With Femtosecond X-ray Pulses*, Nature **406**, 752 (2000).
- [13] J. Weichsel, *et al*, *Spectral features of laser-accelerated protons for radiotherapy applications*, Phys. Med. Biol. **53**, 4383 (2008).
- [14] T. Tajima and J. M. Dawson, *Laser Electron Accelerator*, Phys. Rev. Lett. **43**, 267 (1979).
- [15] J. L. Hsu, *et al*, *Laser Acceleration in Vacuum*, Am. Inst. Phys. Conf. Ser., **396**, 21 (1997).
- [16] R. Feynman, *The Feynman Lectures on Physics, Vol. I*. Addison-Wesley, (1965).
- [17] F. V. Hartemann, *High-Field Electrodynamics*, CRC Press LLC (2002).
- [18] F. Krausz, *Photonics I – The Theory of Light and its Advanced Applications*, Unpublished lecture notes (2006).
- [19] J. D. Jackson, *Classical Electrodynamics*, John Wiley and Sons, Inc., (1999).
- [20] A. I. Nikishov and V.I. Ritus, *Nonlinear Effects in Compton Scattering and Pair Production Owing to Absorption of Several Photons*, Sov. Phys. JETP **20**, 757 (1965).

- [21] J. S. Toll, *The Dispersion Relation for Light and its Application to Problems Involving Electron Pairs*, PhD Thesis, Princeton (1952).
- [22] T. Heinzl and A. Ilderton, *Exploring High-Intensity QED at ELI* (arXiv:0811.1960) to appear in a topical issue of Eur. Phys. J. D on *Fundamental Physics and Ultra-High Laser Fields*.
- [23] T. Heinzl *et al*, *On the Observation of Vacuum Birefringence*, Opt. Commun. **267**, 318 (2006).
- [24] J. S. Schwinger, *On Gauge Invariance and Vacuum Polarization*, Phys. Rev. **82**, 664 (1951).
- [25] F. Sauter, *Über das Verhalten eines Elektrons im homogenen elektrischen Feld nach der relativistischen Theorie Diracs*, Z. Phys. **69**, 742 (1931).
- [26] A. I. Nikishov and V. I. Ritus, *Pair Production by a Photon and Photon Emission by an Electron in the Field of an Intense Electromagnetic Wave and in a Constant Field*, Sov. Phys. JETP **25**, 1135 (1967).
- [27] K.T. McDonald, *Proposal for Experimental Studies of Nonlinear Quantum Electrodynamics*, preprint DOE/ER/3072 (1986), available as <http://www.hep.princeton.edu/mcdonald/e144/prop.pdf>.
- [28] C. Bamber *et al*, *Studies of Nonlinear QED in Collisions of 46.6-GeV Electrons With Intense Laser Pulses*, Phys. Rev. D **60**, 092004 (1999).
- [29] L. W. Davis, *Theory of Electromagnetic Beams*, Phys. Rev. A **19**, 1177 (1979).
- [30] N. B. Narozhny and M. S. Fofanov, *Anisotropy of Electrons Accelerated by a High-Intensity Laser Pulse*, Phys. Lett. A **295**, S7 (2002).

- [31] P. Tomassini, *et al*, *Thomson Backscattering X-rays from Ultra-Relativistic Electron Bunches and Temporally Shaped Laser Pulses*, Appl. Phys. B **80**, 419 (2005).
- [32] T. Heinzl and A. Ilderton, *A Lorentz and Gauge Invariant Measure of Laser Intensity*, Opt. Commun. **282**, 1879 (2009).
- [33] G. Priebe *et al*, *Inverse Compton Backscattering Source Driven by the Multi-10 TW Laser Installed at Daresbury*, Laser and Particle Beams, **26**, 649 (2008).
- [34] Forschungszentrum Dresden - Rossendorf: <http://www.fzd.de>.
- [35] Science and Technology Facilities Council *Central Laser Facility, Annual Report 2008-2009*.
- [36] Vulcan Laser <http://www.clf.stfc.ac.uk>.
- [37] L. Landau and E. Lifshitz, *The Classical Theory of Fields (Course of Theoretical Physics)*, Pergamon Press, 1975.
- [38] A. H. Taub, *Orbits of Charged Particles in Constant Fields*, Phys. Rev. **73**, 786 (1948).
- [39] H. Stephani, *Relativity*. Cambridge University Press, (2004).
- [40] http://en.wikipedia.org/wiki/Lorentz_group.
- [41] A. T. Hymn, *Relativistic Charged-Particle Motion in a Constant field According to the Lorentz Force Law*, Am. J. Phys., **65**, 3 (1997).
- [42] R. Feynman, *The Feynman Lectures on Physics, Vol. II*. Addison-Wesley, (1965).
- [43] H. Mitter, unpublished lectures on electrodynamics, 1998 (in German), available at <http://physik.uni-graz.at/~hem/>

- [44] T. Heinzl, D. Seipt and B. Kämpfer, *Beam-Shape Effects in Nonlinear Compton and Thomson Scattering*, Phys. Rev A **81**, 022125 (2010).
- [45] T. Heinzl, *Light-Cone Quantisation: Foundations and Applications*, Lect. Notes Phys. **572**, 55 (2001).
- [46] M. Abramowitz and I. A. Stegun, *Handbook of Mathematical Functions*, Dover, New York (1972).
- [47] E. S. Sarachik and G. T. Schappert, *Classical Theory of the Scattering of Intense Laser Radiation by Free Electrons*, Phys. Rev. D **1**, 2738 (1970).
- [48] E. Esarey, S. K. Ride and P. Sprangle, *Nonlinear Thomson Scattering of Intense Laser Pulses from Beams and Plasmas*, Phys. Rev. E **48**, 3003 (1993).
- [49] L. S. Brown and T. W. Kibble, *Interaction of Intense Laser Beams With Electrons*, Phys. Rev. **133**, 705 (1964).
- [50] T.W. Kibble, *Frequency Shift in High-Intensity Compton Scattering* Phys. Rev. **138**, 3B (1965).
- [51] I.I. Goldman, *Intensity Effects in Compton Scattering*, Phys Lett. **8**, 2 (1963).
- [52] A. I. Nikishov and V. I. Ritus, *Quantum Processes in the Field of a Plane Electromagnetic Wave and in a Constant Field. I*, Soviet Physics JETP, **19**, 529 (1964).
- [53] A. I. Nikishov and V. I. Ritus, *Quantum Processes in the Field of a Plane Electromagnetic Wave and in a Constant Field. II*, Soviet Physics JETP, **19**, 1191 (1964).
- [54] D.M. Volkov, Z. Phys. **94**, 250 (1935).

- [55] N. D. Sengupta, *On the Scattering of Electromagnetic Waves by Free Electron - I. Classical Theory*, Bull. Math. Soc. (Calcutta) **41**, 187 (1949).
- [56] N. D. Sengupta, *On the Scattering of Electromagnetic Waves by Free Electron - II. Wave Mechanical Theory*, Bull. Math. Soc. (Calcutta) **44**, 175 (1952).
- [57] V.B. Berestetskii, E.M. Lifshitz and L.P. Pitaevskii, *Landau and Lifshitz Course of Theoretical Physics, Vol. 4, Quantum Electrodynamics 2nd Edition*, Butterworth-Heinemann, (1982).
- [58] T.W.B. Kibble, *Kinematics of General Scattering Processes and the Mandelstam Representation*, Phys. Rev. **117**, 4 (1960).
- [59] T. Heinzl, A. Iderton and M. Marklund, *Finite Size Effects in Stimulated Laser Pair Production*, arXiv:1002.4018v1 [hep-ph] (2010).
- [60] S. Chen *et al.*, *Experimental Observation of Relativistic Nonlinear Thomson Scattering*, Nature **396**, 653 (1998).
- [61] M. Babzien *et al.*, *Observation of the Second Harmonic in Thomson Scattering from Relativistic Electrons*, Phys. Rev. Lett. **96**, 054802 (2006).
- [62] I. Lerche and R. C. Tautz, *Kapteyn Series Arising In Radiation Problems*, J. Phys. A: Math. Theor. **41**, 035202 (2008).
- [63] I. Lerche and R. C. Tautz, *A Note on the Summation of Kapteyn Series in Astrophysical Problems*, Astrophys. J. **665**, 1288 (2007).
- [64] Y. Y. Lau *et al.*, *Nonlinear Thomson Scattering: A Tutorial*, Phys. Plasmas **10**, 2155 (2003).
- [65] J. Campbell, *On a Law of Combination of Operators*, Proc. Lond. Math. Soc., **29**, 14 (1898).

- [66] J. Koga, T. Z. Esirkepov, S. V. Bulanov, *Nonlinear Thomson Scattering in the Strong Radiation Damping Regime*, Phys. Plasmas **12**, 093106 (2005).
- [67] A. Di Piazza, K. Z. Hatsagortsyan and C. H. Keitel, *Strong Signatures of Radiation Reaction Below the Radiation-Dominated Regime*, Phys. Rev. Lett. **102**, 254802 (2009).
- [68] A. Di Piazza, *Exact Solution of the Landau-Lifshitz Equation in a Plane Wave*, Lett. Math. Phys. **83**, 305 (2008).
- [69] H. A. Lorentz, *The Theory of Electrons*, B. G. Teubner, Leipzig, (1905); reprinted by Dover Publications, New York, (1952) and Cosimo, New York, (2007).
- [70] M. Abraham, *Theorie der Elektrizität*, Teubner, Leipzig, (1905).
- [71] P. A. M. Dirac, *Classical Theory of Radiating Electrons*, Proc. Roy. Soc. A **167**, 148 (1938).
- [72] S. Coleman, in: *Electromagnetism, Paths to Research*, D. Teplitz, ed., Plenum, New York, (1982).
- [73] S. E. Gralla, A. I. Harte and R. M. Wald, *A Rigorous Derivation of the Electromagnetic Self-Force*, Phys. Rev. D **80**, 024031 (2009).
- [74] H. Spohn, *The Critical Manifold of the Lorentz-Dirac Equation*, Europhys. Lett. **49**, 287 (2000).
- [75] C. Itzykson, J. B. Zuber, *Quantum Field Theory*, McGraw-Hill, (1980).
- [76] N. Salingaros, *Particle in an External Electromagnetic Field, II. The Exact Velocity in a Constant and Uniform Field.*, Phys. Rev. D **31**, 3150 (1985).

- [77] A. Quarteroni, R. Sacco, F. Saleri, *Numerical Mathematics Second Edition*, Springer (2007).
- [78] J. Schreiber *et al*, *Analytical Model for Ion Acceleration by High-Intensity Laser Pulses*, Phys. Rev. Lett. **97**, 045005 (2006).
- [79] K. T. McDonald, *Limits on the Applicability of Classical Electromagnetic Fields as Inferred from the Radiation Reaction*, unpublished preprint, available from <http://www.hep.princeton.edu/mcdonald/examples/radreact.pdf>.

Signatures of high-intensity Compton scattering

Chris Harvey^{*} and Thomas Heinzl[†]*School of Mathematics and Statistics, University of Plymouth, Drake Circus, Plymouth PL4 8AA, United Kingdom*Anton Ilderton[‡]*School of Mathematics, Trinity College, Dublin 2, Ireland*

(Received 2 April 2009; published 15 June 2009)

We review known and discuss new signatures of high-intensity Compton scattering assuming a scenario where a high-power laser is brought into collision with an electron beam. At high intensities one expects to see a substantial redshift of the usual kinematic Compton edge of the photon spectrum caused by the large, intensity-dependent effective mass of the electrons within the laser beam. Emission rates acquire their global maximum at this edge while neighboring smaller peaks signal higher harmonics. In addition, we find that the notion of the center-of-mass frame for a given harmonic becomes intensity dependent. Tuning the intensity then effectively amounts to changing the frame of reference, going continuously from inverse to ordinary Compton scattering with the center-of-mass kinematics defining the transition point between the two.

DOI: 10.1103/PhysRevA.79.063407

PACS number(s): 12.20.Ds

1. INTRODUCTION

The technological breakthrough of laser chirped-pulse amplification [1] has led to unprecedented laser powers and intensities, the current records being about 1 Petawatt (PW) and 10^{22} W/cm², respectively. Within the next few years these are expected to be superseded by an increase of about 1 order of magnitude each, for instance at the upgraded Vulcan laser facility [2]. Up to 3 orders of magnitude may be gained at the planned "Extreme Light Infrastructure" (ELI) facility [3]. This progress calls for a reassessment of intensity effects in QED and the new prospects of measuring them (see, e.g., [4–6] for discussions of strong-field physics at Vulcan and ELI). There is a plethora of strong-field QED processes, which may be roughly categorized into two classes: loop and tree-level processes. The former include strong-field vacuum polarization, the real part of which describes vacuum birefringence [7] (for a recent discussion, see [8]), while its imaginary part signals Breit-Wheeler pair production [9]. Summing all orders of these one-loop diagrams (in the low-energy limit) one obtains the Heisenberg-Euler effective Lagrangian [10] which in turn yields Schwinger's nonperturbative mechanism of spontaneous pair production from the vacuum [11]. The optical theorem and crossing symmetry relate these one-loop diagrams to tree-level processes such as perturbative pair production, pair annihilation, and Compton scattering.

It is well known that one-loop processes are of order \hbar and thus of a genuine quantum nature, while tree level processes generically do have a classical limit. As a result, one can introduce two distinct parameters which characterize the different physics involved. The first parameter is the QED electrical field,

$$E_c \equiv \frac{m^2 c^3}{eh} = 1.3 \times 10^{18} \text{ V/m}, \quad (1)$$

first introduced by Sauter [12] in his analysis of Klein's paradox [13]. The presence of Planck's constant, \hbar , and the speed of light, c , show that E_c originates from a relativistic quantum-field theory. In an electric field of strength E_c an electron acquires an electromagnetic energy equal to its rest mass mc^2 upon traversing a distance of a Compton wavelength, $\lambda_c = \hbar/mc$. Hence, E_c may be viewed as the critical-field strength above which vacuum pair production becomes abundant. This is also borne out by Schwinger's pair-creation probability given by the tunneling factor $p \sim \exp(-\pi E_c/E)$ [11], where E denotes the "ambient" electric field one succeeds in achieving. Currently, this is $E \approx 10^{14}$ V/m implying a huge exponential suppression. The perturbative variant of the Schwinger process, i.e., the (strong-field) Breit-Wheeler process [9,14], was observed about 1 decade ago in the Stanford Linear Accelerator (SLAC) E-144 experiment [15,16]. There a Compton backscattered photon pulse of about 30 GeV was brought into collision with the 50 GeV SLAC electron beam. The huge gamma factor ($\gamma \approx 10^5$) led to an effective electric field close to the critical one, $E' = \gamma E \approx E_c$, as seen by the electron in its rest frame.

In this context a second parameter comes into play, the "dimensionless laser amplitude," given as the ratio of the electromagnetic energy gained by an electron across a laser wavelength λ to its rest mass,

$$a_0 \equiv \frac{eE\lambda}{mc^2}. \quad (2)$$

This is a purely classical ratio which exceeds unity once the electron's quiver motion in the laser beam has become relativistic. It may be generalized to an explicitly Lorentz and gauge-invariant expression [17]. For our present purposes it is sufficient to adopt a useful rule-of-thumb formula expressing a_0 in terms of laser power [18],

^{*}christopher.harvey@plymouth.ac.uk[†]theinz1@plymouth.ac.uk[‡]antoni@maths.tcd.ie

$$a_0^2 \approx 5 \times 10^3 P[\text{PW}], \quad (3)$$

so that a_0 is of order 10^2 for a laser in the Petawatt class. SLAC E-144, on the other hand, had a_0 of order 1, hence by modern standards was in the low-intensity, high-energy regime. As high energy implies huge gamma factors and fields close to E_c , this is also the genuine quantum regime.

In this paper we will concentrate on the segment of the QED parameter space that has become accessible only recently, characterized by large intensities, $a_0 \gg 1$, and comparatively low energies, $\omega \ll mc^2$, typical for experiments with an all-optical setup. We will thus stay far below the Breit-Wheeler pair-creation threshold and will have to consider a process that is not suppressed by either unfavorable powers or exponentials. A natural process that comes to mind is a crossing image of the Breit-Wheeler one, namely, strong-field Compton scattering where a high-intensity beam of laser photons γ_L collides with an electron beam emitting a photon γ . In this case one has to sum over all n -photon processes of the type

$$e^- + n\gamma_L \rightarrow e^- + \gamma. \quad (4)$$

The study of this process(es) has a history almost as long as that of the laser. Intensity effects were addressed as early as 1963/64 in at least three independent contributions by Nikishov, Ritus, and Narozhnyi [19–22], Brown and Kibble [23], and Goldman [24]. These works are written from a particle physics perspective, i.e., essentially by working out the relevant Feynman diagrams. For modern reviews of these developments, the reader is referred to [15,18]. Nikishov and Ritus in [22] pointed out that a_0^2 is proportional to E^2 and hence the photon density n_γ . The precise relationship is

$$a_0^2 = \frac{\hbar v^2}{m^2 c^2 \omega} n_\gamma = 4\pi\alpha v^2 \lambda^3 n_\gamma, \quad (5)$$

where $v \equiv \hbar\omega/mc^2$ is the dimensionless laser frequency and $\lambda^3 n_\gamma$ is the number of photons in a laser wavelength cubed. As the probability for the process (4) is proportional to $a_0^{2n} \sim n^n$, it becomes *nonlinear* in photon density for $n > 1$ and hence is called *nonlinear Compton scattering* [22]. Somewhat in parallel, the same process has been considered by the laser and plasma physics communities with an emphasis, however, on the very low-energy and hence classical aspects. The appropriate notion is therefore nonlinear *Thomson* scattering. These discussions were based on an analysis of the classical Lorentz-Maxwell equation of motion, typically using a noncovariant formulation and neglecting radiation damping. Some early references are papers by Sengupta [25], Vachaspati [26], and Sarachik and Schappert [27]. Since then there has been an enormously large number of papers from this perspective, many of which are quoted in the concise review [28].

The main intensity effect can indeed be understood classically, the reason being the huge photon numbers involved, $\lambda^3 n_\gamma \approx 10^{18}$, in a laser wavelength cubed. Due to the quiver motion in a (circularly polarized) plane-wave laser field the electron acquires a quasifour momentum given by

$$q = p + \frac{a_0^2 m^2}{2kp} k - p + q_L. \quad (6)$$

Hence, the electron acquires an additional, *intensity-dependent* longitudinal momentum q_L caused by the presence of the laser fields. It may be obtained as the proper time average of the solution $p_\mu(\tau)$ of the classical equation of motion with $p_\mu = p_\mu(0)$ being the initial electron four-momentum and $k_\mu = \omega n_\mu$ the lightlike four-vector of the wave [29]. Historically, Eq. (6) was first found in the context of Volkov's solution [30] of the Dirac equation in a plane electromagnetic wave. Volkov explicitly wrote down the zero component q^0 while the generalization (6) seems to be due to Sengupta (note added at the end of his paper [31]; cf. also the textbook discussion in [32]). Upon squaring q one infers as an immediate consequence the intensity dependent mass shift,

$$m^2 - m_s^2 = m^2(1 + a_0^2). \quad (7)$$

Although first predicted by Sengupta in 1952 [31] (see also [23,29]), it has so far never been observed directly [33]. A central topic of this paper will be to (re)assess the prospects for measuring effects due to the mass shift (7).

The paper is organized as follows. We begin in Sec. II by reviewing the coherent-state model of laser fields, which provides the link between classical laser light and light *quanta* (photons) in quantum theory. We then describe scattering amplitudes between these coherent states in QED and how they are generated by an effective action describing interactions with a classical background field. We illustrate this theory with nonlinear Compton scattering, in Sec. III, and give a thorough discussion of the kinematics of the colliding particles. In Sec. IV we give a variety of predictions for both Lorentz invariant and laboratory-frame photon emission spectra. Our conclusions are presented in Sec. V.

II. QED WITH CLASSICAL BACKGROUND FIELDS

We first address the question which asymptotic in state we should take to describe the laser field. In principle, we would simply take the multiparticle state containing the appropriate number of photons of laser frequency and momentum, encoded in the four-vector $k = (\omega, \mathbf{k})$. We are immediately faced with the problem of not knowing exactly how many photons are in the beam. Similarly, as we do not know how many photons will interact with, say, an electron during an experiment, we do not know what to take for the outstate. To overcome these problems we invoke the correspondence principle: due to the huge photon number in a high-intensity beam it should be feasible to treat the laser *classically* as some fixed background field. Formally, this is achieved by describing the laser beam, asymptotically, in terms of coherent states of radiation [34–37]. The coherent states have the usual exponential form

$$|C\rangle = \exp\left\{-\sqrt{N} \int \frac{d^3k}{(2\pi)^3} C^\mu(k) a_\mu^\dagger(k)\right\} |0\rangle, \quad (8)$$

where a_μ^\dagger is the photon creation operator, $C_\mu(k)$ gives the (normalized) polarization and momentum distribution of the

photons in the beam, and N is the expectation value of the photon number operator (the average number of photons in the beam). As usual, the state is an eigenvector of the positive frequency part of \hat{A}_μ since

$$a_\mu(k)|C\rangle = \sqrt{N}C_\mu(k)|C\rangle. \quad (9)$$

Expanding the exponential in Eq. (8), we see that calculating S -matrix elements between states including coherent pieces is equivalent to a particular weighted sum over S -matrix elements of photon Fock states. Working with coherent states may also be thought of, physically, as neglecting depletion of the laser beam, i.e., taking the number of photons in the beam to remain constant [38,39]. There is a natural connection between classical fields and coherent states as these states are the “most classical” available, having minimal uncertainty. The associated classical field is essentially, as we shall see, the Fourier transform of the distribution function C . To see this we turn to the calculation of S -matrix elements between coherent states.

Consider some scattering processes with an asymptotic state containing the coherent state C and some collections of other particles. For reasons which will shortly become clear, we will summarize all those particles *not* in the coherent state by “in,” so that our state is $|\text{in}; C\rangle$. Similarly, we take an out state of the form $\langle \text{out}; C|$ where we have, in accord with the assumption of no beam depletion, the *same* coherent state. In operator language, we are interested in calculating matrix elements $\langle \text{out}; C|\hat{S}|\text{in}; C\rangle$ of the S -matrix operator

$$\hat{S} := \mathcal{T} \exp \left[-\frac{i}{\hbar} \int_{-\infty}^{\infty} dt \hat{H}(t) \right]. \quad (10)$$

Here $\hat{H}(t)$ is the interaction Hamiltonian (in the interaction picture) and \mathcal{T} denotes time ordering. We now write the coherent state (8) as a translation of the vacuum state (see, e.g., [40]),

$$|C\rangle = \hat{T}_C |0\rangle, \quad (11)$$

where the commutator of the translation operator and the photon annihilation operator is

$$[\hat{a}_\mu(k), \hat{T}_C] = C_\mu(k) \hat{T}_C. \quad (12)$$

Extracting the translation operator from the states,¹ we are left with ordinary asymptotic Fock states but with a modified S -matrix operator

$$\langle \text{out}; C|\hat{S}|\text{in}; C\rangle = \langle \text{out}|\hat{T}_C^{-1} \hat{S} \hat{T}_C|\text{in}\rangle. \quad (13)$$

From the definition (10) of \hat{S} , the effect of the translation operators is to shift any photon operator \hat{A}_μ appearing in the interaction Hamiltonian by (the Fourier transform of) $C_\mu(k)$ which we denote by $\mathcal{A}_\mu(x)$. Hence, the fermions interact with

the full quantum photon field \hat{A}_μ and a classical background field, $\mathcal{A}_\mu(x)$.

To be precise, and switching to a more common quantum field theory language, S -matrix elements are given by the on-shell Fourier transform of Feynman diagrams with amputated external legs, as usual, but where the Feynman diagrams are generated by the action

$$S[A, \mathcal{A}, \psi, \bar{\psi}] = \int d^4x -\frac{1}{4} F_{\mu\nu} F^{\mu\nu} + \bar{\psi} i[\not{\partial} + ie\mathcal{A} + ieA] - m \psi. \quad (14)$$

This is almost the ordinary QED action, but the photon field in the interaction term is shifted by \mathcal{A}_μ , explicitly given by

$$\mathcal{A}_\mu(x) = \sqrt{N} \int d^3k \frac{e^{-ik \cdot x}}{(2\pi)^{3/2} \sqrt{2|k|}} C_\mu(k) + \text{c.c.} \Big|_{k^0=0}. \quad (15)$$

This potential gives the classical electromagnetic fields associated with the momentum distributions $C_\mu(k)$. Note that only the interaction terms of the action are affected by the presence of the background field, following Eq. (13). We therefore have a natural and quite elegant way to calculate—we do not need to directly add up the individual contributions of the infinite series of terms generated by expanding the asymptotic coherent state. Instead, we simply include a classical background in the action which contains all the information about the chosen asymptotic photon distributions. Following [29,41] these results can be summarized by

$$\langle \text{out}; C|\hat{S}|\text{in}; C\rangle = \langle \text{out}|\hat{T}_C^{-1} \hat{S} \hat{T}_C|\text{in}\rangle \langle \text{out}|\hat{S}[A]|\text{in}\rangle, \quad (16)$$

where, on the right-hand side, the asymptotic states are ordinary particle number states, with no coherent pieces, and the photon fields in the S -matrix operator are translated by \mathcal{A}_μ .

Briefly, the same result can be recovered entirely in the path integral, or functional, language, following, e.g., [42]. The construction of S -matrix elements between coherent states proceeds just as for elements between Fock states, but the asymptotic vacuum wave functional must be replaced by coherent-state wave functionals. Ordinarily it is the vacuum which is responsible for introducing the $i\epsilon$ prescription into the action and from there into the field propagators. A coherent state does this and more—it translates the photon field in the interaction terms by the classical field (15), recovering Eq. (16).

Note that the modified action (14) remains quadratic in the fermion field. All effects of the background are therefore contained in a modification of the electron propagator. The result is that, in Feynman diagrams, the propagator becomes “dressed” by the background field \mathcal{A}_μ which surrounds the electrons. The propagator will be represented by a heavy line as in Fig. 1 and has a perturbative expansion in terms of a free-electron propagator interacting an infinite number of times with \mathcal{A}_μ , as represented by the dashed line.

The Feynman rules of the theory are otherwise unchanged from QED—there is a single three-field vertex which joins the photon propagator and two of the dressed fermion propagators. This background-field approach is equivalent to

¹Under the usual assumption of no forward scattering. For the photons, this requires $C_\mu(k')=0$ for any scattered photons of momentum k' .



FIG. 1. Perturbative expansion of the electron propagator in a background field.

adopting a Furry picture [43], in which the “interaction” Hamiltonian describes the quantum interactions while the interaction with the background \mathcal{A}_μ is treated as part of the “free” Hamiltonian.

In general, the fermion propagator will have no closed form expression. Since an intense background will be characterized by numbers larger than 1 (such as the intensity parameter a_0), a perturbative expansion in the background is not suitable. We can of course use a coupling expansion, but this leaves us with an infinite number of Feynman diagrams to calculate for *any* process, even at tree level. Fortunately, for the backgrounds considered in this paper and discussed below, the electron propagator is known exactly, allowing us to treat the background field exactly. We will now illustrate these ideas by applying them to the process of interest in this paper: nonlinear Compton scattering.

III. NONLINEAR COMPTON SCATTERING

In this process an electron, incident upon a laser, scatters a photon out of the beam. Using the background-field approach described above, we use the action (14), which contains the effects of the laser, and take the asymptotic in—and out—states to be, respectively,

$$|p', \lambda\rangle, \quad \langle p', \lambda' : k', \epsilon|. \quad (17)$$

The pair (p, λ) gives the momentum and spin state of the incoming electron, similarly (p', λ') describe the outgoing electron, and (k', ϵ) are the momentum and polarization tensor of the scattered photon. Only one Feynman diagram contributes to this process at tree level, shown in Fig. 2. Note that the analogous scattering amplitude with “naked” electrons, corresponding to spontaneous photon emission in vacuum, vanishes due to momentum conservation.

Calculating the corresponding S -matrix element amounts to amputating the external legs and integrating over the single vertex position. Amputating and Fourier transforming the electron propagator in a background field give us the solutions of the Dirac equation in that background [19,23,24,29]. We will write these electron wave functions as $\Psi_{p\lambda}(x)$. The S -matrix element of the process in Fig. 2 therefore reduces to

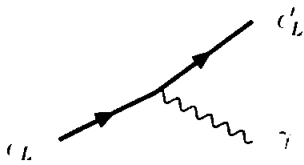


FIG. 2. Nonlinear Compton scattering Feynman diagram using dressed electrons (subscript L).

$$\langle p', \lambda' : k', \epsilon | \hat{S} | \mathcal{A} | p, \lambda \rangle = -ie \int d^4x \bar{\Psi}_{p', \lambda'}(x) \frac{e^{ik'x}}{\sqrt{2|k'|}} \not{\epsilon} \Psi_{p, \lambda}(x). \quad (18)$$

To proceed we need to pick a background field so that we can explicitly calculate the wave functions $\Psi_{p\lambda}(x)$ and therefore the S -matrix element (18). This is the focus of the next section.

A. Plane waves and Volkov electrons

We will model the laser by a plane wave, $\mathcal{A}_\mu \equiv \mathcal{A}_\mu(kx)$, with k a lightlike four-vector characterizing the laser beam direction. The electron wave functions in such a background, or “Volkov electrons [30],” are known exactly. The propagator is also known and may be derived either in field theory or using a first quantized (proper time) method [11]. For a textbook discussion, see [32]. The Volkov electron is

$$\Psi_{p\lambda}(x) = e^{-ipx} \exp \left\{ \frac{1}{2ikp} d\xi 2ep \mathcal{A}(\xi) - e^2 \mathcal{A}^2(\xi) \right\} \times \left[1 + \frac{e}{2kp} \not{k} \mathcal{A} \right] u_p, \quad (19)$$

where $p^2 = m^2$ and u_p is the usual electron spinor.

To better understand this wave function we specialize from here on to the case of \mathcal{A}_μ being a circularly polarized plane wave of amplitude a ,

$$\mathcal{A}^\mu = a_1^\mu \cos(kx) + a_2^\mu \sin(kx), \quad (20)$$

where $a_j k = 0$ and $a_j a_k = -a^2 \delta_{jk}$. The electron wave function becomes

$$\Psi_{p\lambda}(x) = \exp \left[-iqx - ie \frac{a_1 p}{kp} \sin(kx) + ie \frac{a_2 p}{kp} \cos(kx) \right] \dots, \quad (21)$$

We have not given the explicit form of the spinor part; it is easily written down and not needed for the discussion in this section. The important effect is that the electron acquires the quasi-four momentum q defined in Eq. (6) from the laser field with the intensity parameter a_0 given by

$$a_0^2 \equiv \frac{e^2 a^2}{m^2}. \quad (22)$$

Technically, the origin of the quasimomentum lies in a separation of the exponent in Eq. (19) into a Fourier zero mode and oscillatory pieces, with the zero mode causing the momentum shift, $p \rightarrow q$. Inserting the wave functions (21) into Eq. (18) and omitting the details of the calculation [21], we find that the scattering amplitude is a periodic function with Fourier series

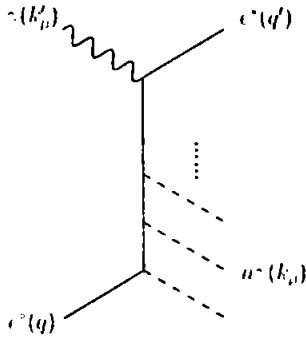


FIG. 3. The effective Feynman diagram describing the n th harmonic process; an electron of mass m_e absorbs n laser photons of momentum k_μ and emits a photon of momentum k'_μ .

$$\begin{aligned} & \langle p', \lambda'; k', \epsilon | \hat{S}[\mathcal{A}] | p, \lambda \rangle \\ &= \frac{1}{(2|k'|2E_q, 2E_q)^{1/2}} \sum_{n=1}^{\infty} M(n) \delta^{(4)}(q + nk - q' - k'). \end{aligned} \quad (23)$$

A discussion of the amplitudes $M(n)$ may be found in [32]. We will give below the explicit form of the squared amplitudes summed over spins λ, λ' , and polarizations ϵ . We do not consider polarized scattering and angular distributions in this paper, though these topics are interesting in themselves and are discussed in, for instance, [44–46].

The sum in Eq. (23) is not a coupling expansion, nor does it appear directly from an expansion of the coherent state into Fock states. Instead, the momentum-conserving delta function in the n th term implies that $M(n)$ can be identified with the amplitude for an electron of momentum q and mass m_e , absorbing n photons of momentum k , and emitting one scattered photon of momentum k' ,

$$e_-(q) + n\chi(k) \rightarrow e_-(q') + \chi(k'), \quad (24)$$

as illustrated in Fig. 3. As pointed out in Sec. I, these multiphoton processes are the origin of the name “nonlinear” Compton scattering. It is simplest to use the language of quasimomenta to formulate the kinematics of Eq. (23) as Eq. (24) is a process involving effective particles. The asymptotic particle kinematics may be reconstructed from the relation (6) between p and q . The processes with $n > 1$ correspond to higher harmonics. Note that the $n = 1$ process is analogous to ordinary, “linear” Compton scattering. It is possible to normalize such that one does indeed recover the Compton cross section at $a_0 = 0$. We will use this below as a reference cross section for experimental signals.

B. Kinematics—forward and backscattering

We will now study the kinematics implied by the momentum conservation in Eq. (23), finding an expression for the emitted photon frequency in terms of incoming particle data which generalizes the standard Compton formula for the photon frequency shift. This will later be used when we predict the emitted photon spectrum.

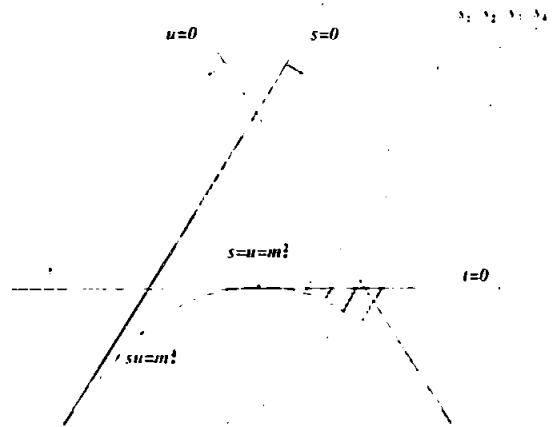


FIG. 4. (Color online) Mandelstam plot for nonlinear Compton scattering. Solid segments of dashed lines correspond to allowed u_n and t_n regions for each depicted value of s_n .

The delta function in Eq. (23) implies the momentum conservation equation

$$q + nk = q' + k', \quad (25)$$

where q is given by Eq. (6) and q' being defined analogously with p replaced by p' . As k is lightlike we have

$$qk = pk, \quad q'k = p'k. \quad (26)$$

It is useful to first discuss the kinematics in terms of the Mandelstam invariants

$$s_n = (q + nk)^2 = m_e^2 + 2nkp \geq m_e^2, \quad (27)$$

$$t_n = (nk - k')^2 = -2nkk' \leq 0, \quad (28)$$

$$u_n = (nk - q')^2 = m_e^2 - 2nkp'. \quad (29)$$

Recall that these are not independent as $s_n + t_n + u_n = 2m_e^2$. As each of them depends on the photon number n they will be different for each of the subprocesses (24). The physically allowed parameter ranges are displayed in the Mandelstam plot of Fig. 4. For the n -photon subprocess, if $s = s_n$ is held fixed, the allowed t and u ranges (highlighted in red/full segments of dashed lines) are

$$\begin{aligned} t_{\min} &= 2m_e^2 - s_n - m_e^4/s_n & u_{\max} &= m_e^4/s_n & \text{backscattering} \\ t_{\max} &= 0 & u_{\min} &= 2m_e^2 - s_n & \text{forward scattering.} \end{aligned} \quad (30)$$

Obviously, the allowed t range increases with photon number n .

In order to find the generalization of Compton’s formula for the scattered photon frequency (thus abandoning manifest covariance) we square Eq. (25) so that we may remove q' from the game via

$$nkq = k'q' = qk' + nkk', \quad (31)$$

where the second equality follows directly from Eq. (25). Using definitions (6) and (26), we trade q for p , arriving at

an equation in terms of the asymptotic, on-shell momenta

$$nk p = k' p + \left(n + a_0^2 \frac{m^2}{2k p} \right) k k'. \quad (32)$$

where $k'^2=0$ and $p^2=m^2$. We will assume, in what follows, that the electron and laser meet in a head-on collision. That is, incident momenta are

$$k^\mu = \omega(1, n), \quad p^\mu = (E_p, -|p|n), \quad |n|=1. \quad (33)$$

Primed (outgoing) quantities are defined analogously. For a head-on collision the only angle in play is the standard scattering angle θ of the photon, determined via $n \cdot n' \equiv \cos \theta$. The remaining scalar products become

$$n \cdot p = -|p|, \quad n' \cdot p = -|p| \cos \theta. \quad (34)$$

From now on we measure all energies in units of the (bare) electron mass, m . This introduces the dimensionless parameters

$$\nu \equiv \frac{\omega}{m}, \quad \gamma \equiv \frac{E_p}{m} \equiv \cosh \zeta, \quad \beta \gamma \equiv \frac{|p|}{m} \equiv \sinh \zeta, \quad (35)$$

where ζ is the rapidity such that

$$\beta \equiv \frac{|p|}{E_p} = \sqrt{1 - 1/\gamma^2} \equiv \tanh \zeta. \quad (36)$$

Of course, β and γ are the usual Lorentz factors characterizing the frame of reference from the electron's point of view. $\beta=0$, for instance, corresponds to the (asymptotic) electron rest frame. Using these definitions, Eq. (32) may be rearranged to express the intensity-dependent scattered photon frequency as

$$\nu'_n(\theta) = \frac{n\nu}{1 + \kappa_n(a_0)e^{-\zeta}(1 - \cos \theta)}. \quad (37)$$

Here, $e^{-\zeta}$ is the (inverse) Doppler shift factor for a head-on collision,

$$e^{-\zeta} = \gamma(1 - \beta) = \sqrt{\frac{1 - \beta}{1 + \beta}}. \quad (38)$$

Going back to Eq. (37) we see that all the intensity dependence resides in the coefficient

$$\kappa_n(a_0) \equiv n\nu - \beta\gamma + a_0^2\gamma(1 - \beta)/2 = n\nu - \sinh \zeta + a_0^2e^{-\zeta}/2. \quad (39)$$

Standard ("linear") Compton scattering is reobtained by setting $n=1$ and $a_0=0$ (no intensity effects). In this case Eqs. (37) and (39) give back the ordinary Compton formula,

$$\begin{aligned} \nu'_1 &= \frac{\nu}{1 + (\nu - \beta\gamma)\gamma(1 - \beta)(1 - \cos \theta)} \\ &= \frac{\nu}{1 + (\nu - \sinh \zeta)e^{-\zeta}(1 - \cos \theta)}. \end{aligned} \quad (40)$$

So, technically speaking, the two intensity effects on the scattered frequency are the replacements (i) $\nu \rightarrow n\nu$ in the numerator and (ii) $\kappa_1(0) \rightarrow \kappa_n(a_0)$ in the denominator. Explicitly, the latter is

$$\nu - \beta\gamma \rightarrow n\nu - \beta\gamma + a_0^2\gamma(1 - \beta)/2, \quad \text{or}$$

$$\nu - \sinh \zeta \rightarrow n\nu - \sinh \zeta + a_0^2e^{-\zeta}/2. \quad (41)$$

The possibility of the incoming electron absorbing $n > 1$ laser photons may be interpreted, in a classical picture, as the generation of the n th harmonic, modulated by both relativistic and intensity effects. Using a linearly polarized beam the first few harmonics have indeed been observed experimentally by analyzing the photon distribution as a function of azimuthal angle, ϕ . The second and third harmonics have clearly been identified from their quadrupole and sextupole radiation patterns [47].

For each harmonic number n , the allowed range of scattered photon frequencies ν'_n is finite. The boundary values of this interval (which is the t interval in the Mandelstam plot Fig. 4) correspond to forward and backscattering at $\theta=0$ and π , respectively,

$$\nu'_n(0) = n\nu, \quad \nu'_n(\pi) = \frac{n\nu}{1 + 2\kappa_n(a_0)e^{-\zeta}}. \quad (42)$$

The assignment of minimum and maximum depends on the sign of κ_n ,

$$\kappa_n > 0 \Rightarrow \nu'_n(\pi) < \nu'_n(\theta) < n\nu$$

redshift "Compton."

$$\kappa_n < 0 \Rightarrow n\nu < \nu'_n(\theta) < \nu'_n(\pi)$$

$$\text{blueshift "inverse Compton."} \quad (43)$$

So, if $\kappa_n > 0$, the allowed scattered photon energies ν'_n are redshifted relative to $n\nu$, the energy of the n absorbed laser photons. This clearly includes the cases $a_0=0$, $\gamma=1$, and $n=1$ which describe Compton's original scattering experiment in the electron rest frame. In accelerator language, this case sees the laser fired onto a fixed electron target: the laser photon transfers energy to the target, so that the scattered photon is redshifted ($\nu' < n\nu$).

On the other hand, if $\kappa_n < 0$, the scattered photon's energy is blueshifted from $n\nu$. The situation when the photon gains energy from the electrons is often referred to as inverse Compton scattering. This is of relevance in astrophysics, for instance, in the Sunyaev-Zeldovich effect [48-50]. A particularly simple and important scenario is provided by the backscattering of the laser pulses, $\theta=\pi$, in the high-energy limit (inverse Compton regime). We take $\gamma \gg 1$ so that $e^\zeta \approx 2\gamma$ and we assume $\kappa_n < 0$, whereupon the scattered frequency becomes, from Eq. (37),

$$\nu'_n(\pi) = \frac{n\nu e^{2\zeta}}{1 + a_0^2 + 2n\nu e^\zeta} \approx \frac{4\gamma^2 n\nu}{1 + a_0^2 + 4\gamma n\nu}, \quad (44)$$

where the approximation is valid for high energy. In this regime one may distinguish between two different limits,

$$\nu'_n(\pi) = 4\gamma^2 n\nu a_0^2 \quad \text{if} \quad 4\gamma n\nu \ll 1 \ll a_0^2, \quad (45)$$

$$\nu'_n(\pi) = \gamma \quad \text{if} \quad 1 + a_0^2 \ll 4\gamma n\nu. \quad (46)$$

It is the former subcase which is typically realized² for optical photons ($\nu \approx 10^{-6}$) and moderate values of harmonic number n . Thus, as long as $a_0 \leq 2\gamma$, the back scattered frequency (45) is (i) blueshifted with respect to the incoming n th harmonic frequency $n\nu$ and (ii) for $n=1$, redshifted compared to the linear “kinematic edge” (the maximal, backscattered frequency, ν'_{\max}) as emphasized already by McDonald [18]. Explicitly, this redshift is

$$4\gamma^2\nu - 4\gamma^2\nu/a_0^2, \quad \gamma \gg 1, \quad 4\gamma n\nu \ll 1 \ll a_0^2. \quad (47)$$

From the definition of κ_n given in Eq. (39) it is clear that, given any fixed experimental setup (i.e., incoming electron energy and intensity parameters ζ and a_0), κ_n will eventually become positive and remain so for all higher harmonics with

$$n > \left\lfloor \frac{\sinh \zeta - a_0^2 e^{-\zeta/2}}{\nu} \right\rfloor \equiv n_0, \quad (48)$$

where $\lfloor b \rfloor$ denotes the nearest integer less than or equal to b . Thus, for a given experimental setup, scattered photons corresponding to harmonic generation with $n > n_0$ can only have energies redshifted relative to the energy $n\nu$ absorbed by the electron. Alternatively, we can fix n and so define a critical intensity, from the vanishing of κ_n , which allows us to tailor the emission spectrum. The critical intensity parameter is

$$\begin{aligned} a_{0,\text{crit}}^2(n) &\equiv 2\gamma(1+\beta)(\beta\gamma - n\nu) \\ &= 2e^\zeta(\sinh \zeta - n\nu) = e^{2\zeta} - 2n\nu e^\zeta - 1 \geq 0. \end{aligned} \quad (49)$$

For $a_0 = a_{0,\text{crit}}(n_0)$ all harmonics with $n > n_0$ ($n < n_0$) will be redshifted (blueshifted). For the extreme choice of $n_0 = 1$, all scattered frequencies will be redshifted for intensities above $a_{0,\text{crit}}(1)$, as in, for example, fixed-target mode ($\gamma = 1$). We are, however, more interested in the colliding mode (high energy). Then, for $\gamma \gg 1$, we can approximate $a_{0,\text{crit}}^2$ from Eq. (49) as

$$a_{0,\text{crit}}^2 \approx 4\gamma^2 - 4\gamma n\nu. \quad (50)$$

When $4\gamma n\nu \ll 1$ as above, $a_{0,\text{crit}}$ becomes effectively n independent

$$a_{0,\text{crit}} \approx e^\zeta \approx 2\gamma. \quad (51)$$

As a numerical example, consider the facility at the Forschungszentrum Dresden-Rossendorf (FZD) with a 100 TW laser and a 40 MeV linac [51]. This implies $\gamma = 80$, $\nu = 2 \times 10^{-6}$, and $a_0 \approx 20$, so that all harmonics are relatively blueshifted up to $n \approx 3.9 \times 10^7$ —as we will see, emission rates at this n are basically zero. In this case, the critical value of a_0 , above which all harmonics ($n \geq 1$) are relatively redshifted compared to $n\nu$, is $a_0 \geq 2\gamma = 160$, 1 order of magnitude above the expected available intensity. One may verify, for example, that for $a_0 = 200$, $\kappa_n > 0$ for all n .

The discussion above will be illustrated in the next section when we discuss the photon spectra as a function of

scattered frequency, ν' . In particular, we will see that, even if backscattering does not necessarily maximize the scattered photon frequency, it nevertheless gives us the strongest signal for which to search experimentally, namely, the redshift of the Compton edge (parameters permitting).

To better understand the different behaviors of the harmonics, it is useful to write κ_n in terms of laboratory-frame variables. For a head-on collision (which we assume), say along the z axis, all momenta involved are longitudinal. The total three-momentum, call it P , is then given by

$$\begin{aligned} P &\equiv nk + q = nk + p + q_L \\ &= m(n\nu - \sinh \zeta + a_0^2 e^{-\zeta/2})\hat{z} = m\kappa_n \hat{z}. \end{aligned} \quad (52)$$

The lab-frame physics involved in a head-on collision ($p = -(\beta\gamma\nu)k$) depends crucially on the relative magnitude of the three terms contained in κ_n ,

$$n|k|/m = n\nu, \quad (53)$$

$$|p|/m = \sinh \zeta. \quad (54)$$

$$|q_L|/m = a_0^2 e^{-\zeta/2}. \quad (55)$$

Consider again Compton's original experiment with an electron at rest and $a_0 = 0$. This corresponds to $q_L = p = 0$, so the only three-momentum is that of the single incoming photon which delivers part of its energy to the electron and hence is redshifted. If we now increase the electron energy in the laboratory (using a standard or wake field acceleration scheme) this redshift turns into a blueshift ($\nu' > \nu$) as soon as $|p| > |k| = m\nu$. This happens exactly where the total momentum, $P = k + p$, changes direction from pointing in direction k to $-k$. Hence, at this particular point P passes through zero, which, of course, defines the center-of-mass (c.m.) frame where there is no frequency shift at all, $\nu' = \nu$.

If we now turn on intensity ($a_0 > 0$) the total momentum acquires an additional, laser-induced contribution q_L along k . So, in fixed-target mode large intensity will result in a significant enhancement of the Compton redshift. If, on the other hand, we assume colliding mode with a blueshift at $a_0 = 0$, then the q_L contribution in P works against the “influence” of p . As a result, the blueshift $\nu' > \nu$ at zero intensity is reduced, resulting in a redshift of the kinematical Compton edge (ν'_{\max}). If a_0 is large enough this latter redshift may completely cancel the inverse Compton blueshift. Again, this happens when the total momentum $P = k + p + q_L$ vanishes ($\kappa_1 = 0$), i.e., in the “c.m. frame” which is now an intensity-dependent notion as q_L depends on a_0 .

If we finally allow for higher harmonics $n > 1$, with the total momentum becoming $P = nk + p + q_L$, we can balance p by increasing a_0 , n , or both. The transition point, $\kappa_n = 0$, defines a c.m. frame for the n th process. At this point, the range of the n th allowed harmonic collapses to a point, $\nu'_n(\theta) = n\nu$, as the θ dependence in Eq. (37) drops out. Strictly speaking, this can only occur for at most one value of n , but neighboring n 's will still have rather small spectral ranges (see Fig. 9).

²SLAC E-144 had $\gamma\nu = O(1)$ so all terms in the denominator of Eq. (44) were of comparable magnitude.

IV. PHOTON EMISSION RATES

A. Lorentz invariant characterization

The S -matrix element represented by the Feynman diagram of Fig. 2 and given implicitly in Eq. (23) may readily be translated into an emission rate [19,32]. The nontrivial contribution to the differential rate for emitting a photon of frequency $\omega' = m\nu'$ per unit volume per unit time, in the n th harmonic process, i.e., the process (24), comes from the differential probability³ [32]

$$\frac{dW_n}{dx} = \frac{1}{(1+x)^2} \mathfrak{J}_n(z(x)), \quad n \geq 1, \quad (56)$$

where x is the dimensionless Lorentz invariant

$$x \equiv \frac{kk'}{kp'} = \frac{t_n}{u_n - m_e^2} \geq 0. \quad (57)$$

The kinematically allowed range for n th harmonic generation is given by the interval

$$0 \leq x \leq y_n, \quad (58)$$

$$y_n \equiv \frac{2nkp}{m_e^2} = \frac{s_n}{m_e^2} - 1 \geq 0, \quad (59)$$

which corresponds to the t range given in Eq. (30) highlighted in Fig. 4. The end points $x=y_n$ are located on the hyperbola $su=m_e^2$. For x outside of this range the n th partial rate vanishes.

The function \mathfrak{J}_n is

$$\mathfrak{J}_n(z) \equiv -\frac{4}{a_0^2} J_n^2(z) + \left(2 + \frac{x^2}{1+x}\right) [J_{n-1}^2(z) + J_{n+1}^2(z) - 2J_n^2(z)], \quad (60)$$

where J_n being Bessel functions of the first kind. Their argument is another Lorentz invariant

$$z(x) \equiv \frac{2a_0}{y_1} \sqrt{\frac{x(y_n - x)}{1 + a_0^2}}. \quad (61)$$

Both upper and lower limits of x correspond to $z=0$ and hence zeros of $\mathfrak{J}_n(z)$ for all $n > 1$. The first few partial emission rates for $E_p=50$ MeV, $\omega=1$ eV (hence $\gamma=10^2$, $\nu=2 \times 10^{-6}$), and $a_0=20$ are plotted in Fig. 5. Linear Compton ($a_0=0$ and $n=1$) data are presented for comparison.

The figure clearly shows the appearance of higher harmonics ($n > 1$) with, however, a reduced signal strength as compared to the fundamental frequency. Writing the Compton edge (59) as

$$y_n = y_n(a_0) = y_1(0) \frac{n}{1 + a_0^2}, \quad (62)$$

where $y_1(0)$ corresponds to linear Compton scattering, we see that the edge $x=y_1(a_0)$ of the first harmonic will always

³We normalize such that we recover the Klein-Nishina cross section for linear Compton scattering for $n=1$ as $a_0 \rightarrow 0$ (see, e.g., [32]).

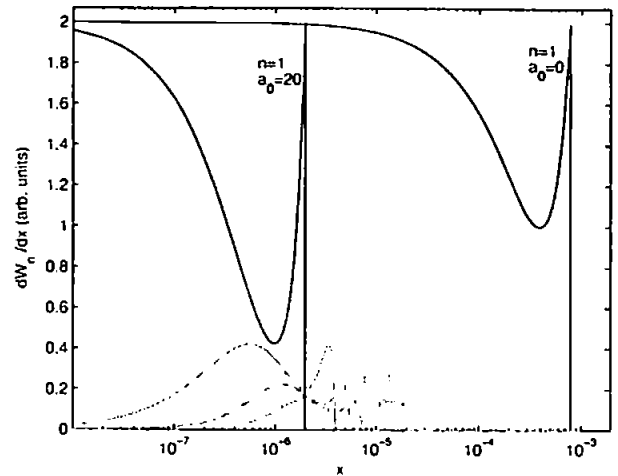


FIG. 5. (Color online) Partial emission rates ($n=1 \dots 4$) for non-linear Compton scattering as a function of the Lorentz invariant x at intensity $a_0=20$ compared to linear Compton scattering ($a_0=0$ curve). Horizontal log scale.

be shifted to the left by a factor $1/(1+a_0^2)$. The same is true for the higher harmonics until $n > 1 + a_0^2$. For $a_0 \gg 1$ these large harmonics will, however, be invisible due to their very small signal strength.

To obtain the total rate, one just sums over photon numbers n , i.e., over all harmonics.

$$\frac{dW}{dx} = \sum_{n=1}^{\infty} \frac{dW_n}{dx}, \quad (63)$$

where it is understood that the n th term is supported on $0 \leq x \leq y_n$, with x given in Eq. (57). The partial sums up to $n=30, 60$, and 100 are shown in Fig. 6, along with the linear Compton spectrum. Again we note the significant shift of the fundamental Compton edge at $x=y_1(a_0)$ together with side maxima due to the higher harmonics. Interestingly, the fundamental ($n=1$) signal gets amplified due to superposition of the higher harmonic rates from Fig. 5. This suggests that, for $a_0 > 1$, the signal-to-noise ratio may become larger than for the linear case, while the full width at half maximum may become smaller. By tuning a_0 to an optimal value one may thus design x rays of a given frequency and width.

B. Laboratory kinematics: Energy dependence

Any actual Compton scattering experiment will be performed in a laboratory (frame) with the electrons either at rest (fixed target mode) or in motion. In what follows, we will assume the latter together with a head-on collision between laser pulse and electron beam (collider mode) as discussed in the previous section. In this case the kinematic invariants x and y_n from Eqs. (57) and (59) become functions of the scattered frequency ν' and the scattering angle θ .

$$x = \frac{(1 - \cos \theta) \nu'}{e^{\xi} - (1 - \cos \theta) \nu'}, \quad (64)$$

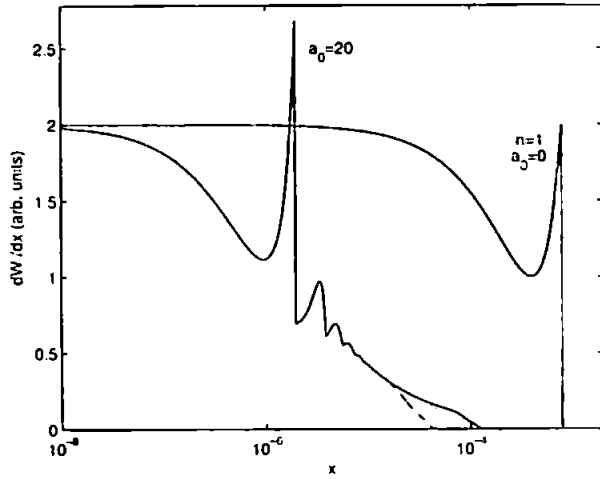


FIG. 6. (Color online) Sum of partial emission rates from $n = 1 \dots 30$ (dashed, lower curve), 60 (dotted, middle curve), and 100 (solid (black), top curve) for nonlinear Compton scattering (head-on collision) at intensity $a_0=20$. The curves are indistinguishable for $x \lesssim 10^{-5}$. Linear Compton data (blue, $n=1$, $a_0=0$) added for comparison.

$$\gamma_n = \frac{2n\nu e^2}{1 + a_0^2}. \quad (65)$$

Either the scattering angle θ or the frequency ν'_n may be eliminated via Eq. (37), allowing us to plot the emission rate as a function of ν' or θ , respectively.⁴ In this section we focus on the ν' dependence of the partial and total emission rates which are depicted in Figs. 7 and 8, respectively. Similar plots (for a_0 of order 1) have been obtained before in [16,18,44,46].

Analytically the partial rates are

$$\frac{dW_n}{d\nu'} = \frac{dW_n}{dx} \frac{dx}{d\nu'} = -\frac{\Im_n(z)}{\kappa_n}. \quad (66)$$

The allowed range for ν' is given in Eqs. (42) and (43). The argument z defined in Eq. (61) becomes a function of ν' via its dependence on

$$x \equiv x_n(\nu') = \frac{n\nu - \nu'}{\kappa_n - n\nu + \nu'} \quad (67)$$

upon eliminating θ from Eq. (64) via Eq. (37).

For the parameters chosen ($\gamma=10^2$, $\nu=2 \times 10^{-6}$, and $a_0=20$) Figs. 7 and 8 are fairly similar to their invariant pendants, Figs. 5 and 6. In particular, the previous shift in x now corresponds to a redshift of the linear Compton edge by a factor of $1+a_0^2 \approx 400$ from about 40 to 0.1 keV, i.e., from the hard to the soft x-ray regime. Note that the frequency range is still blueshifted relative to the incoming frequency ν (corresponding to the left-hand edge in Figs. 7 and 8 given by

⁴The relationship between angle and frequency spectrum (37) is invertible provided $\kappa_n \neq 0$. For $\kappa_n=0$ the n th harmonic spectral range shrinks to a point (see below).

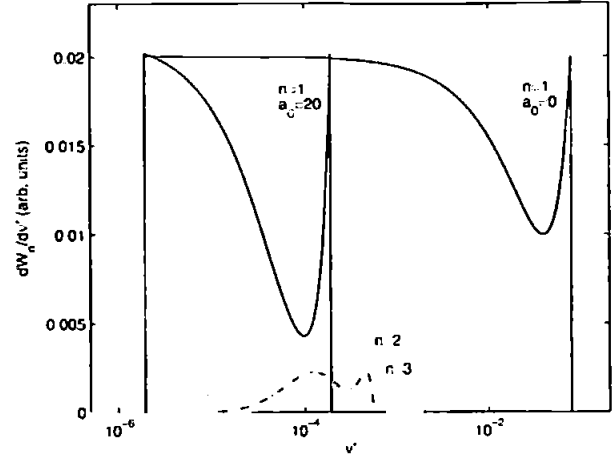


FIG. 7. (Color online) Individual harmonic spectra ($n=1 \dots 4$) for nonlinear Compton scattering at intensity $a_0=20$ compared to linear Compton scattering ($n=1$, $a_0=0$) as a function of ν' .

$\nu=2 \times 10^{-6}$). Again, there is a noticeable enhancement of the total emission rate at $\nu'_n(\pi) \approx 4\gamma^2\nu/a_0^2$ [cf. Eq. (45)] due to the generation of peaks corresponding to higher harmonics, $n > 1$, with the peak values decreasing rapidly with n . We note that the edge values of the higher harmonics which are clearly visible in Fig. 7 get washed out by the superposition of more and more partial rates dW_n in Fig. 8. This will reduce the visibility of the associated maxima, as will, of course, all sorts of background effects which have not been included in the theoretical analysis above.

The properties of the photon spectrum depend crucially on electron parameters (β , γ , or ξ) characterizing the laboratory frame and, in particular, the intensity parameter a_0 . To illustrate this dependence along with the discussion of Sec. III B, we have calculated the photon spectra as a function of a_0 , ranging from $a_0=20$ up to 300. The outcome is depicted in the movielike sequence of plots of Fig. 9. As $\gamma=100$ the

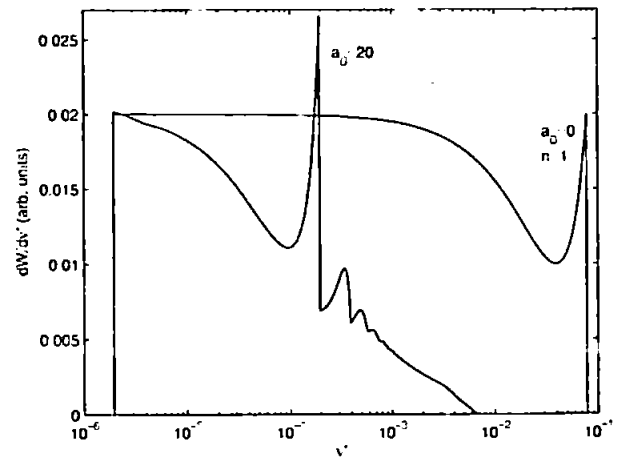


FIG. 8. (Color online) Theoretical photon spectrum (sum of first 50 harmonics) for nonlinear Compton scattering at intensity $a_0=20$ compared to linear Compton scattering ($n=1$, $a_0=0$) as a function of ν' .

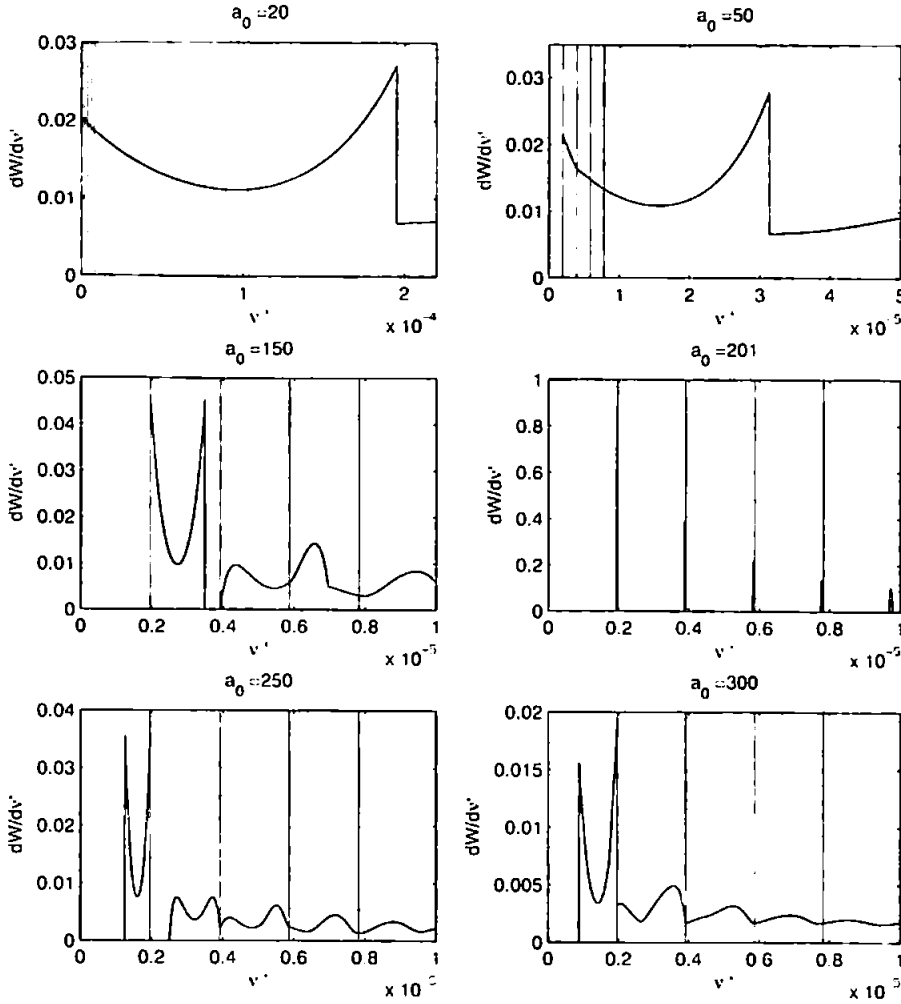


FIG. 9. (Color online) Theoretical photon spectra for nonlinear Compton scattering for different values of a_0 ($\gamma=100$) and incoming frequency $\nu=2 \times 10^{-6}$ (arb. units). Vertical (red) lines correspond to frequencies $n\nu$.

critical a_0 from Eq. (49) defining the c.m. frame of the first harmonic is $a_{0\text{cm}}(1) \approx 200$ corresponding to the fourth plot in Fig. 9. There, the lower harmonic spectrum collapses to lines located at the individual harmonics with frequencies $\nu'_n = n\nu$ (marked by red vertical lines throughout).

If we go through the whole sequence the following picture emerges. For small $a_0 < a_{0\text{cm}}(n)$, all harmonic ranges with counting label less than n are blueshifted. Plots 1 and 2 show the harmonic range for $n=1$ (and part of $n=2$), both to the right of their red end edges (ν and 2ν , respectively). The right-hand, blue end, maximum of the fundamental range is enhanced due to contributions of higher harmonics. For a_0 approaching its critical value the harmonic ranges shrink and a gap between the first and second appears (plot 3) so that the fundamental maxima become of equal height. At $a_0 = a_{0\text{cm}}(1) \approx 200$ the first harmonic range shrinks (almost) to a point, with the neighboring ranges also becoming very narrow (plot 4). Once $a_0(1)$ becomes supercritical, all harmonic ranges are redshifted [i.e., located to the left of the vertical (red) lines, $\nu'_n < n\nu$], with the ranges increasing again and gaps closing (plots 5 and 6). In plot 6, the first and second harmonics overlap again, leading to maxima of different height with the one at $\nu'_1 = \nu$ being the larger. Thus, by tuning

a_0 we effectively change frames of references with $a_{0\text{cm}}(1)$ representing the border between inverse Compton scattering (blueshift) and Compton scattering (redshift).

C. Laboratory kinematics: Angular dependence

As mentioned earlier, the emission rates may be considered as functions of either scattered frequency ν'_n or scattering angle θ —the two being related via Eq. (37). In terms of the scattering angle θ the rates become

$$\frac{dW_n}{d\Omega} = \frac{dW_n}{dx} \frac{dx}{d\Omega} = \frac{e^{\xi}}{n\nu(1 - \cos \theta)^2} \frac{x_n^2}{(1 + x_n)^2} \mathcal{J}_n(z_n),$$

$$0 < \theta < \pi, \quad (68)$$

where $x_n \equiv x$ (for the n th harmonic) and z_n are to be viewed as functions of θ (see below). Our angular measure is $d\Omega \simeq d\theta \sin \theta$, which is the solid angle measure up to a factor of 2π , as the azimuthal angle ϕ does not contribute due to axial symmetry. Note that this is different for linear polarization or, more generally, if there is another preferred direction which, for instance, could be induced by noncommutative geometry [52].

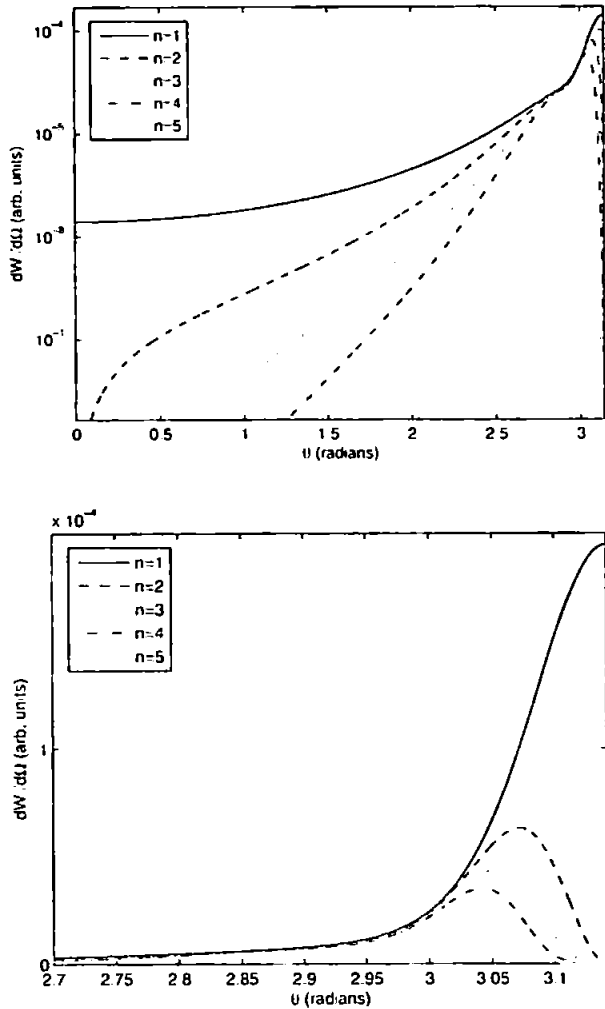


FIG. 10. Theoretical photon spectrum for the first five individual harmonics as a function of scattering angle θ . Parameters: $\gamma=100$, $a_0=20$. Left: vertical scale logarithmic; Right: vertical scale linear, zoomed into range $2.7 < \theta < \pi$.

In terms of their angular dependence the various invariants may all be expressed, using Eqs. (37) and (57), in terms of the variable x_1 defined by

$$x_n(\theta) \equiv nx_1(\theta) = \frac{2nr(1 - \cos \theta)}{e^\xi(1 + \cos \theta) + e^{-\xi}(1 + a_0^2)(1 - \cos \theta)}, \quad (69)$$

with x_1 between $x_1(0)=0$ and $x_1(\pi)=y_1$ as in Eq. (59), where

$$y_1 = \frac{2\nu e^\xi}{1 + a_0^2}. \quad (70)$$

The argument of \mathfrak{J}_n in Eq. (68) becomes

$$z_n(\theta) = nz_1(\theta) = 2n \frac{a_0}{\sqrt{1 + a_0^2}} \sqrt{r(1 - r)}. \quad (71)$$

where we have introduced the rescaled variable

$$r \equiv x_1/y_1 = \frac{e^{-\xi}(1 + a_0^2)(1 - \cos \theta)}{e^\xi(1 + \cos \theta) + e^{-\xi}(1 + a_0^2)(1 - \cos \theta)}, \quad (72)$$

$$0 \leq r \leq 1. \quad (72)$$

As a result, z_1 becomes maximal for $r=1/2$ and so z_1 is less than unity,

$$z_1 \leq \frac{a_0}{\sqrt{1 + a_0^2}} < 1, \quad (73)$$

which will be important later when we discuss the convergence of the emission rate sum. Solving $r(\theta_0)=1/2$ we find that z_1 is maximized at the angle

$$\theta_0 = \arccos \frac{1 + a_0^2 - e^{2\xi}}{1 + a_0^2 + e^{2\xi}}. \quad (74)$$

We will now relate these results to the emission spectra as functions of θ . In Fig. 10 we show the angular distribution of the photon yield, as determined by Eq. (68), for the lowest individual harmonics, $n=1, \dots, 5$. For the parameters chosen ($\gamma=10^2$, $\nu=2 \times 10^{-6}$, and $a_0=20$) the largest signal is due to the fundamental harmonic, $n=1$. This is also the only one contributing on axis, i.e., in the forward and backward directions, $\theta=0$ and π , respectively. For the classical intensity distribution this was also found by Sarachik and Schappert [27]. Thus, in particular, real backscattering at $\theta=\pi$ only occurs for $n=1$, while for the higher harmonics one has "dead cones" with an opening angle of about 0.1 rad, slightly increasing with harmonic number n , as seen from the magnified plot in Fig. 10 (right panel).

The dead cones are controlled by the angle θ_0 from Eq. (74): their opening angles are bounded by $\theta'_0 \equiv \theta_0 - \pi$. For $1 \ll a_0^2 \ll \gamma^2$ the former are quite narrow such that most of the radiation (in particular the location of the maxima at θ_0) is near backward.⁵ Quantitatively one finds that the dead cone opening angles are less than

$$\theta'_0 \approx a_0/\gamma \ll 1, \quad (75)$$

which, for the parameters of Fig. 10, corresponds to $\theta'_0 \approx 0.2$ rad. (For the intensity distribution of classical radiation the relation (75) was found in [45].)

To determine the total emission rate we have to sum Eq. (68) over all harmonic numbers, n . It is not entirely obvious that the ensuing series converges. To prove this we employ the Bessel function identity [53],

$$J_{n-1}(z) = \frac{n}{z} J_n(z) - J'_n(z), \quad (76)$$

where the prime denoting the derivative with respect to the argument z in order to rewrite \mathfrak{J} in terms of J_n^2 and $J'_n{}^2$,

⁵We mention in passing that the situation for linear polarization is different. As pointed out by Esarey *et al.* [45] for Thomson scattering with linearly polarized photons, *odd* harmonics do get backscattered (no dead cones).

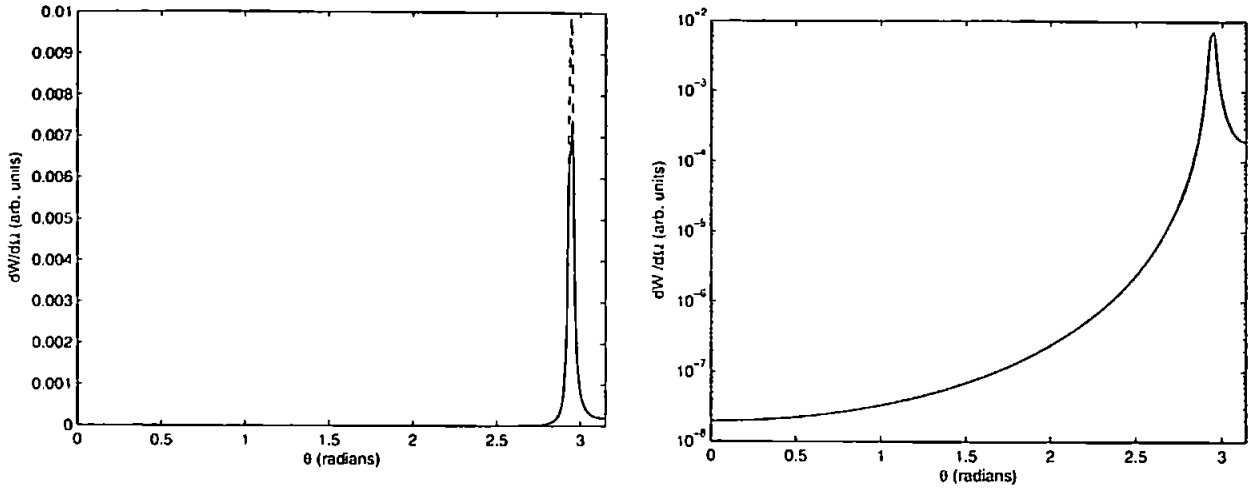


FIG. 11. Theoretical photon spectrum. Parameters: $\gamma=100$, $a_0=20$. Left: vertical scale linear, harmonics summed up to $n=5000$ (full line) and $n=10\,000$ (dashed line). Right: vertical scale logarithmic, harmonics summed up to $n=5000$.

$$\begin{aligned} \mathfrak{J}(z_n) = & 2J_n^2(nz_1) \left[-\frac{2}{a_0^2} + \left(2 + \frac{n^2 x_1^2}{1+n x_1} \right) \left(\frac{1}{z_1^2} - 1 \right) \right] \\ & + 2J_n'^2(nz_1) \left(2 + \frac{n^2 x_1^2}{1+n x_1} \right). \end{aligned} \quad (77)$$

According to Eq. (68), in the rates this is multiplied with an n -dependent factor $n/(1+n x_1)^2$. Thus, upon summation, we encounter series of the form

$$\sum_{n>0} \frac{n^N}{(1+n x_1)^M} J_n^2(nz_1) \quad \text{and} \quad \sum_{n>0} \frac{n^N}{(1+n x_1)^M} J_n'^2(nz_1), \quad (78)$$

where $N \in \{1, 3\}$ and $M \in \{2, 3\}$. We can easily bind these series from above, for example,

$$\sum_{n>0} \frac{n}{(1+n x_1)^2} J_n^2(nz_1) < \sum_{n>0} n J_n^2(nz_1) \equiv S_1, \quad (79)$$

$$\sum_{n>0} \frac{n^3}{(1+n x_1)^3} J_n^2(nz_1) < \sum_{n>0} n^3 J_n^2(nz_1) \equiv S_3, \quad (80)$$

(and likewise for $J_n'^2$). The series S_1 and S_3 on the right-hand side are examples of Kapteyn series [54] which are known to converge. Remarkably, some also have analytic expressions for the sum. These results do not seem particularly common, so we collect them in the Appendix. Although we have not yet been able to explicitly perform our sums (which have a more complicated n dependence than the Kapteyn series) we can now be confident that they converge. This is an extremely satisfying result confirming the validity of the background field picture we have employed and our analysis based around the summation of individual harmonics.

Lerche and Tautz [55] stated that a summation of the first 1000 terms in Kapteyn series such as Eq. (79) or (80) yields errors below 10^{-6} for $z_1 \leq 0.95$. We need to include z_1 values closer to one where the convergence rate is at its lowest. This

occurs near the angle θ_0 defined in Eq. (74). Increasing the maximum harmonic number from 5000 to 10 000 yields basically identical plots except that the height of the narrow peak at θ_0 increases as shown in Fig. 11 (left panel). The maximum is indeed located at $\theta = \theta_0 = 2.94$ (or $\theta_0' = a_0/\gamma \approx 0.2$) as given in Eqs. (74) and (75). The shoulder near $\theta = \pi$ ($\theta' = 0$) is entirely due to the fundamental harmonic ($n = 1$).

Finally, we again vary a_0 and plot a movie of the angular distribution for fixed $\gamma=100$ in Fig. 12. The main features are (i) a propagation of the main peak from near-backward direction (when $a_0 \leq 2\gamma$) to near-forward direction (when $a_0 \geq 2\gamma$) consistent with the formula (74) for θ_0 and (ii) the appearance of a double peak which (iii) becomes symmetric for $a_0 = 2\gamma$ at an angle $\theta_0 = \pi/2$. The latter situation corresponds to $\cos \theta_0 = 0$, hence,

$$a_0^2 = e^{2\xi} - 1 = e^{2\xi} \approx 4\gamma^2, \quad (1 \ll a_0^2 \ll \gamma^2). \quad (81)$$

This latter value (approximately) coincides with the critical a_0 of Eq. (51). The locations of the two peaks in the spectrum are plotted in Fig. 13, along with the angle θ_0 given in Eq. (74) as a function of a_0 . It is clear from this plot that the maximum value of z_1 corresponds to the local minimum between the two peaks.

D. Thomson limit: Emission rate and intensity

At this point one should mention that thorough discussions of the intensity distributions employing *classical* radiation theory have appeared before [27,45]. It is useful to check that our quantum calculations based on the Feynman diagrams of Fig. 3 describing nonlinear Compton scattering reproduce the results for nonlinear *Thomson* scattering in the classical limit. According to Nikishov and Ritus [19] the classical limit is given by

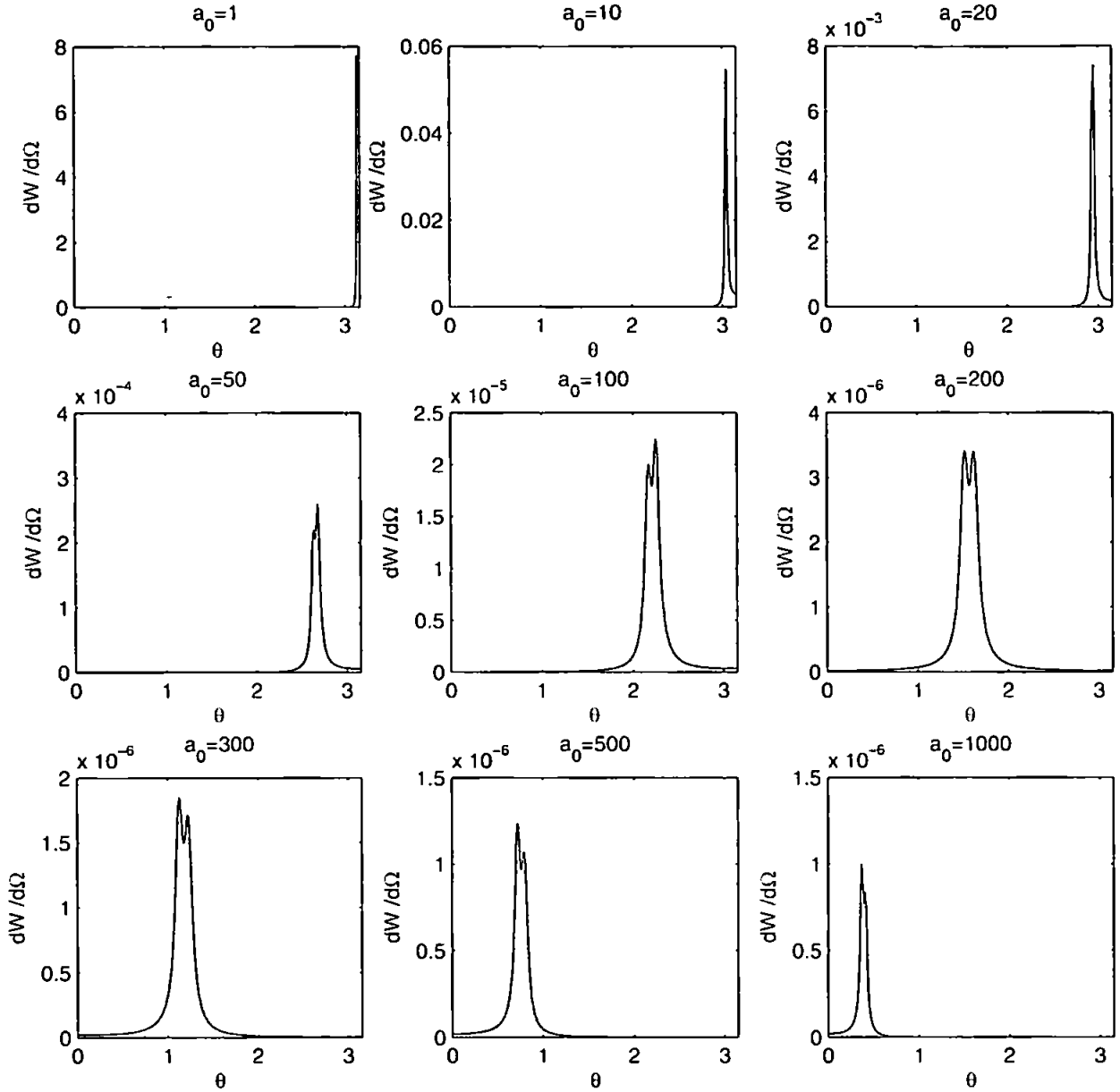


FIG. 12. Theoretical photon spectrum as a function of θ , harmonics summed up to $n=5000$ for different values of a_0 ($\gamma=100$); vertical scale linear (arb. units).

$$y_n = \frac{2npk}{m_*^2} \ll 1. \quad (82)$$

$$x_n \ll 1. \quad (83)$$

which is just the statement that m_* is the dominant energy scale. Note that this can be achieved by having large a_0 and may be counterbalanced by large n . Hence, harmonics with sufficiently large harmonic number n will behave nonclassically (if they are observable at all despite their suppression). As y_n is the upper bound for x_n , Eq. (82) may equivalently be formulated as

such that we may neglect $x_n = nx_1$ on the left-hand sides of Eqs. (79) and (80) which hence *coincide* with S_1 and S_3 in the classical limit. Even if Eqs. (83) no longer holds (i.e., for large n), contributions to the sum are still suppressed by J_n^2 . Comparing the quantum and classical (Compton vs Thomson) rates by evaluating all sums numerically, the graphs are indistinguishable. Plotting the relative difference for our parameter values one finds a small discrepancy near $\theta = \theta_0$ of the order of 1% (see Fig. 14). Note that the classical series S_1

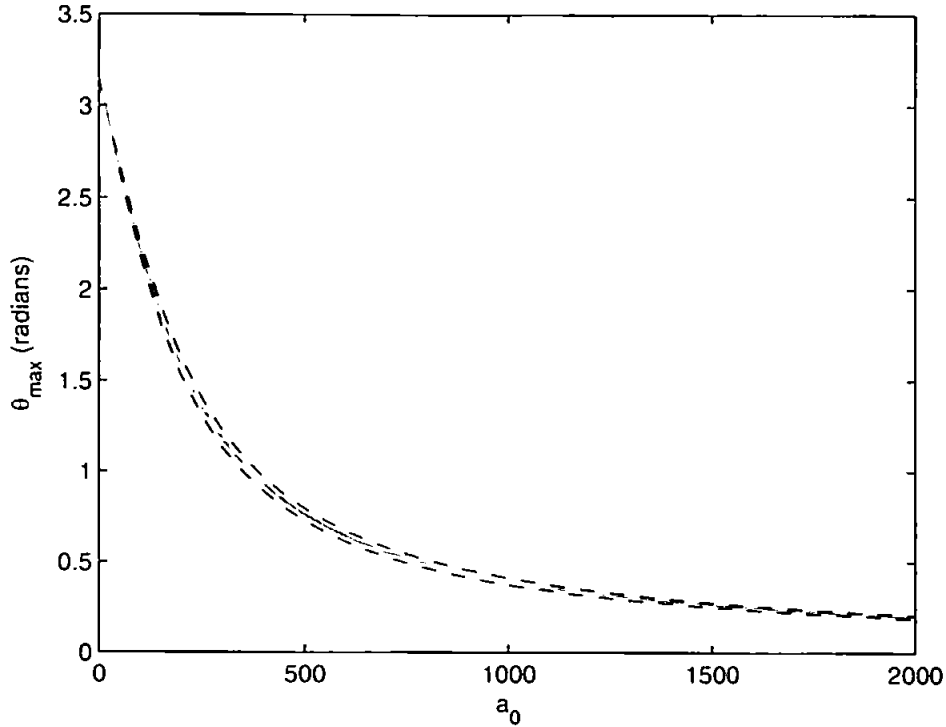


FIG. 13. The angular position of the maximum emission rates as a function of intensity, $a_0 \geq 1$ (dashed/upper and lower curves), and the angle θ_0 which defines the maximum value of z_1 (solid gray/middle curve). Harmonics summed up to $n=5000$. $\gamma=100$.

and S_3 have a slightly slower rate of convergence (in particular near $z_1=1$, i.e., $\theta=\theta_0$), where the suppression is mainly provided by $J_n^2(nz_1)$, hence least efficient at $z_1=1$. We have found, for instance, that the peak in Fig. 14 increases from 0.4% to 0.7% when we increase the maximum n from 5000 to 10 000. Nevertheless, Fig. 14 provides a nice confirmation that for high-intensity optical lasers the background can indeed be treated as classical to a very good approximation.

We are left with relating photon production probabilities dW_n to intensities dl_n . This problem has also been addressed by Nikishov and Ritus [19] who stated that the intensity is given by the zero component of the radiation four-vector,

$$P_\mu = \sum_{n=0} \int dW_n k'_\mu. \tag{84}$$

We thus have $dl_n = m\nu' dW_n$ or

$$\frac{dl_n}{d\theta} = me^2 \epsilon \frac{\nu^2}{\sin^2 \theta} \frac{z_1^3}{a_0^3} \frac{n^2}{(1+nz_1)^3} \mathfrak{J}_n(nz_1). \tag{85}$$

Compared to Eq. (68) we thus have an additional factor $n/(1+nz_1)$. In the classical limit, $nz_1 \ll 1$, this is just n so that Eq. (85) is bounded not by the Kapteyn series S_1 and S_3 , but by the analytically known series S_2 and S_4 as given in the Appendix.

V. CONCLUSIONS

In this paper we have (re)assessed the prospects for observing intensity effects in Compton scattering. The physical

scenario assumed is the collision of a high-intensity laser beam with an electron beam of sufficiently high energy ($\gamma \gtrsim 10^2$) produced in a conventional accelerator or by a suitable laser plasma acceleration mechanism. In technical terms we were interested in the features present in cross sections or photon emission rates which are enhanced with increasing dimensionless laser amplitude, $a_0 = ea/m$, where a is the magnitude of the laser vector potential. The possible effects are of a mostly classical nature, being fundamentally due to the mass shift, $m^2 - m_e^2 = m^2(1+a_0^2)$, caused by the relativistic quiver motion of an electron in a laser field. Ranked in order of their relevance the main intensity effects are (i) a redshift of the kinematic Compton edge for the fundamental harmonic $\omega' = 4\gamma^2\omega \rightarrow 4\gamma^2\omega/a_0^2$ for the parameters we have used, (ii) the appearance of higher harmonic peaks ($n > 1$) in the photon spectra, and (iii) a possible transition from inverse Compton scattering ($\omega' > \omega$) to Compton scattering ($\omega' < \omega$) upon tuning a_0 . The redshift (i) may be explained in terms of the larger effective electron mass, $m_e > m$, the generation of which costs energy that is missing when it comes to “boosting” the photons to higher frequencies. This has, for instance, an impact on x-ray generation via Compton back-scattering. To avoid significant energy losses (reducing the x-ray frequency) the amplitude a_0 should probably not exceed unity significantly. However, one is certainly dealing with a fine-tuning problem here, as item (ii), the generation of higher harmonics, improves the x-ray beam energy distribution. For $a_0 > 1$ there is a larger photon yield due to superposition of the harmonics and the full width at half maximum goes down. As a result, the x rays tend to become more

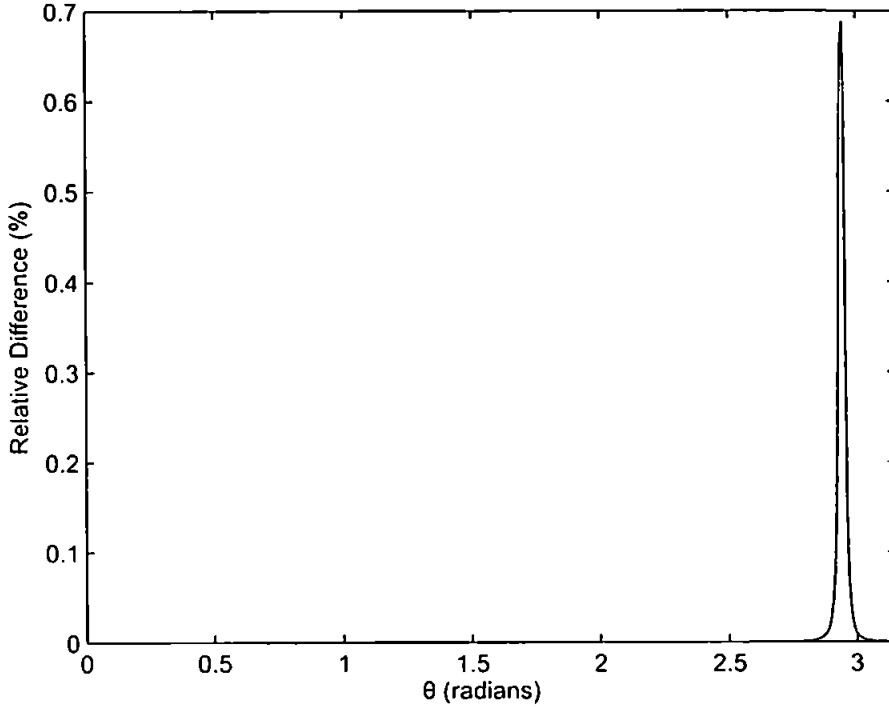


FIG. 14. (Color online) Relative difference of photon emission rates [Compton–Thomson]/Compton as a function of scattering angle θ . Harmonics summed up to $n=10\,000$. $\gamma=100$, $a_0=20$.

monochromatic once higher harmonics become involved. Item (iii), the transition from inverse to ordinary Compton scattering, once a_0 increases beyond 2γ illustrates the energy “loss” just mentioned. When $a_0 \approx 2\gamma$ the laboratory frame can be interpreted as an intensity-dependent center-of-mass frame for which $\omega'_n = n\omega$, at least for low harmonics. Thus there is no longer an energy gain of the emitted photons: the laser beam has become so “stiff” that, in this frame, electrons begin to bounce back from it (gaining energy) rather than vice versa.

The next step is to actually perform the experiments required for measuring the effects listed above. We emphasize that nonlinear Compton scattering provides a unique testing ground for strong-field QED as the process is not suppressed in terms of α or E/E_c by powers or exponentially. Hence, the experiments at Daresbury ($\gamma \approx 50$, $a_0 \approx 2$) [56] and the FZD ($\gamma \approx 80$, $a_0 \approx 20$) planned for the near future should indeed be able to see the effects analyzed in this paper. This will provide crucial evidence for the validity of the approach to strong-field QED adopted here, based on the electron mass shift, the Volkov solution, and the Furry picture.

ACKNOWLEDGMENTS

The authors thank F. Amiranoff, M. Downer, G. Dunne, H. Gies, B. Kämpfer, K. Langfeld, M. Lavelle, K. Ledingham, M. Marklund, D. McMullan, G. Priebe, R. Sauerbrey, G. Schramm, D. Seipt, V. Serbo, and A. Wipf for discussions on various aspects of strong-field QED. A.I. acknowledges

support from IRCSET and C.H. from EPSRC. A.I. thanks the Plymouth Particle Theory Group for hospitality.

APPENDIX: KAPTEYN SERIES

The Kapteyn series [54] (see also [57]) of the second kind involve squares of Bessel functions or their derivatives. We use the notation

$$S_N \equiv \sum_{n>0} n^N J_n^2(nz_1), \quad (\text{A1})$$

$$S'_N \equiv \sum_{n>0} n^N J_n'^2(nz_1), \quad (\text{A2})$$

where $0 < z_1 < 1$ in keeping with our earlier discussion. The sums with a closed-form expression are

$$S_{-2} \equiv \sum_{n>0} n^{-2} J_n^2(nz_1) = \frac{z_1^2}{4}, \quad (\text{A3})$$

$$S_0 \equiv \sum_{n>0} J_n^2(nz_1) = \frac{1}{2\sqrt{1-z_1^2}} - \frac{1}{2}, \quad (\text{A4})$$

$$S_2 \equiv \sum_{n>0} n^2 J_n^2(nz_1) = \frac{z_1^2(4+z_1^2)}{16(1-z_1^2)^{3/2}}. \quad (\text{A5})$$

$$S_4 \equiv \sum_{n>0} n^4 J_n'^2(nz_1) = \frac{z_1^2(64 + 592z_1^2 + 472z_1^4 + 27z_1^6)}{256(1 - z_1^2)^{3/2}}. \quad (A6)$$

The first is a result of Nielsen [58] according to Schott who derived the second and third results [59], while the fourth can be found in [60] [note that our notation differs from that paper, which also contains a typographical error in their Eq. (24) for S_2]. The sums involving J_n' are

$$S_2' \equiv \sum_{n>0} n^2 J_n'^2(nz_1) = \frac{4 + 3z_1^2}{16(1 - z_1^2)^{5/2}}. \quad (A7)$$

$$S_4' \equiv \sum_{n>0} n^4 J_n'^2(nz_1) = \frac{64 + 624z_1^2 + 632z_1^4 + 45z_1^6}{256(1 - z_1^2)^{11/2}}, \quad (A8)$$

given in [27,60], respectively. The latter paper also gave a double integral representation for the series S_{-1} (here denoted F_+). Referring to a theorem by Watson [61] the authors of [55] derive an iterative scheme for higher-order Kapteyn series, giving, for example,

$$S_1 = \frac{1}{1 - z_1^2} \left(z_1 \frac{\partial}{\partial z_1} \right)^2 S_{-1}. \quad (A9)$$

$$S_3 = \frac{1}{1 - z_1^2} \left(z_1 \frac{\partial}{\partial z_1} \right)^2 S_1. \quad (A10)$$

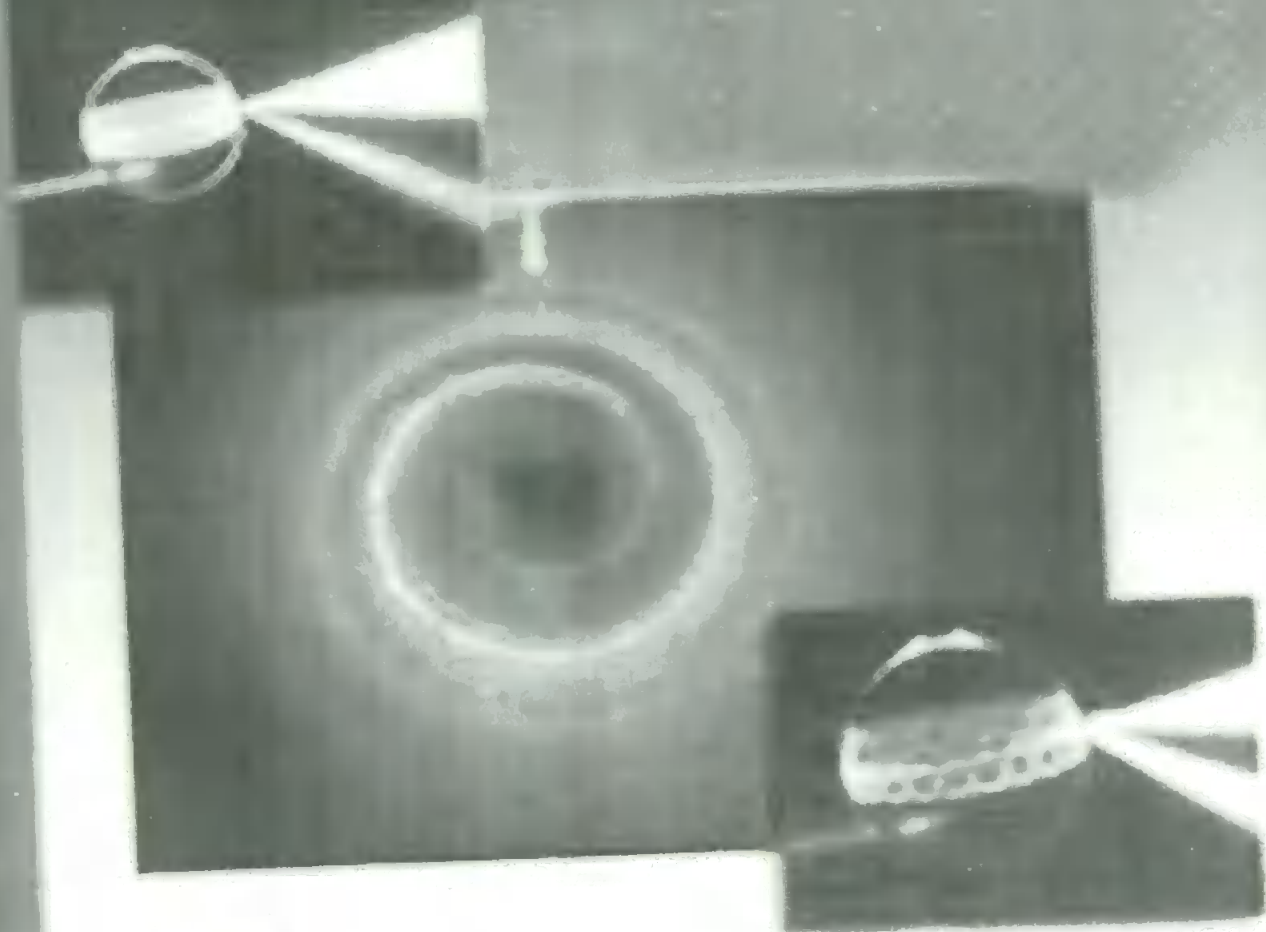
[1] A. Strickland and G. Mourou, *Opt. Commun.* **56**, 219 (1985).
 [2] The Vulcan 10 Petawatt Project: http://www.clf.rl.ac.uk/Facilities/vulcan/projects/10_pw/10_pw_index.htm
 [3] The Extreme Light Infrastructure (ELI) Project: <http://www.extreme-light-infrastructure.eu>
 [4] T. Heinzl and A. Ilderton, e-print arXiv:0809.3348.
 [5] T. Heinzl and A. Ilderton, topical issue of *Eur. Phys. J. D* (to be published).
 [6] M. Marklund and J. Lundin, e-print arXiv:0812.3087.
 [7] J. Toll, Ph.D. thesis, Princeton, 1952 (unpublished).
 [8] T. Heinzl, B. Liesfeld, K.-U. Amthor, H. Schwöerer, R. Sauerbrey, and A. Wipf, *Opt. Commun.* **267**, 318 (2006).
 [9] G. Breit and J. Wheeler, *Phys. Rev.* **46**, 1087 (1934).
 [10] W. Heisenberg and H. Euler, *Z. Phys.* **98**, 714 (1936).
 [11] J. S. Schwinger, *Phys. Rev.* **82**, 664 (1951).
 [12] F. Sauter, *Z. Phys.* **69**, 742 (1931).
 [13] O. Klein, *Z. Phys.* **53**, 157 (1929).
 [14] H. R. Reiss, *J. Math. Phys.* **3**, 59 (1962).
 [15] D. L. Burke, R. C. Field, G. Horton-Smith, J. E. Spencer, D. Walz, S. C. Berridge, W. M. Bugg, K. Shmakov, A. W. Weidemann, C. Bula, K. T. McDonald, E. J. Prebys, C. Bamber, S. J. Boege, T. Koffas, T. Kotseroglou, A. C. Melissinos, D. D. Meyerhofer, D. A. Reis, and W. Ragg, *Phys. Rev. Lett.* **79**, 1626 (1997).
 [16] C. Bamber, S. J. Boege, T. Koffas, T. Kotseroglou, A. C. Melissinos, D. D. Meyerhofer, D. A. Reis, W. Ragg, C. Bula, K. T. McDonald, E. J. Prebys, D. L. Burke, R. C. Field, G. Horton-Smith, J. E. Spencer, D. Walz, S. C. Berridge, W. M. Bugg, K. Shmakov, and A. W. Weidemann, *Phys. Rev. D* **60**, 092004 (1999).
 [17] T. Heinzl and A. Ilderton, *Opt. Commun.* **282**, 1879 (2009).
 [18] K. T. McDonald, Preprint DOE/ER/3072-38; www.hep.princeton.edu/mcdonald/e144/prop.pdf
 [19] A. I. Nikishov and V. I. Ritus, *Zh. Eksp. Teor. Fiz.* **46**, 776 (1963) [*Sov. Phys. JETP* **19**, 529 (1964)].
 [20] A. I. Nikishov and V. I. Ritus, *Zh. Eksp. Teor. Fiz.* **46**, 1768 (1964) [*Sov. Phys. JETP* **19**, 1191 (1964)].
 [21] N. B. Narozhnyi, A. Nikishov, and V. Ritus, *Zh. Eksp. Teor. Fiz.* **47**, 930 (1964) [*Sov. Phys. JETP* **20**, 622 (1965)].
 [22] A. I. Nikishov and V. I. Ritus, *Zh. Eksp. Teor. Fiz.* **47**, 1130 (1964) [*Sov. Phys. JETP* **20**, 757 (1965)].
 [23] L. S. Brown and T. W. B. Kibble, *Phys. Rev.* **133**, A705 (1964).
 [24] I. I. Goldman, *Phys. Lett.* **8**, 103 (1964).
 [25] N. Sengupta, *Bull. Calcutta Math. Soc.* **41**, 187 (1949).
 [26] Vachaspati, *Phys. Rev.* **128**, 664 (1962); **130**, E2598 (1963).
 [27] E. S. Sarachik and G. T. Schappert, *Phys. Rev. D* **1**, 2738 (1970).
 [28] Y. Y. Lau, F. He, D. Umstadter, and R. Kowalczyk, *Phys. Plasmas* **10**, 2155 (2003).
 [29] T. W. B. Kibble, *Phys. Rev.* **138**, B740 (1965).
 [30] D. Volkov, *Z. Phys.* **94**, 250 (1935).
 [31] N. Sengupta, *Bull. Calcutta Math. Soc.* **44**, 175 (1952).
 [32] V. Berestetskii, E. Lifshitz, and L. Pitaevskii, *Quantum Electrodynamics (Course of Theoretical Physics)* (Butterworth, Washington, DC, 1982).
 [33] K. T. McDonald, Conference on Probing Luminous and Dark Matter, Adrian Fest, Rochester, New York, September 1999; Available at <http://viper.princeton.edu/mcdonald/e144/adrianfestdoc.pdf>
 [34] J. Schwinger, *Phys. Rev.* **91**, 728 (1953).
 [35] R. J. Glauber, *Phys. Rev. Lett.* **10**, 84 (1963).
 [36] R. J. Glauber, *Phys. Rev.* **130**, 2529 (1963).
 [37] R. J. Glauber, *Phys. Rev.* **131**, 2766 (1963).
 [38] I. Bialynicki-Birula and Z. Bialynicka-Birula, *Phys. Rev. A* **8**, 3146 (1973).
 [39] J. Bergou and S. Varro, *J. Phys. A* **14**, 2281 (1981).
 [40] K. Gottfried and T.-M. Yan, *Quantum Mechanics: Fundamentals* (Springer, New York, 2004).
 [41] L. M. Frantz, *Phys. Rev.* **139**, B1326 (1965).
 [42] S. Weinberg, *The Quantum Theory of Fields, Vol. 1: Foundations*, (Cambridge University Press, Cambridge, 1995).
 [43] W. H. Furry, *Phys. Rev.* **81**, 115 (1951).
 [44] Y. S. Tsai, *Phys. Rev. D* **48**, 96 (1993).
 [45] E. Esarey, S. K. Ride, and P. Sprangle, *Phys. Rev. E* **48**, 3003 (1993).
 [46] D. Y. Ivanov, G. L. Kotkin, and V. G. Serbo, *Eur. Phys. J. C* **36**, 127 (2004).
 [47] S.-y. Chen, A. Maksimchuk, and D. Umstadter, *Nature (London)* **396**, 653 (1998).

- [48] R. A. Sunyaev and Y. B. Zeldovich, *Astrophys. Space Sci.* **7**, 20 (1970).
- [49] R. A. Sunyaev and Y. B. Zeldovich, *Annu. Rev. Astron. Astrophys.* **18**, 537 (1980).
- [50] M. Birkinshaw, *Phys. Rep.* **310**, 97 (1999).
- [51] Forschungszentrum Dresden-Rossendorf; <http://www.fzd.de/db/Cms?pNid=1483>
- [52] A. Ilderton, T. Heinzl, and M. Marklund (to be published).
- [53] M. Abramowitz and I. A. Stegun, *Handbook of Mathematical Functions* (Dover, New York, 1972).
- [54] W. Kapteyn, *Ann. Sci. Éc. Normale Supér.* **91**, 10 (1893).
- [55] I. Lerche and R. C. Tautz, *J. Phys. A: Math. Theor.* **41**, 035202 (2008).
- [56] G. Priebe, D. Laundy, M. A. Macdonald, G. P. Diakun, S. P. Jamison, L. B. Jones, D. J. Holder, S. L. Smith, P. J. Phillips, B. D. Fell, B. Sheehy, N. Naumova, I. V. Sokolov, S. Ter-Avetisyan, K. Spohr, G. A. Krafft, J. B. Rosenzweig, U. Schramm, F. Grüner, G. J. Hirst, J. Collier, S. Chattopadhyay, and E. A. Seddon, *Laser Part. Beams* **26**, 649 (2008).
- [57] G. N. Watson, *A Treatise on the Theory of Bessel Functions* (Cambridge University Press, New York, 1995.) Reprint of second edition from 1944, first edition published 1922.
- [58] N. Nielsen, *Handbuch der Theorie der Cylinderfunktionen* (Teubner, Leipzig, 1904).
- [59] G. Schott, *Electromagnetic Radiation* (Cambridge University Press, New York, 1912).
- [60] I. Lerche and R. C. Tautz, *Astrophys. J.* **665**, 1288 (2007).
- [61] G. N. Watson, *Messenger of Mathematics* **40**, 150 (1917).

Book of Abstracts:

16th Iranian Conference on Optics & Photonics

Yazd University
26-28 January 2010



کتابخانه علمی تخصصی
فیزیک



Photonics Research Group
Yazd University



انجمن بین‌المللی فیزیک لیزر و اپتیک

مؤثرین کنفرانس اپتیک و فیزیک لیزر ایران و دومین کنفرانس علمی فیزیک ایران

۸ تا ۱۳ آبان ۱۳۸۸



۱۵۰۹ - P

Signatures of high-intensity Compton scattering

C. Harvey¹, T. Heinzl¹ and A. Ilderton²

¹University of Plymouth, UK

²University of Umea, Sweden

Abstract:

This paper discusses the predicted signatures of nonlinear Compton scattering, that will occur when a high-intensity laser beam is brought into collision with a beam of electrons from a linac. We consider various intensity effects on the emission spectrum of the scattered photons, both in terms of their frequencies, and in terms of their scattering angles. At high intensities we predict a substantial redshift of the usual kinematic Compton edge of the photon spectrum caused by the large, intensity-dependent effective mass of the electrons inside the laser beam. In addition, we find that the notion of the centre-of-mass frame for a given harmonic becomes intensity dependent.

Keywords: *Compton scattering, intensity effects.*

Signatures of High-Intensity Compton Scattering

C. Harvey¹, T. Heinzl¹ and A. Ilderton²

¹University of Plymouth, UK

²University of Umeå, Sweden

christopher.harvey@plymouth.ac.uk

Abstract: *This paper discusses the predicted signatures of nonlinear Compton scattering, that will occur when a high-intensity laser beam is brought into collision with a beam of electrons from a linac. We consider various intensity effects on the emission spectrum of the scattered photons, both in terms of their frequencies and in terms of their scattering angles. At high intensities we predict a substantial redshift of the usual kinematic Compton edge of the photon spectrum caused by the large, intensity-dependent effective mass of the electrons inside the laser beam. In addition, we find that the notion of the centre-of-mass frame for a given harmonic becomes intensity dependent.*

Keywords: Compton scattering, intensity effects.

1 Introduction

Recent technological breakthroughs have led to lasers of unprecedented powers and intensities, the current records being about 1 PetaWatt (PW) and 10^{22} W/cm², respectively. During the next few years further increases are expected, most notably at the planned European "Extreme Light Infrastructure" (ELI), where the power and intensity may be as much as 3 orders of magnitude higher than any current facility [2]. This will allow for an experimental probing of a previously inaccessible region of the QED parameter space, and so motivates this theoretical reassessment of intensity effects in QED.

To be specific, we will be considering the nonlinear Compton scattering that occurs when a beam of electrons from a linac is brought into collision with a high-intensity laser. In this case an

electron of momentum p absorbs n laser photons γ_L , each of momentum k , then emits a single photon of momentum k' , giving us the process

$$e^-(p) + n\gamma_L(k) \rightarrow e^-(p') + \gamma(k'). \quad (1)$$

If we assume that the electron and laser photons collide head-on, then there is only one angle to consider – the scattering angle of the emitted photon θ . The incident four-momenta are then

$$k^\mu = \omega(1, \mathbf{n}), \quad p^\mu = (E_p, \mathbf{p}), \quad (2)$$

with the outgoing (primed) quantities defined analogously.

We will model the laser field by a circularly polarised plane wave of amplitude a

$$A^\mu = a_1^\mu \cos(k \cdot x) + a_2^\mu \sin(k \cdot x), \quad (3)$$

where k is the (light-like) propagation four-vector and the Lorentz gauge condition is satisfied. The Dirac equation can be solved exactly for electrons in such a background (Volkov solution [4]), and for a thorough discussion we refer the reader to [5].

The laser beam is characterised by the 'dimensionless laser amplitude' a_0

$$a_0 \equiv \frac{eE\lambda_L}{mc^2}. \quad (4)$$

This is a purely classical quantity, a ratio of two energies – the ratio of the energy gain of the electron moving over a laser wavelength λ_L with the electron's rest mass. It may be generalised to an explicitly Lorentz and gauge-invariant expression [3], but for our purposes it is sufficient to adopt a rule-of-thumb formula expressing a_0 in terms of laser power [6]

$$a_0^2 \approx 5 \times 10^3 P[\text{PW}]. \quad (5)$$

In this paper we will be considering the phenomenology of the high intensity $a_0 > 1$ but relatively low energy $\omega \ll mc^2$ regime. As mentioned earlier, this region of the QED parameter space has only recently become experimentally accessible.

2 Kinematics

2.1 Momentum/Mass Shift

Due to the presence of the laser field, the Volkov electrons acquire a quasi four-momentum q

$$q \equiv p + \frac{a_0^2 m^2}{2k \cdot p} k \equiv p + q_L. \quad (6)$$

Hence the electrons acquire an additional, *intensity-dependent* longitudinal momentum q_L caused by the presence of the laser field. This may be found by applying the kinetic momentum operator to the Volkov solution and taking the time-average of the result. However, it may also be understood classically as the time-average of the electron 'quiver' motion in the plane wave. Squaring q allows us to define an effective electron mass m_*

$$m_*^2 \equiv q^2 = m^2 (1 + a_0^2). \quad (7)$$

Calculating the scattering amplitude, we find that the quasi momentum is conserved in the scattering process [1, 5]

$$q + nk = q' + k'. \quad (8)$$

2.2 Scattering Frequency

Inserting the momentum expressions (2) into (8), the intensity-dependent scattered photon frequency is found to be

$$\nu_n' = \frac{n\nu}{1 + j_n(1 - \cos\theta)}; \quad j_n = j_n(n, \gamma, \nu, a_0). \quad (9)$$

where γ is the initial electron energy and $\nu = \omega/m$. Notice that the sign of j_n determines whether the scattered photon is red or blue shifted relative to the laser photons.

3 Photon Emission Rates

We now consider the emission rates for the scattered photons. For a circularly polarised plane wave the cross section can be expressed analytically [5]

3.1 Frequency Dependence

We begin by considering the emission rates in terms of the scattered photon frequency ν' . For an individual harmonic we find

$$\frac{dW_n}{d\nu'} = -\frac{1}{\gamma(1+\beta)j_n} J_n(a_0, \nu, \nu_n'), \quad (10)$$

where γ, β are the electron Lorentz parameters and the function J_n is composed of Bessel functions. To obtain the total rate one simply sums over all the harmonics.

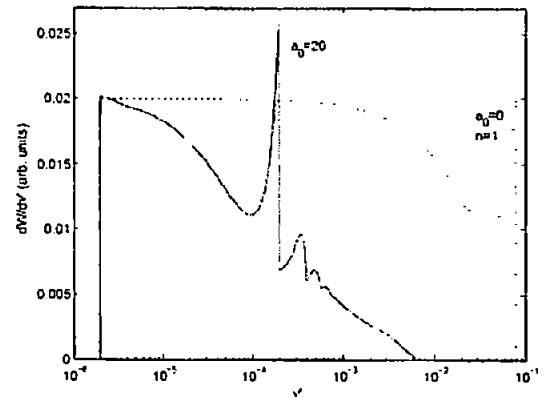


Figure 1: Theoretical photon spectrum (sum of first 50 harmonics) for intensity $a_0=20$ compared to linear Compton scattering ($n=1, a_0=0$) as a function of ν' . Initial electron $\gamma=100$.

A plot of the emission spectrum is shown in Figure 1 for $a_0=20$, where we have also included the text book linear Compton (Klein-Nishina) case ($n=1, a_0=0$) for comparison. From the plot several features are apparent. Firstly, and most significantly, is the red shift of the Compton peak by a factor of $1 + a_0^2 \approx 400$ compared to the linear case. Secondly, we observe a series of secondary peaks to the right of the main Compton 'edge', due to the presence of the higher harmonics ($n=2,3,\dots$). Assuming that these are not washed out by background effects not included in our analysis, this would be the first time that any higher harmonics were experimentally detectable for a circularly polarised laser field.

We showed earlier how the sign of $j_n(a_0, \gamma)$ determines whether the scattered photon is red or blue shifted relative to the laser photons. This suggests that by tuning γ and a_0 it should be possible to change the scattered photon spectrum from a blue shift to a red shift. In particular, at the

point where j_n changes sign, the n^{th} harmonic spectrum will collapse to the line $\nu_n' = n\nu$. Analytically we find that this will occur when a_0 attains its critical value of

$$a_{0,\text{crit}} \equiv \sqrt{\frac{2(\gamma\beta - n\nu)}{\chi(1-\beta)}} \approx 2\gamma. \quad (11)$$

collapses is the point where $P = nk + q = nk + p + q_L$ equals zero. In a certain sense therefore, the point where j_n changes sign can be used to define a 'centre-of-mass' frame for the n^{th} scattering process. Thus by tuning a_0 , as we have done in Figure 2, we are effectively changing the frame of reference in which the scattering process is viewed.

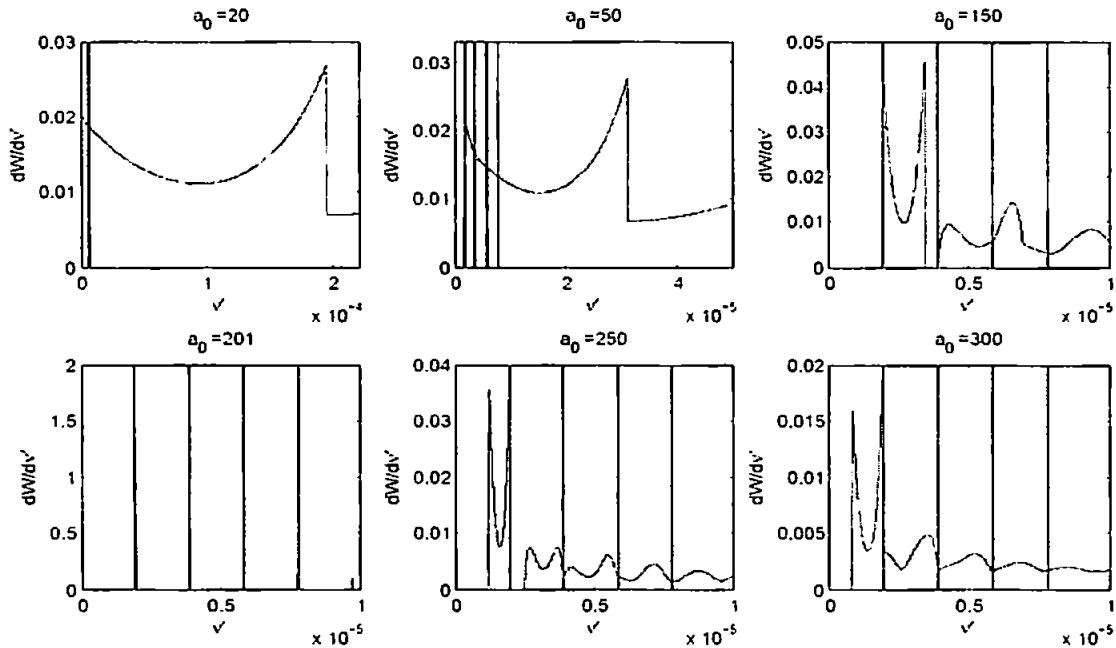


Figure 2: Sequence of plots showing the photon spectra for different values of a_0 (arb. units). Parameters are such that $a_{0,\text{crit}}=200$. Vertical (grey) lines correspond to frequencies $n\nu$.

In Figure 2 we show a sequence of emission spectra for the case $a_{0,\text{crit}}=200$ ($n=1$). If we go through the whole sequence, the following picture emerges. For the subcritical case, $a_0 < a_{0,\text{crit}}$, the harmonic ranges are blue shifted (i.e. located to the right of the respective vertical lines $\nu' = n\nu$). As a_0 approaches its critical value the harmonic ranges shrink and a gap between the first and the second appears (third plot). At $a_0 = a_{0,\text{crit}}$ the first harmonic range shrinks to a point, with the neighbouring ranges also becoming very narrow. Once a_0 becomes supercritical the harmonic ranges are red shifted, with the ranges increasing again and the gaps closing.

To understand what is happening we consider the collision momenta. Recall that, in the case of *linear* Compton scattering, there is no frequency shift when $P = k + p$ equals zero (i.e. in the centre-of-mass frame of the collision). Now, making the analogy to *nonlinear* Compton scattering, we see that the point where the n^{th} harmonic spectrum

3.2 Angular Dependence

We may also consider the emission rates as a function of the scattering angle θ . Performing the necessary calculations, we find the angular emission rate for a given harmonic to be

$$\frac{dW_n}{d\Omega} = \frac{n\nu}{\chi(1+\beta)[1+j_n(1-\cos\theta)]^2} J_n^2(a_0, \nu') \quad (12)$$

Note that here we have used the angular measure $d\Omega = \sin\theta d\theta$, since for a circularly polarised laser field there is no dependence on the azimuthal angle ϕ . In Figure 3 we show the angular emission rates for the first five individual harmonics. We see that the fundamental ($n=1$) harmonic contributes most strongly in the backscattering ($\theta = \pi$) direction, while the higher harmonics also peak near this point.

Unlike with the ν' parameterisation where a given frequency interval only contains a finite number of harmonics, with the θ parameterisation *all* the

harmonics are constrained to the finite range $\theta=0..\pi$. Thus, before we can sum the harmonics (12) to calculate the total emission rate, we are forced to confront the issue of convergence.

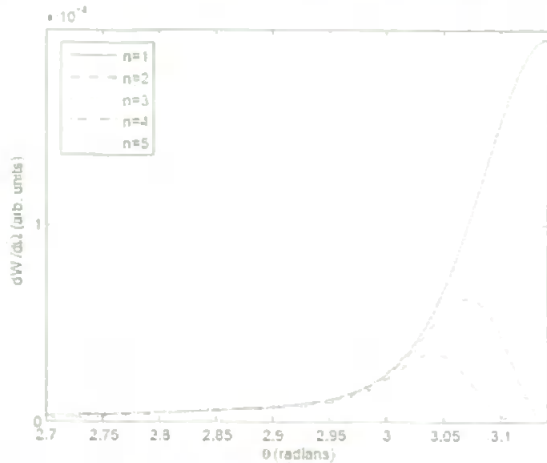


Figure 3: Individual emission rates for the first five harmonics as a function of the scattering angle θ . $a_0=20$.

Fortunately we find that we can express the series (12) in such a way that it can be bounded from above by Kapteyn series of the second kind. Then, by using the results of [7], we find that we are able to calculate the angular emission rate accurately (by summing the series numerically) everywhere apart from a narrow region around the peak (that can be seen forming in Figure 3). In effect this means that we are able to determine the nature of the angular photon spectrum, just not the absolute magnitude of the peak. Performing the calculation we find that, for the parameter values we have been considering (e.g. $a_0=20$, $\gamma=100$), the photon spectrum forms a sharp peak in the backscattering ($\theta=\pi$) direction and is close to zero everywhere else. As a_0 is increased the peak moves more towards the forward scattering direction, giving a symmetric plot for $a_0 = 2\gamma$ at an angle $\theta=\pi/2$.

4 Conclusion

In this contribution we predict a number of laser intensity effects on the photon emission rates for an electron inside a laser field. These effects are mostly of a classical nature, being fundamentally due to the mass shift caused by the relativistic quiver motion of an electron in the laser field.

Ranked in order of their relevance, the main intensity effects are (i) a redshift of the Compton edge as compared to the linear Compton (Klein-Nishina) case, (ii) the appearance of higher harmonic peaks ($n>1$) in the photon spectra, and (iii) the notion that the centre-of-mass frame for a given harmonic becomes intensity dependent.

The next step is to actually perform the experiments required for measuring the effects listed above. We stress once again that nonlinear Compton scattering will allow the probing of a previously inaccessible region of the QED parameter space, and we hope that the analysis contained in this paper will prove useful to those involved with various experiments planned for the near future in Europe and elsewhere.

Acknowledgements

A. Ilderton acknowledges support from IRCSET and C. Harvey from EPSRC.

References

- [1] C. Harvey, T. Heinzl and A. Ilderton, "Signatures of high-intensity Compton scattering" *Phys. Rev. A*, Vol. 79, 063407, 2009.
- [2] T. Heinzl and A. Ilderton, "Exploring high-intensity QED" *Topical issue of Eur. Phys. J. D* (to be published).
- [3] T. Heinzl and A. Ilderton, "A Lorentz and gauge invariant measure of laser intensity" *Opt. Commun.* Vol. 282, pp 1879-1883, 2009.
- [4] D. Volkov, "Über eine Klasse von Lösungen der Diracschen Gleichung" *Z. Phys.* Vol 94, pp 50-260, 1935.
- [5] V. Berestetskii, E. Lifshitz and L. Pitaevskii, *Quantum Electrodynamics (Course of Theoretical Physics)*, Butterworth, 1982.
- [6] K.T. McDonald, "Proposal for Experimental Studies of Nonlinear Quantum Electrodynamics" available as <http://www.hep.princeton.edu/~mcdonald/e144/prop.pdf> 1986.
- [7] I. Lerche and R.C. Tautz, "A note on the summation of Kapteyn series in astrophysical problems" *Astrophys. J.* Vol 665, pp 1288-1291, 2007.